

HIGH-SPEED MRI-GUIDED NEAR-INFRARED TOMOGRAPHY SYSTEM  
TO MONITOR BREAST HEMODYNAMICS IN VIVO

A Thesis

Submitted to the Faculty

in partial fulfillment of the requirements for the

degree of

Doctor of Philosophy

by

Zhiqiu Li

Thayer School of Engineering

Dartmouth College

Hanover, New Hampshire

May 2011

Examining Committee:

Chairman \_\_\_\_\_  
Brian W. Pogue, Ph.D.

Member \_\_\_\_\_  
Keith D. Paulsen, Ph.D.

Member \_\_\_\_\_  
Shudong Jiang, Ph.D.

Member \_\_\_\_\_  
Venkat Krishnaswamy, Ph.D.

Member \_\_\_\_\_  
Daqing Piao, Ph.D.

\_\_\_\_\_  
Brian W. Pogue  
Dean of Graduate Studies



## **Abstract**

Diffuse spectroscopic imaging of breast cancer with near-infrared (NIR) light can be integrated into magnetic resonance imaging (MRI), to provide local molecular information about the tissue regions. Dynamics within the tissue from pulsatile blood volume and oxygenation levels can be indicative of pathogenic events such as cellular proliferation and angiogenesis. Additionally the pharmacokinetics and leakage of optical contrast agents within these tissues can be helpful in tumor diagnosis. Measurement of these events can require a fast imaging system, and in this work a new data acquisition design was studied, which can greatly improve the imaging speed and realize dynamic contrast imaging with combined NIR-MRI exams.

This study demonstrates the technology and methodology to build a NIR tomography system with spectrally-encoded sources in two wavelength bands which is capable of quantifying the temporal oxyhemoglobin and deoxyhemoglobin contrast in breast tissue at a 20 Hz bandwidth. The system was integrated into a 3T MRI system through a customized breast coil interface for simultaneous optical and MRI acquisition. In this configuration, the MR images provide breast tissue structural information for NIR spectroscopy of adipose and fibro-glandular tissue in breast. System stability and noise were carefully characterized, and different reconstruction methods were compared to optimize image quality. Spectral characterization and dynamic performance of the NIR system were verified through a series of phantom experiments. Normal human subjects were imaged with finger pulse oximeter (PO) plethysmogram synchronized to the NIR-MRI system to provide a frequency-locked data reference. Both the raw data from the NIR system and the recovered absorption variation of the breast at two wavelengths

showed the same frequency as the PO output, indicating that this system can recover the temporal absorption changes caused by breast hemodynamics. The system was used to spectrally characterize changes in normal fibroglandular and adipose tissue.

## Acknowledgements

First of all, I would like to thank my Advisor Prof. Brian Pogue for his long time guidance and generous support for the past five years. Brian was the most important person to lead me into the amazing world of biomedical optics. He spent enormous time with me discussing the problems and possible applications of my project, and helped push it forward with his insight and resources. He also offered superior research conditions and comprehensive training opportunities which help build me into a better researcher.

I appreciate the great help from Prof. Shudong Jiang, who taught me most of the necessary skills and knowledge about optical devices and instrumentation. She is busy but always willing to offer suggestions and help. Her strictness has been “forcing” me to refine my system and get more robust results.

I also must thank Prof. Venkat Krishnaswamy for his great help on the hardware. We spent a lot of time working together and I learnt a lot from him, both technically and methodologically.

I also want to thank Prof. Keith Paulsen who has been bridging Thayer and DHMC, and gained me access to many clinical resources. He set an excellent example as an academic leader, and I am “pushing myself out of my comfort zone everyday” as he suggested to all of us.

I am grateful to Prof. Daqing Piao for his pioneering contribution on the spectral encoding technique, and his constant encouragement and advice on my work. His tenacity, innovative mind, and achievement have been inspiring me all the way.

It has been a wonderful experience to work in the Optics in Medicine Lab at Thayer School of Engineering. I want to thank Subhadra Srinivasan and Phaneendra Yalavarthy's help on the numerical algorithm, Scott Davis' careful revision of my papers, Michael Mastanduno's help on parameter verification, and Xin Wang and Jia Wang's discussion on virtually everything. I also want to thank all the other colleagues, Colin Carpenter, Dax Kepshire, Frederic Leblond, Kimberly Samkoe, Julia A. O'Hara, Martin Isabelle, Josiah Gruber, Ashley Laughney, Kelly Michaelsen, Jennifer-Lynn Demers, Michael Jermyn, Robert Holt and Sason Torosean, for all they have done for me.

Finally and most importantly, I would like to thank my parents, Jianshe Li and Mingjuan Wang. Your love and encouragement give me unlimited power on the road of science. And special thanks to Jing Lu, the first volunteer on my system, the one who spent many nights with me outside the MR room, my wife and my greatest source of happiness on this foreign land.

This work has been funded by National Institutes of Health research grants R33CA100984 and P01CA080139.

# Table of Contents

.....	ii
.....	iv
<b>of Contents.....</b>	<b>vi</b>
<b>of Tables.....</b>	<b>viii</b>
<b>of Figures and Illustrations.....</b>	<b>ix</b>
<b>of Acronyms .....</b>	<b>xviii</b>
<b>1. Introduction.....</b>	<b>- 1 -</b>
.1 Overview .....	- 1 -
.2 Breast Cancer and Current Clinical Imaging Techniques .....	- 1 -
.3 Development of Optical Imaging & Pulse Oximetry .....	- 3 -
.4 NIR Spectroscopy of Tissue.....	- 6 -
.5 Current Status of NIR Breast Cancer Imaging.....	- 8 -
.6 Multimodal Imaging System.....	- 12 -
.7 High-speed NIR Tomography of Breast Tissue.....	- 13 -
<b>2. Video-rate Single Wavelength Tomography System.....</b>	<b>- 18 -</b>
.1 System Configuration.....	- 19 -
.1.1 Spectrally encoded sources .....	- 21 -
.1.2 Optical Detectors .....	- 25 -
.1.3 Tissue/Phantom Interface.....	- 30 -
.1.4 Exposure Synchronization .....	- 32 -
.2 Experimental procedure and raw data process .....	- 34 -
.2.1 Calibration of input power of source channels .....	- 35 -
.2.2 Calibration of detection efficiencies of detection channels .....	- 36 -
.2.3 Raw data process.....	- 37 -
.3 Static Blood Phantom Imaging Experiment.....	- 39 -
.3.1 Direct Reconstruction of $\mu_a$ .....	- 40 -
.3.2 Difference Reconstruction of $\mu_a$ .....	- 43 -
.3.3 Region-based Reconstruction of $\mu_a$ .....	- 46 -
.4 Dynamic Blood Phantom Imaging Experiment .....	- 47 -
.4.1 Static anomaly with varying absorption property.....	- 47 -
.4.2 Moving anomaly with constant absorption property .....	- 51 -

.5	Pulsatile Phantom Experiment .....	- 53 -
.6	Summary .....	- 59 -
<b>3.</b>	<b>Dual-wavelength Near-Infrared Dynamic Oximetry Imaging System..</b>	<b>- 61 -</b>
.1	System Design.....	- 61 -
.2	Total hemoglobin recovery .....	- 68 -
.3	Dynamic Oxygen Saturation Recovery.....	- 71 -
.4	Pulse Oximetry using NIR light.....	- 73 -
.5	Summary .....	- 85 -
<b>4.</b>	<b>Human Subject Imaging Experiments.....</b>	<b>- 87 -</b>
.1	Experimental Setup .....	- 87 -
.2	Analysis of possible errors .....	- 91 -
.2.1	Coupling error.....	- 95 -
.2.2	Position of the anomaly region .....	- 97 -
.2.3	Size of the anomaly region .....	- 100 -
.2.4	$\mu_s$ ' of the homogeneous phantom.....	- 101 -
.2.5	$\mu_s$ ' of the heterogeneous medium.....	- 102 -
.2.6	Conclusion for error analysis .....	- 107 -
.3	Imaging experiment of the first human subject.....	- 108 -
.4	Imaging experiment of the second human subject.....	- 116 -
.5	Conclusion.....	- 122 -
<b>5.</b>	<b>Conclusions.....</b>	<b>- 124 -</b>
.1	Thesis summary.....	- 124 -
.2	Future directions.....	- 126 -
	.....	<b>- 131 -</b>

## **List of Tables**

2.1. The optimal current and temperature settings for 785 nm LDs.....	- 23 -
3.1. The optimal current and temperature settings for 830 nm LDs.....	- 67 -

## List of Figures and Illustrations

- 1.1. Five-Year Survival Rates by Stage at Diagnosis and Race [3] .....- 2 -
- 1.2. Pulse oximeter. (a) a typical fingertip pulse oximeter.(b) Light Absorbance in a finger [20]. .....- 6 -
- 1.3. The absorption spectrum per unit molar concentration of HbO, Hb, water and fat. Data was taken from Oregon Medical Laser Center. Absorption coefficients of and Hb are calculated with concentration of  $0.2 \text{ mM} - 1 \cdot \text{mm} - 1$ . .....- 7 -
- 1.4. (a) The NIR spectroscopy system developed by the UCI group. (b) The handheld scanner. (c) A patient was scanned by the handheld scanner. (d) Line scan result of four major chromophores of a tumor. (e) Fitted  $\mu a$  v.s. wavelength of normal tissue and tumor [1, 27]. .....- 9 -
- 1.5. (a) An engineering drawing of the optical source and detection subsystem. The upper circular region holds three rings of sixteen fiber bundles each, mounted to sixteen linear translation stages. The tomography imaging is achieved by cycling the laser source into each fiber sequentially through the circular translation stage on the bottom. (b) The fiber-optical interface. (c) The patient bed with imaging system underneath. (d) A female subject positioned on the table with her breast in the imaging array [25].....- 10 -
- 1.6. A schematic of the NIR imaging system at University of Pennsylvania [1].....- 12 -
- 1.7. Result of an patient exam using MR/NIR hybrid imaging [58]. Axial MR imaging showing coronal plane of optical imaging (a). Panel (b) shows a 3D representation of combined maximum intensity projection MR image and 3D rendering of optical solution of HbT. Optical solutions for HbT (d), water (e), oxygen saturation (f), scatter amplitude (g), and scatter power (h), are shown overlaid on top of coronal MR (c). In each case the background value is removed. (I) shows the multi-wavelength NIR system used in this experiment. ....- 13 -
- 1.8. (a) Block diagram of the instrument setup using source switching method [65]. (b) Schematic diagram of the NIR tomography system by spectrally encoded parallel source delivery [67]. .....- 16 -
- 2.1. A diagram of the video-rate near infrared tomography system is shown. Eight spectrally encoded LD systems were integrated onto one cart. Eight fiber-coupled spectrometers with high-resolution CCDs are integrated onto another cart and set to respond to an external TTL trigger signal. The signal is generated by a data

acquisition board and then split into eight channels by a customized splitter circuit, and delivered to the EXT SYNC port on each CCD simultaneously. Imaging data is transferred back to the computer for post processing. A flexible fiber mount is customized to hold the phantom or tissue in between. ....- 20 -

2.2. (a) The customized cart sitting 8 spectrally encoded LDs [67]. (b) A LD with its supporting components. (c) The TE-Cooled mount. (d) The temperature control board. (e) The drive current control board.....- 23 -

2.3. Stability test of 8 LD sources in the 785 nm wavelength band. (a) The intensity stability of the LDs. (b) The wavelength stability of the LDs. (c) The standard deviation of intensity divided by the average intensity of the LDs. (d) The standard deviation of wavelength of the LDs. ....- 25 -

2.4. The detection system consisting of 8 spectrometers and 8 CCDs [75] is shown. - 26 -

2.5. Linearity and noise analysis of 7 CCDs, with each row (a) to (g) showing data from one of the CCDs. The first column is the linearity. The second column is the noise level relative to signal intensity. The third column is the noise level in percent.- 30 -

-

2.6. (a) The average light paths for the circular geometry and the slab geometry are illustrated. (b) Experimental photograph of a 64.5 mm thick slab phantom is shown with 8 orange source fibers on the right side and 8 black detection fibers on the left. (c) The signals from 8 LDs measured by one CCD with a circular homogeneous phantom. (d) The signals from 8 LDs measured by one CCD with a slab homogeneous phantom. Note in (c) that most of the laser signals are not really detectable. ....- 31 -

2.7. (a) The splitter circuit box to convey the trigger signal to the EXT SYNC ports of 8 CCDs. (b) The NI DAQ board to generate trigger signal. (c) The LABVIEW program interface to control the frequency and shape of the trigger signal. ....- 34 -

2.8. (a) The procedure to calibrate source intensities. (b) The procedure to calibrate detection efficiencies of all detection channels. ....- 36 -

2.9. The procedure to calculate attenuation from each source-detector pair for one measurement is shown. ....- 38 -

2.10. Direct reconstruction results of  $\mu a$  on the imaging plane of a heterogeneous phantom with different blood concentrations in the anomaly. (a)-(d) show reconstructed images of the phantom with swine blood concentration of 1%, 2%, 3% and 4%. The reconstructed and true values of  $\mu a$  in the anomaly (marked as

ROI) and in the background (marked as BKG) of different swine blood concentrations are listed in (e), and plotted in (f). .....	- 42 -
2.11. Difference reconstruction results of $\mu a$ on the imaging plane of a heterogeneous phantom with different blood concentrations in the anomaly. (a)-(d) show reconstructed images of the phantom with swine blood concentration of 1%, 2%, 3% and 4%. The reconstructed and true values of difference $\mu a$ in the anomaly (marked as ROI) and in the background (marked as BKG) of different swine blood concentrations are listed in (e), and plotted in (f). .....	- 45 -
2.12. (a) The segmented mesh for region-based reconstruction. (b) A plot of the reconstructed and true values of $\mu a$ in the anomaly (marked as ROI), and the reconstrued $\mu a$ of the background (marked as BKG) of different swine blood concentrations. (c) A list of all reconstruction results in (b).....	- 47 -
2.13. (a) The reconstructed $\mu a$ of the anomaly (marked as ROI) and the background (marked as KG), using the direct reconstruction method. (b) Reconstructed images at several time points (in seconds).....	- 48 -
2.14. (a) The reconstructed $\mu a$ of the anomaly (marked as ROI) and the background (marked as BKG), using the difference reconstruction method. (b) Reconstructed images at several time points. ....	- 49 -
2.15. The reconstructed $\mu a$ of the anomaly (marked as ROI) and the background (marked as BKG), using the region-based reconstruction method. ....	- 50 -
2.16. The setup of the moving anomaly experiment with the slab tank which contained solution made of intralipid and blood. Here the black fibers were for detection, and the orange fibers were source delivery from laser diodes.....	- 51 -
2.17. Images of the tube at different locations recovered with the direct reconstruction method.....	- 52 -
2.18. Images of the tube at different locations recovered with the difference reconstruction method.....	- 53 -
2.19. System setup of the pulsatile phantom experiment is shown. High $\mu a$ solution was continuously pumped through a balloon at 0.5 Hz. The balloon was submerged in a 72 mm thick slab container filled with low $\mu a$ solution. The absorption contrast of the solution inside the balloon against outside was 3:1. Eight LDs were launched as sources, and 6 CCDs were set as detectors to acquire data at 10 frames per second. Slit widths on all spectrometers were set to 100 $\mu\text{m}$ . .....	- 54 -

- 2.20. Raw signals of different S-D pairs in frequency domain. (a) illustrates the 3 different optical paths through the phantom with straight lines. D1 to D6 were 6 detection spots connected to spectrometers through detection fibers. S1 to S8 were 8 laser beam input spots connected to LDs through source fibers. (b) shows the time domain signal and its frequency domain spectrum of path 1. The frequency domain amplitude has been normalized to its mean value. (c) shows the time domain signal and its frequency domain spectrum of path 2. (d) shows the time domain signal and its frequency domain spectrum of path 3.....- 56 -
- 2.21. (a) Mean value of reconstructed  $\mu a$  in the balloon versus time using direct reconstruction method. (b) Fourier transform of  $\mu a$  in (a). (c) Mean value of reconstructe  $\mu a$  in the balloon versus time using the region-guided reconstruction method. (d) Fourier transformed of  $\mu a$  in (c), which shows the dominance of the 0.5 Hz signal in the frequency spectrum.....- 58 -
- 3.1. (a) The fiber coupler housing two 400  $\mu\text{m}$  core fibers. These two fibers were aligned vertically with 0.06 inch center-to-center distance. (b) The cross section dimensions of the fiber coupler. (c) The source fiber plate. (d) The detector fiber plate. (e) The tissue/phantom interface. ....- 64 -
- 3.2. The spectra of 14 LDs of two spectrally-encoded source bands is shown as read out on a single spectrometer sequentially. ....- 64 -
- 3.3. Stability test of the 7 LD sources in the 830 nm wavelength band are shown including: (a) The intensity stability of the LDs. (b) The wavelength stability of the LDs. (c) The standard deviation of intensity divided by the average intensity of the LDs. (d) The standard deviation of wavelength of the LDs. ....- 66 -
- 3.4. (a) The interface of the LABVIEW program to collect and display the spectra of detected signals on the CCDs. (b) The LABVIEW VI section to initialize all CCDs with preset parameters. (c) The LABVIEW VI section to collect and display data of all CCDs. ....- 68 -
- 3.5. The agarose phantom with a liquid anomaly in the middle, used to vary hemoglobin levels in a single inclusion. The light sources were guided by the orange fibers on the right, and the black detection fibers on the left were connected to the spectrometers. ....- 69 -
- 3.6. (a) The reconstructed and true total hemoglobin in the anomaly region and the background are plotted, showing the expected linear and flat trends. (b) The reconstructed in the anomaly and the background are shown, with less than 2% standard error in both cases.....- 70 -

3.7. (a) The setup of the deoxygenation experiment is shown, with the blue probe of the reflectance tissue oximeter extended into the anomaly in the phantom. (b) The interface of the reflectance tissue oximeter (T-stat, Spectros Inc.).....	- 72 -
3.8. (a) The readings from the two modalities (visible reflectance probe <i>reference</i> and spectrally-encoded <i>NIR</i> tomography) versus time of the experiment are shown. The same data is replotted in (b) for from <i>NIR</i> tomography versus by reflectance probe <i>reference</i> .....	- 73 -
3.9. (a) The $\mu_a$ - <i>RR</i> curve when typical <i>PO</i> wavelengths (660 nm and 940 nm) are used. (b) The $\mu_{eff}$ - <i>RR</i> curve when two wavelengths of the <i>NIR</i> system (780 nm and 830 nm) are used. Curves with a postfix of $\mu_a$ only consider absorption, while curves with a postfix of $\mu_{eff}$ consider both absorption and scattering.....	- 77 -
3.10. The experimental setup for the balloon experiment. ....	- 78 -
3.11. (a) A 10-second data stream of the 785 nm raw data. (b) The Fourier transform of (a). (c) A 10-second data stream of the 830 nm raw data. (d) The Fourier transform of (c). ....	- 79 -
3.12. The flow chart of the direct calculation method to calculate <i>RR</i> and $\mu_a$ .....	- 80 -
3.13. Illustration of finding peaks and valleys of detected optical signal of two wavelengths during the steady state in order to calculate <i>RR</i> values. ....	- 80 -
3.14. Illustration of a detected optical signal during transient state. ....	- 81 -
3.15. (a) The <i>RR</i> curve obtained with the first method in equation 3.8. (b) The $\mu_a$ curve calculated from (a) according to equation 3.4. ....	- 82 -
3.16. The flow chart of the statistical analysis based method to calculate <i>RR</i> and $\mu_a$ , where pct is short for percentile.....	- 82 -
3.17. (a) The <i>RR</i> curve obtained with the statistical analysis based method. (b) The $\mu_a$ curve calculated from (a) is shown. ....	- 83 -
3.18. The flow chart of the frequency analysis based method to calculate <i>RR</i> and $\mu_a$ .....	- 83 -
3.19. (a) The <i>RR</i> curve obtained with the frequency analysis based method. (b) The $\mu_a$ curve calculated from (a) is shown. ....	- 84 -
4.1. (a) A customized <i>MR</i> breast coil is shown. (b) The side view of the <i>MR</i> breast coil in which the breast interface was fixed with a phantom in between and fibers	

attached to both sides. The small yellow packets stuck onto the breast interface were MR fiducial markers. ....	- 88 -
4.2. (a) The LABVIEW section to read the analog output of the vital sign monitor at the same speed as the NIR system is shown. (b) The LABVIEW section to read the 1 Hz digital output of the vital sign monitor is shown.....	- 90 -
4.3. The experimental setup for breast imaging inside the MRI, showing the laser diodes and spectrometers (left) with fiber coupling into the MRI system (center). Data collection was synchronized with finger pulse oximetry (right) to monitor pulsatile flow data in a frequency locked manner. ....	- 90 -
4.4. The flowchart of signal and data of the multi-modal experiment is shown. The spectrometers were connected with the computer through USB ports. The analog output of the pulse oximeter was connected to an I/O port of the DAQ board on the computer, and the digital output of the pulse oximeter was connected to the computer through 9-pin serial cable with RS-232 communication protocol....	- 91 -
4.5. The geometry of the heterogeneous phantom used for simulation is shown. The 2D mesh contained 5249 nodes, and was discretized into triangular elements....	- 92 -
4.6. The reconstructed $\mu a$ curves with 5% normally distributed noise are shown along with the true values, where (a) is for the anomaly region, and (b) is for the background region. ....	- 96 -
4.7. (a) The error in reconstructed $\mu a$ caused by normally distributed noise in the data is shown. (b) The error in reconstructed phase relation between the two regions caused by normally distributed noise in the data is shown.....	- 97 -
4.8. (a) The error in the reconstructed $\mu a$ caused by wrongly estimated horizontal position of the anomaly is shown. (b) The error in the reconstructed phase relation between the two regions caused by wrongly estimated horizontal position of the anomaly is shown.....	- 98 -
4.9. (a) The error in the reconstructed $\mu a$ caused by wrongly estimated vertical position of the anomaly is shown. (b) The error in the reconstructed phase relation between the two regions caused by wrongly estimated vertical position of the anomaly is shown. ....	- 99 -
4.10. (a) The error in the reconstructed $\mu a$ caused by wrongly estimated anomaly size is shown. (b) The error in the reconstructed phase relation between the two regions caused by wrongly estimated anomaly size is shown. The true radius of the anomaly was 10 mm. ....	- 100 -

- 4.11. (a) The error in the reconstructed  $\mu a$  caused by wrongly estimated homogeneous  $\mu s'$  is shown. (b) The error in the reconstructed phase relation between the two regions caused by wrongly estimated homogeneous  $\mu s'$  is shown. The true value of the homogeneous  $\mu s'$  was  $1.0 \text{ mm}^{-1}$ . ..... - 102 -
- 4.12. (a) The error in the reconstructed  $\mu a$  caused by the heterogeneity of  $\mu a$  and  $\mu s'$  in the heterogeneous phantom is shown. (b) The error in the reconstructed phase relation between the two regions caused by the heterogeneity of  $\mu a$  and  $\mu s'$  in the heterogeneous phantom is shown. .... - 104 -
- 4.13. (a) The error in the reconstructed  $\mu a$  caused by wrongly assumed  $\mu s'$  in the anomaly region is shown. (b) The error in reconstructed phase relation between the two regions caused by wrongly assumed  $\mu s'$  in the anomaly region is shown. The true  $\mu s'$  in the anomaly region was  $1.0 \text{ mm}^{-1}$ . ..... - 105 -
- 4.14. (a) The error in the reconstructed  $\mu a$  caused by wrongly assumed  $\mu s'$  in the background region is shown. (b) The error in the reconstructed phase relation between the two regions caused by wrongly assumed  $\mu s'$  in the background region is shown. The true  $\mu s'$  of the background region was  $0.6 \text{ mm}^{-1}$ . ..... - 106 -
- 4.15. (a) A breast MR image (coronal view) of the first healthy human subject is shown. (b) A finite element mesh generated from (a) was segmented into the fibroglandular region (white) and the adipose region (black) for region-based reconstruction..... - 109 -
- 4.16. (a) A 20-second data stream of the PO analog output in volt. (b) The FFT of the PO output. 20-second data stream of the detected signals from the 785 nm wavelength band of the NIR system for source 1 to detector 1, source 4 to detector 4, source 7 to detector 7 are plotted in (c), (e) and (g) respectively. Their FFT spectra are shown in (d), (f) and (h) respectively. .... - 110 -
- 4.17. 20-second data stream of the detected signals from the 830 nm wavelength band of the NIR system for source 1 to detector 1, source 4 to detector 4, source 7 to detector 7 are plotted in (a), (c) and (e). Their FFT spectra are shown in (b), (d) and (f) respectively. .... - 111 -
- 4.18. The recovered  $\mu a$  variations in the breast tissue of the first human subject are shown at 785 nm (a) and 830 nm (b), where the red curves are of the fibroglandular region, and the blue curves are of the adipose region. .... - 113 -

- 4.19. The peak frequency of the analog output of the PO along the time is shown, together with the peak frequencies of the reconstructed  $\Delta\mu a$  of the fibroglandular region at both wavelength bands.....- 114 -
- 4.20. The phase relation of  $\Delta\mu a$  of two breast tissue types of the first human subject at two wavelength bands is shown, with the PO analog output as the reference. All phases were unwrapped and shifted to be between  $-\pi$  and  $\pi$ , showing the extent the corresponding signal ahead of the PO analog output.....- 115 -
- 4.21. (a) A breast MR image (coronal view) of the second healthy human subject is shown. (b) A finite element mesh generated from (a) was segmented into the fibroglandular region (white) and the adipose region (black) for region-based reconstruction.....- 117 -
- 4.22. (a) A 15-second data stream of the PO analog output in volt. (b) The FFT of the PO output in (a). (c) 15-second data stream of the detected signal from source 4 to detector 4 at the 785 nm wavelength band. (d) The FFT of the signal in (c). (e) 15-second data stream of the detected signal from source 4 to detector 4 at the 830 nm wavelength band. (f) The FFT of the signal in (e).....- 118 -
- 4.23. The recovered  $\mu a$  variation in the breast tissue of the second human subject are shown at 785 nm (a) and 830 nm (b), where the red curves are of the fibroglandular region, and the blue curves are of the adipose region.....- 120 -
- 4.24. The peak frequency of the analog output of the PO along the time is shown, together with the peak frequencies of the reconstructed  $\Delta\mu a$  of the adipose region at both wavelength bands.....- 120 -
- 4.25. The phase relation of  $\Delta\mu a$  of two breast tissue types of the second human subject at two wavelength bands is shown, with the PO analog output as the reference. All phases were unwrapped and shifted to be between 00 and 3600, showing the extent the corresponding signal ahead of the PO analog output.....- 121 -
- 5.1. (a) The designs of the new breast interface [58] are shown from the profile side view (a), top view (b) and front view (c). (d) shows the fabricated product with lift bag and elastic in place. The upper holes are for the fibers of the multi-wavelength NIR system, and the lower holes are for the high-speed NIR system. ....- 127 -
- 5.2. Dynamic changes of (a) Hb, (b) of a subject under stimulation of 5 min. of hypercarbia & hyperoxia followed by 5 min hyperoxia imaging [93]. ....- 128 -

- 5.3. (a) Schematic diagram of the breast interface of a CW NIR system developed at UPenn [62]. (b) Time course of ICG concentration curves for a specific voxel in three patients [96]. .....- 129 -
- 5.4. The relationship of  $\mu a$  of ICG and 0.75% intralipid mixture at two wavelengths with regard to the concentration of ICG is shown. ....- 130 -

## *List of Acronyms*

Avalanche Photodiode	APD
Charged-Coupled Device	CCD
Continuous Wave	CW
Data Acquisition	DAQ
Diffuse Optical Spectroscopy	DOS
Diffuse Optical Tomography	DOT
Frequency Domain	FD
Fast Fourier Transform	FFT
Reduced Hemoglobin	Hb
Oxyhemoglobin	HbO
Heartbeat Rate	HBR
Total Hemoglobin	
Indocyanine Green	ICG
Laser Diode	LD
Magnetic Resonance	MR
Normally Distributed	ND
Near-Infrared	NIR
Phosphate Buffered Saline	PBS
Pulse Oximeter	PO
Region Of Interest	ROI
The Ratio Of Two Ratios	RR
Superluminescent Diode	SLD

Signal To Noise Ratio

SNR

Oxygen Saturation

# **Chapter 1. Introduction**

## **1.1 Overview**

Near-infrared spectral tomography has been extensively studied to measure functional properties of breast tissue, with an aim of providing fundamental insight or diagnostic information about breast cancer management [1]. This study describes the technology and methodology to build a high-performance high-speed dual-wavelength near-infrared (NIR) tomography system to quantify the temporal absorption contrast available in breast tissue. The technological focus is to refine a system that is capable of recovering real-time hemoglobin content and oxygen saturation within tissue, by means of synchronized high-speed detection of spectrally-encoded laser sources in two wavelength bands. To improve the accurate and the resolution of the high-speed reconstruction results, the NIR system was integrated into a clinical magnetic resonance (MR) system, and synchronized with a finger pulse oximeter (PO). Two healthy human subjects were examined with this multi-modal design, and the results proved this multi-modality design can recover the small pulsatile variation of absorption property in breast tissue related to the heartbeat. And it also showed the system's ability on novel contrast imaging of fast flow signals in deep tissue.

## **1.2 Breast Cancer and Current Clinical Imaging Techniques**

Breast cancer is the 2nd most common cancer diagnosed among women, excluding skin cancer. It is estimated that there will be 207,090 new cases and 39,840 deaths from breast cancer in the United States in 2010 [2]. One key to decrease the death rate of breast

cancer is early diagnosis, simply because all cancers have much higher probability to be cured when they are detected at an early stage. In a statistical analysis carried out by National Cancer Institute, considering all women diagnosed between 1996 and 2003, the 5-year survival rate was 98% for those with localized disease, 84% for those with regional disease, and 27% for those with distant-stage disease [3], as shown in Figure 1.1. Therefore, biennial screening mammography is strongly recommended by the U.S. Preventive Services Task Force for women between the ages of 50 and 74 years [4].

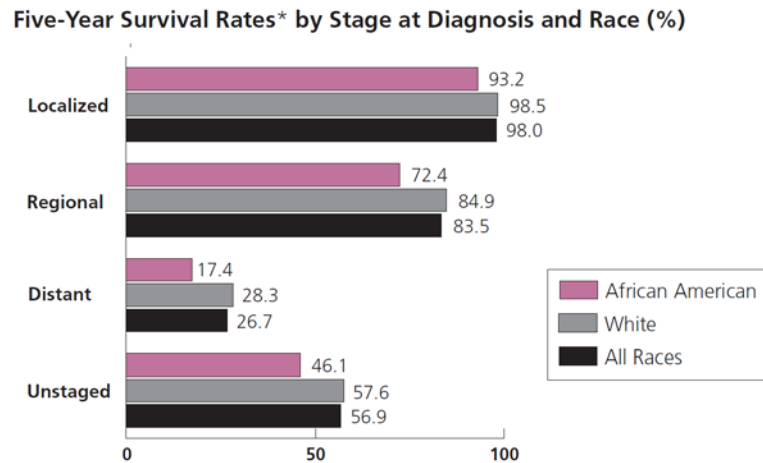


Figure 1.1. Five-Year Survival Rates by Stage at Diagnosis and Race [3]

The most widely adopted technique of breast imaging is x-ray mammography, which is the standard tool of biennial screening for early detection of breast cancer [5]. This technique uses low-energy X-rays to image the compressed breast, and a projected image of the internal interaction coefficients within tissue is developed. On average, mammography will detect about 80%-90% of breast cancers in women without symptoms [3], and it has been studied in many randomized blinded clinical trials to show that its regular use in screening can lead to decreased deaths from breast cancer [6-8]. But mammography still comes with higher false-negative and false-positive, especially for

dense breast tissue which is common in women prior to menopause. About 20% of all breast cancers are missed [9], and statistically there would be 55 additional false-positive screens for each additional breast cancer detected [10], which results in large portion of unnecessary biopsy procedures.

MRI is even more sensitive than mammography, but it is utilized at a cost of higher false-positive results, and very high economic cost [11]. The imaging exam involves injection of Gd-based contrast agent, which is known to have a slight morbidity risk in patients with compromised kidney function [12]. So MRI is only recommended as a supplement for mammography in complex cases, or for women in pre-defined categories that are at higher-risk for onset of familial cancers [13].

Ultrasound has been accepted only as a complementary method, because of its unique effectiveness in distinguishing between fluid-filled cysts and solid tumors [14], and its high operator dependence. It has not been proven as a useful screening standard beyond this application [15].

Other emerging techniques, such as positron emission tomography (PET) scan and Electrical Impedance Scanning are still under clinical trial and evaluation [14]. The routine acceptance of these does not appear to be in the immediate future, and conclusive multicenter trials have not been performed.

### **1.3 Development of Optical Imaging & Pulse Oximetry**

The non-invasive and non-ionizing features of biomedical optics have long attracted the investigative work of researchers. The first optical transillumination experiment to document the imaging of breast tumors was done as early as 1920s', prior to the use of x-ray imaging, but the images were blurry because of the high scattering in

breast tissue [16]. Due to the physical limitations of light scattering in tissue, as well as limitations in instrumentation, algorithms and computational capacity, the application of biomedical optical imaging was very limited [17].

At the same time, research of measuring optical absorbance in tissues to monitor oxygenation found its niche and kept moving forward. Human cell function is sustained by oxygen transport, and lack of oxygen can quickly lead to irreversible damage to cell tissue, and this damage is even bigger for cell tissue with a high metabolic rate. Skeletal muscle can survive for 2 hours after anoxia, but the heart can only remain ischemic for 5 minutes, and cerebral cortex will be damaged in less than 1 minute [18]. Therefore oxygenation information is always important in clinical work and physiological research fields. Traditional methods to measure oxygen content in blood are chemical reaction based, such as the Van Slyke method and use of the Clark electrode [19]. Although very accurate, these methods are very slow and can only be used in vitro, and no continuous monitoring can be performed. The first reliable oximeter didn't present itself until 1976 when HP marketed its ear oximeter HP47201A. This oximeter didn't require calibration by squeezing blood from the ear like earlier oximeters, and its accuracy was improved by using 8 wavelengths. It was served as a "gold standard" for oximetry for a long time. But still it was large and heavy, and had a bulky, awkward earpiece [20].

In 1972, Takuo Aoyagi, a bioengineer, invented the method to measure a ratio of red to infrared light absorption through tissue, extracting out the pulsating components [21]. This methodology gave birth to a kind of small and easy-to-use device called pulse oximeter which can provide accurate, continuous and real-time oxygen saturation monitoring. However, the oxygen saturation level measured by a pulse oximeter, usually

represented by  $S_pO_2$ , is the percent of hemoglobin molecules bound with oxygen molecules only in the pulsing arterial blood, and those of venous blood, skin, bone, muscle, fat are all excluded. Pulse oximetry is different from another optical imaging technique called NIR spectroscopy which will be discussed in section 1.4, because the oxygen saturation value recovered by the latter technique is a ratio of oxygenated hemoglobin to total hemoglobin in the microcirculation of a volume of illuminated tissue, and is represented as in this thesis.

Typically two LDs at 660 nm and 940 nm are placed on one side of a pulse oximeter as the light sources. And two detectors are placed on the other side, which typically are photodiodes with optical filters in front to block light of either wavelength. After a pulse oximeter is attached to a finger or earlobe of the patient, the pulsation of optical signal at both wavelengths are measured at high speed, typically in the kHz range. For each wavelength, the ratio of the pulsing part of the signal versus the static part is calculated. Then one ratio is divided by the other, and the resulting number can be related to through beer's law, although calibration is needed in practice.

This approach to measure oxygen saturation from arterial blood flow pulsation is delicate and useful for regional measurements of physiological health, and is the principle for current generation of commercial pulse oximeters. The "next generation" pulse oximeters are still based on this principle, but can effectively reduce motion artifacts by introducing more complicated signal processing algorithms. An example is the adaptive filter technique by Masimo to model and remove the motion noise from the signal in real-time [22]. Current light transport models techniques, including Monte Carlo simulations

and/or the diffusion equation, can be used to estimate signals but generally still require significant calibration effort to be useful in routine clinical use.

Although only the oxygen level in the arterial blood is measured, nowadays pulse oximeters have found enormous utilities in the measurement of oxygen saturation in vivo, and have become critically important in emergency medicine. Typical applications include anoxia monitoring during surgery under anesthesia, arterial oxygen saturation monitoring of both the mother and the fetus during childbirth, sleep and physical stress studies [19].

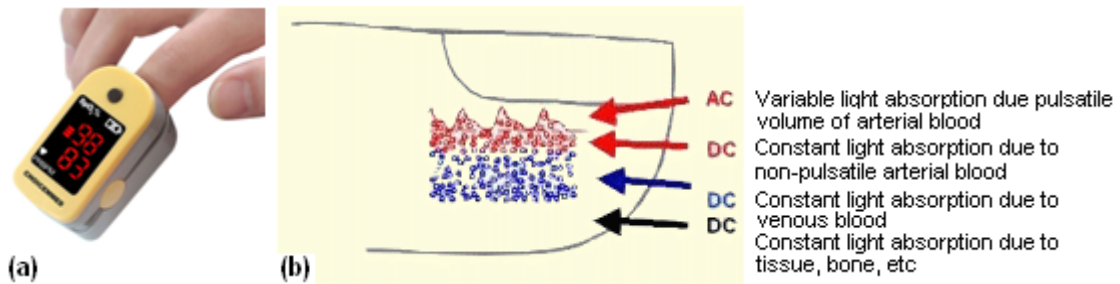


Figure 1.2. Pulse oximeter. (a) a typical fingertip pulse oximeter.(b) Light Absorbance in a finger [20].

#### 1.4 NIR Spectroscopy of Tissue

Unlike X-ray which propagates through breast tissue with a weak Compton scatter and photoelectric effect attenuation, the path optical photons take in tissue is much more scatter dominated by elastic Mie scattering events. Absorption and scattering events accompany incident photons all the way, and the probability of these events depends on two factors, e.g. the wavelength of incident photons and optical property of local tissue. The primary light absorbers in breast tissue, called chromophores, include oxyhemoglobin (HbO), reduced hemoglobin (Hb), water and lipid. And their absorbing

spectra as a function of wavelength are very different, as shown in Figure 1.3. The “NIR spectral window” between 650nm and 900nm provides a region with relatively low absorbance, and offers the possibility for NIR photons to penetrate several centimeters in depth and provide transmitted information about the tissue in between.

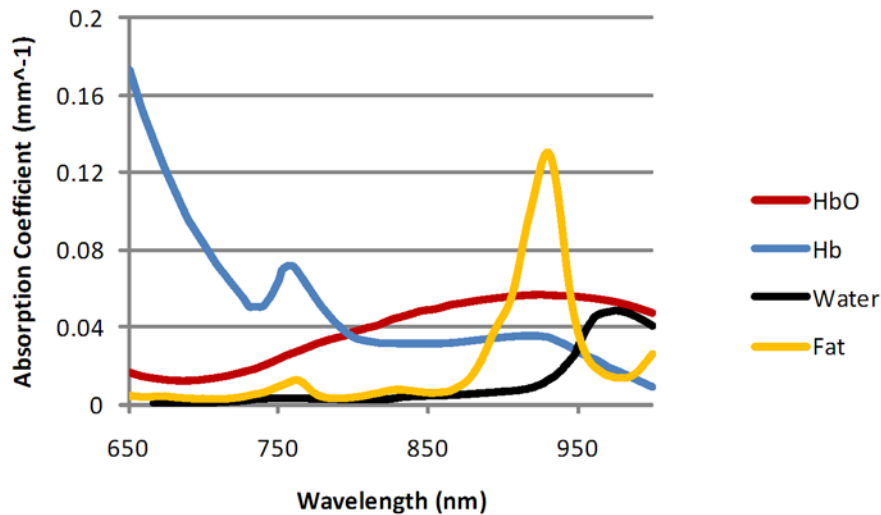


Figure 1.3. The absorption spectrum per unit molar concentration of HbO, Hb, water and fat. Data was taken from Oregon Medical Laser Center. Absorption coefficients of HbO and Hb are calculated with concentration of  $0.2 (mM)^{-1} \cdot mm^{-1}$ .

The pathology of breast cancer varies widely with up to 18 different phenotypes being known. But generally it is agreed that after a small breast tumor switches to an angiogenic phenotype, large amount of abnormal and leaky blood vessels begin to form with reversed and intermittent flow, which finally leads to hypoxic regions within the tumor [23, 24]. The increased vasculature density and clogged blood circulation within the breast tumor distinguish the tumor from surrounding tissue by increased hemoglobin levels and potentially decreased oxygen saturation, and this critical pathophysiologic information could be detected by NIR optical tomography. Images of breast lesions to

date, indicate that total hemoglobin-based contrast can be up to twice the value of normal tissue in the same breast, which perhaps is higher than the intrinsic contrast of any other imaging modality [25].

## 1.5 Current Status of NIR Breast Cancer Imaging

Research into the use of NIR in breast cancer management can be divided into two categories, diffuse optical spectroscopy (DOS) which emphasizes on obtaining the averaged quantitative optical parameters of the interested region, and diffuse optical tomography (DOT) which aims at reconstructing the spatial images of optical parameters or chromophores concentrations of the whole tissue region.

Research at the Beckman Laser Institute at the University of California, Irvine, has been devoted to development and propagation of a handheld DOS breast imaging device. It is based on the concept of frequency-domain spectroscopy, typically using 6 [26, 27] to 8 [28, 29] laser diodes with wavelengths ranging from 672 nm to 978 nm that are modulated from 300 MHz to 1 GHz as sources, and are coupled into a source fiber through an 8x8 optical multiplexer [29]. The detector is an avalanche photodiode (APD) placed 3 cm from the source. Based on the analytic solution of an assumed semi-infinite geometry using diffusion equation,  $\mu_a$  and  $\mu'_s$  are calculated on each wavelength, and the concentration of chromophores can be obtained through least-squares fitting [30, 31]. Additionally, the system uses steady-state transmission measurements from a halogen lamp as a wide-spectrum (650~1000nm) continuous wave (CW) source, added onto the frequency domain (FD) system. This DOS system is able to pick up the different optical properties on malignant breasts and corresponding normal breasts [27, 29, 31, 32], and the pre- and post-menopausal normal breast [29, 33], but it is not easy to provide a

convincing criterion to distinguish breast tumor. The main reason is that the sensitivity of DOS depends on the fraction of signal resulting from diseased tissue versus surrounding healthy tissue, and will be skewed with the depth. Besides, result of this hand held device may vary for 5% for different operators [26]. Despite these limitations, the system is being put into use in a multicenter trial to track the patient response to neoadjuvant chemotherapy, to determine if it could reliably provide prognostic information about those patients who are not responding to therapy. This trial is just initiating, and Dartmouth will be a participating site.

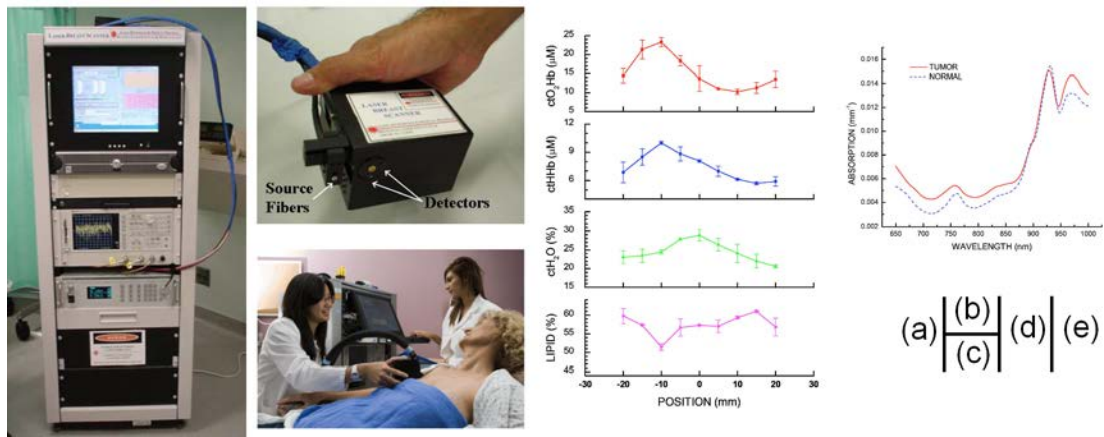


Figure 1.4. (a) The NIR spectroscopy system developed by the UCI group. (b) The handheld scanner. (c) A patient was scanned by the handheld scanner. (d) Line scan result of four major chromophores of a tumor. (e) Fitted  $\mu_a$  v.s. wavelength of normal tissue and tumor [1, 27].

Researchers at Dartmouth have been working on DOT since 1995 when Paulsen and Jiang demonstrated the approach to reconstruct images with NIR transmission light. Pogue et al used modulated light at 751 nm LD at 150 MHz and inserted it around a cylindrical phantom to successfully recover an anomaly inside with 2:1 contrast [34, 35].

Jiang et al reported better reconstructed images with dual mesh scheme [36]. Later a three-wavelength NIR tomography system was built and tested on phantoms and patients. With assumptions about water and lipid content, the first in vivo HbO and Hb concentration recovery was realized [37]. The system was greatly upgraded in 2001 into a fully automatic multi-wavelength breast tomography imaging system, with 16 sources, 16 PMT detectors and 5 wavelengths, and one-plane imaging per wavelength could be finished within 30 seconds [38]. Many patient exams followed, showing localized hemoglobin contrasts near 2:1 were readily detected and quantified [39-43]. Wang et al further proved that superior recovery was possible using more wavelengths [44] and longer wavelengths [45].

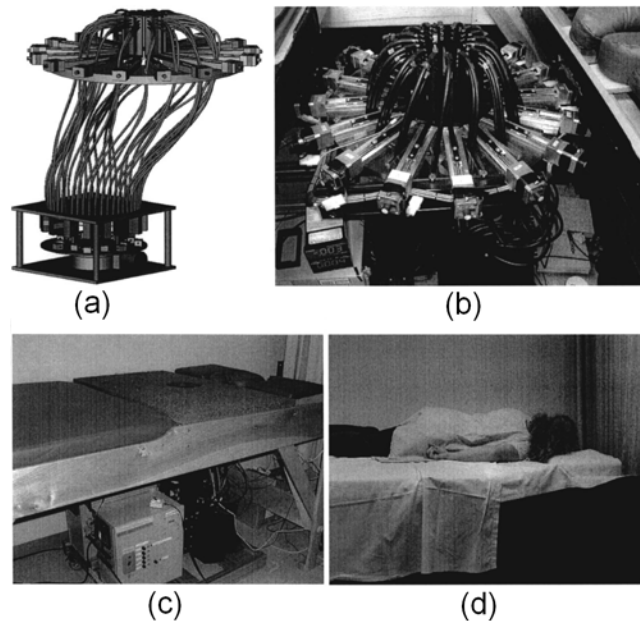


Figure 1.5. (a) An engineering drawing of the optical source and detection subsystem. The upper circular region holds three rings of sixteen fiber bundles each, mounted to sixteen linear translation stages. The tomography imaging is achieved by cycling the laser source into each fiber sequentially through the circular

translation stage on the bottom. (b) The fiber-optical interface. (c) The patient bed with imaging system underneath. (d) A female subject positioned on the table with her breast in the imaging array [25].

Research at the University of Pennsylvania has been focused on a three-dimensional parallel plate tomography system. To balance the building cost and the need for a large amount of dataset which is essential for 3-D reconstruction, CW measurements were chosen. A charged-coupled device (CCD) chip was used and divided into many detection regions that functioned like smaller detectors. 6 optimal wavelengths ranging between 650 nm and 905 nm were chosen based on their calculation [46, 47]. There are 45 source fibers which switch between 6 wavelengths, and the CCD chip is divided into 984 smaller regions. This configuration resulted in almost CW measurements per wavelength, which are much more than other 3-D DOT systems [48]. To address the limitation of CW measurement to differentiate scattering and absorption, a relatively limited number of frequency domain measurements were integrated with 9 APDs to calculate the averaged absorption and scattering coefficients, and provide a homogenous initial guess for the reconstruction of CW data [48, 49]. Instead of using the common Newton-type reconstruction approach, they applied a gradient-based algorithm to overcome memory limit [47], and parallel computing was implemented to reduce the computation time.

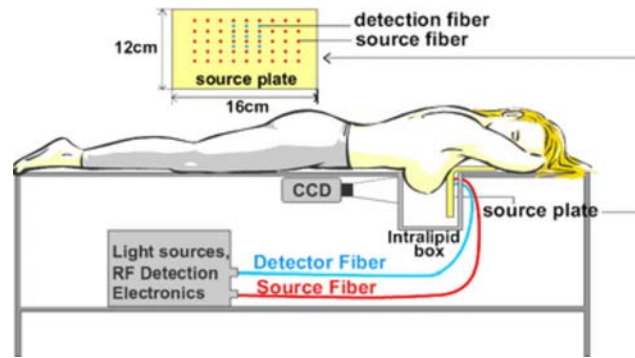


Figure 1.6. A schematic of the NIR imaging system at University of Pennsylvania [1].

Although no convincing clinical diagnostic criterion has been proposed and discrepancy still exists in the results of patient exams, these systems did confirm the possibility of using hemoglobin content, oxygen saturation, water concentration and scattering coefficient to provide diagnostic information to differentiate normal and malignant tumors, despite that conclusive demonstration of where NIR breast imaging would fit into breast cancer management still remains undetermined [25, 27, 29, 32, 43, 48-50]. Most centers have ongoing work in following response to neoadjuvant chemotherapy as the most likely clinical outlet in the near future.

## 1.6 Multimodal Imaging System

Despite the effort and advances stated above about breast spectroscopy, imaging with NIR light still suffers from low resolution due to the diffuse nature of photons within the tissue. Additionally the cost, complexity and imaging time do not allow unlimited increase of source-detector measurements or wavelengths. To address this problem, the concept of utilizing multiple imaging modalities was proposed, which makes use of the higher resolution anatomical structure information from another imaging modality as spatial priors to constrain algorithm convergence and resolution of the NIR system. MRI

has been the most common choice to combine with DOT systems and it was shown to improve the quantification of the DOT inverse algorithm [51-53]. There are hybrid systems like tomosynthesis/NIR [54] and Ultrasound/NIR [55-57] as well.

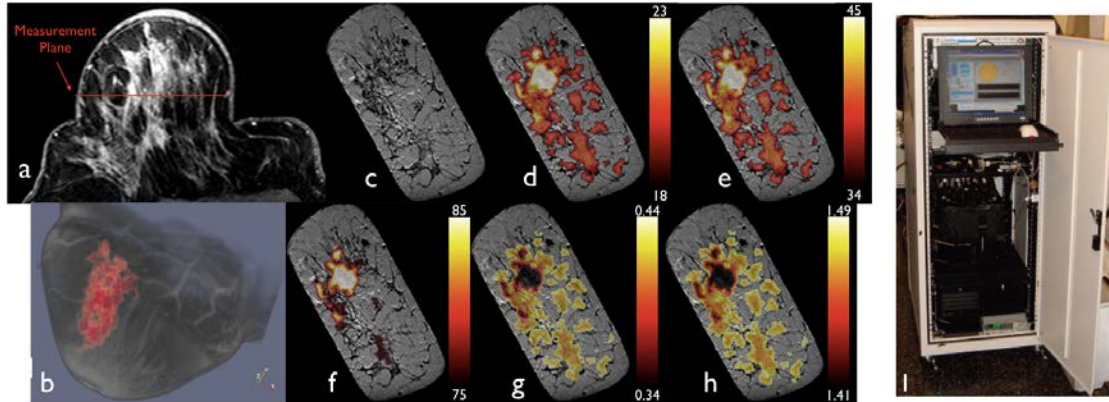


Figure 1.7. Result of an patient exam using MR/NIR hybrid imaging [58]. Axial MR imaging showing coronal plane of optical imaging (a). Panel (b) shows a 3D representation of combined maximum intensity projection MR image and 3D rendering of optical solution of HbT. Optical solutions for HbT (d), water (e), oxygen saturation (f), scatter amplitude (g), and scatter power (h), are shown overlaid on top of coronal MR (c). In each case the background value is removed. (I) shows the multi-wavelength NIR system used in this experiment.

## 1.7 High-speed NIR Tomography of Breast Tissue

Most researches so far have been focused on optimizing imaging qualities of breast tissue, including optimizing selected wavelengths, incorporating more wavelengths, and integrating with another imaging modality to make use of the structure information in reconstruction [51, 59-61]. The reconstructed images usually can show regions with abnormally higher hemoglobin content or lower oxygen saturation, which could be the

sign of tumor existence and thus could potentially provide useful diagnostic information. In addition, dynamic contrast mechanisms in breast tissue, such as those from optical contrast agent pharmacodynamics [62] or rapid vascular changes induced from gas inhalation changes [63, 64] are under exploration to improve image contrast and specificity. These functional contrast changes have induction curves which change rapidly over seconds and minutes and thus require faster imaging systems to capture the physiologically critical information about vascular dynamics and resistance with biologically accurate temporal resolution. The heartbeat of human is the main driving force of pulsatile blood flow and hemoglobin change in organs, including extremities such as the breast. To relate these, the minimum imaging speed should be at least 3 Hz. But currently most NIR systems used in clinical trials require several minutes to acquire one image, and the time-averaged information in these images simply cannot reflect the temporal changes of blood volume and oxygenation in the suspicious region. Only a few NIR tomography systems can image at high speed, and they can be categorized into two typical designs.

The first and more straightforward design is to switch sources one after the other by source positions and wavelengths, while keeping all detectors on. Suppose the required exposure time is  $T_{expose}$ , switch time is  $T_{switch}$ , the number of sources positions is  $n_{src\_pos}$ , and the number of wavelengths is  $n_{wv}$ , then the operation frequency  $f_1$  is:

$$f_1 = \frac{1}{(T_{expose} + T_{switch}) \times (n_{src\_pos} \times n_{wv} - 1)} \quad (1.1)$$

An improved design modulates laser beams of different wavelengths at different low frequencies and focused into one source fiber. This mixed signal can then be demodulated at the detection side. In this way  $n_{wv}$  in equation 1.1 equals to one, and

imaging speed can be greatly improved. A system built by Schmitz et al [65] is shown in Figure 1.8(a), and the operational speed is 3 Hz with 16 sources at 2 wavelengths. Source positions can be modulated in a similar manner as well. One such system realized by Joseph has 32 modulated sources [59, 66], although its imaging speed was not mentioned. Generally this frequency modulation design is stable and ultra-flexible. The disadvantages of this design include compromised detection dynamic range with more source positions or wavelengths, and the easily overwhelmed weaker signal from distal sources by strong signals from closer sources. The measurements of one frame cannot be taken at the same time either. Thus this design is not very suitable for high speed imaging of large tissue volumes such as the human breast.

The second method is to light on all sources of the same wavelength while keeping all detectors open. This technique was first realized by Piao et al [67-69] and the system design is shown in Figure 1.8(b). The eight sources in this system were not exactly of the same wavelength. Instead they were spectral-encoded to have about 1 nm distance in between which was realized by precise control of the temperature and current of individual laser diode to shift its wavelength. The optical properties are assumed to be the same across this narrow wavelength range in calculation, which may bring in small errors. A 1200 grooves/mm grating was used before the CCD detector to separate signals from each source and project them onto the CCD sensor. In this spectral-encoding design, no mechanic switching is involved, thus the system is stable and ultra-fast. The operation frequency  $f_2$  is:

$$f_2 = \frac{1}{T_{expose}} \quad (1.2)$$

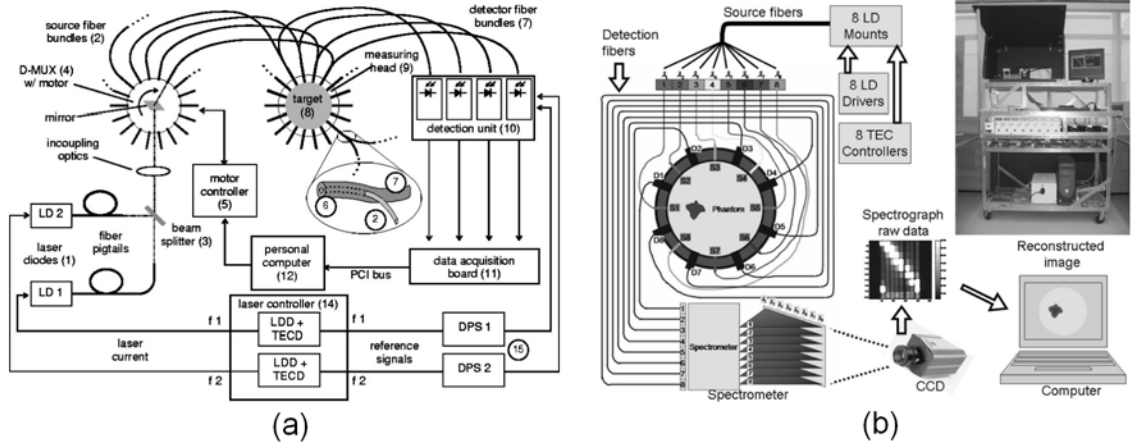


Figure 1.8. (a) Block diagram of the instrument setup using source switching method [65]. (b) Schematic diagram of the NIR tomography system by spectrally encoded parallel source delivery [67].

It is obvious that this method can potentially be much faster than the first method since it is not influenced by the number of sources or detectors at all. Piao's system has shown the ability to reach a high speed of 35 Hz with satisfactory signal to noise ratio when imaging a small cylindrical phantom [67]. Piao further replaced the 8 laser diodes with a coherent superluminescent diode (SLD) with 14.2 nm FWHM bandwidth. The SLD output beam was dispersed by a 1200 g/l grating and collimated onto eight linearly aligned fibers to form eight sources with slightly different wavelengths. This design is much more compact and thus feasible for endoscopic prostate imaging [57, 70, 71]. The advantage of this spectral-encoding design is its ultra-high speed. And oversampling is always good for improving signal to noise ratio (SNR). The disadvantages of this design include the following:

- The number of sources cannot be large, because too wide wavelength coverage will invalidate the assumption of identical optical properties in this range, and settling many laser diodes in the narrow wavelength range is difficult;
- Mode-hopping of laser diodes which is hard to be completely removed;
- Settling more than two wavelengths is hard for this design, because the high density grating leads to narrow wavelength coverage on the CCD.

Considering the need for high speed imaging to catch pulsatile signals in breast, the second method was chosen in this thesis work. And one additional wavelength was added onto the system to monitor the temporal absorption change caused by pulsatile blood flow in breasts, as stated in Chapter 4. The structure of this thesis is as follows:

Chapter 2 described the instrumentation of the single wavelength video-rate tomography system which can image through tissue-like media of seven centimeters thick at 20 Hz. Both static and dynamic phantom experiments were carried out, and several reconstruction schemes were compared and discussed.

Chapter 3 presented the dual-wavelength video-rate tomography system, whose capacity of recovering temporal hemoglobin content and oxygen saturation with given scattering coefficients was demonstrated through phantom experiments.

Chapter 4 started with the error analysis with the multimodal clinical imaging setup. Then the results and physiological implication from the clinical imaging experiments of two healthy human subjects were display and discussed.

Chapter 5 summarized the thesis work. Possible clinical applications and future work were discussed.

## **Chapter 2. Video-rate Single Wavelength Tomography System**

High-speed near-infrared spectral tomography of tissue can be used to measure functional activities of tissues such as metabolic changes or hemodynamic events, or the dynamic injection and tracking of optical contrast agents. The frequencies of these activities are either directly driven by or are closely related to the heartbeat rate. Therefore to accurately record many of these corresponding signals in humans, the minimum imaging speed should be at least several Hertz, and ideally the higher the better, because imaging at a higher speed provides quantitative information with higher SNR, and potentially allows the use of signal processing methods to improve the SNR. Additionally the waveform generated by the heartbeat is not sinusoidal, and contains significant higher frequency content in it. Thus, an ideal fast imaging system would allow capture of this higher frequency content as well, so as to maximize the information obtained.

Two designs that can reach 3Hz have been fully discussed in chapter 1.7. The system with a source-switching design can acquire data with at 3 Hz rate, with 10 ms exposure time for each source position [65]. The system designed with spectrally-encoded light sources can be run at above 30 Hz acquisition rate. But until recently it was limited to small animal imaging, mostly due to dynamic range limitations in the circular geometry. Now with careful modifications, it has the potential to image through thick tissue, with an acquisition rate several fold higher than that of the human heartbeat.

The new system has the same eight spectrally-encoded laser diode sources but it is used in a slab-shaped interface with one dedicated spectrometer with a cooled CCD

detector at each channel. Eight spectrometers that are synchronized through external TTL trigger signals were used, providing much better signal to noise ratio than the previous effort where all channels were fed into a single spectrometer-CCD [68]. The use of a parallel plate slab geometry is also important, because the intensities of the signals that propagate from all sources to the same detector location are then all closer in value, allowing a much smaller dynamic range than the conventional circular design. The system was constructed and tested in tissue-like phantoms, the performance was characterized, and the implications and planned use are discussed in this chapter. The system has the capacity to image through up to 8 cm of soft tissue, which would make it possible to be used to track the variation of absorption caused by hemodynamics in peripheral limbs, breast tissue or part of the cranium, although breast tissue is the main target for this study.

## **2.1 System Configuration**

The video-rate single wavelength tomography system illustrated in Figure 2.1 consisted of several sub systems. Eight spectrally-encoded laser diodes (LD) each with a temperature control module and a current control module were integrated on to a source cart. Eight fiber-coupled spectrometers, each equipped with a 1200 grooves/mm grating and a high-resolution CCD, were integrated on to a detection cart and set to respond to an external TTL trigger signal. The TTL trigger signal was generated by a data acquisition (DAQ) board from National Instrument and programmed through LABVIEW software. A splitter circuit was customized to convey the TTL trigger signal into eight channels and finally to the EXT SYNC port on each CCD simultaneously. Imaging data is collected by the same LABVIEW program and transferred back to the console computer through USB

connection with the CCDs. A customized flexible fiber mount and phantom/tissue interface was built to hold the phantom in the parallel plate slab geometry with the fibers in contact with it. Each component will be described in detail below.

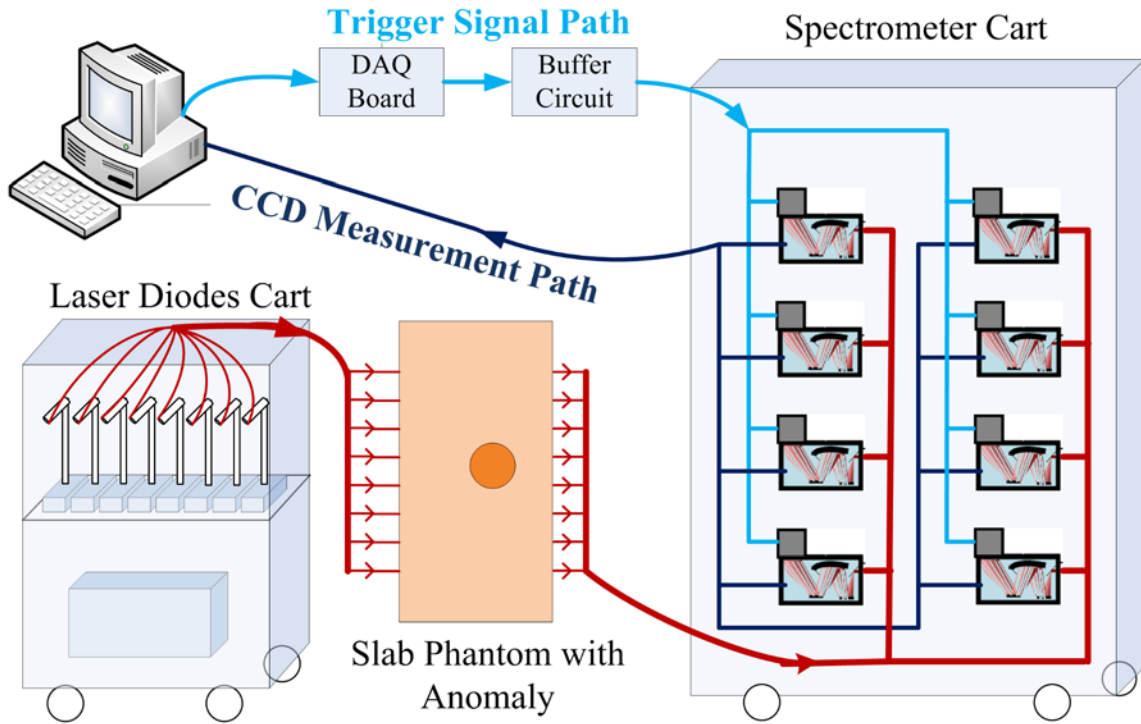


Figure 2.1. A diagram of the video-rate near infrared tomography system is shown. Eight spectrally encoded LD systems were integrated onto one cart. Eight fiber-coupled spectrometers with high-resolution CCDs are integrated onto another cart and set to respond to an external TTL trigger signal. The signal is generated by a data acquisition board and then split into eight channels by a customized splitter circuit, and delivered to the EXT SYNC port on each CCD simultaneously. Imaging data is transferred back to the computer for post processing. A flexible fiber mount is customized to hold the phantom or tissue in between.

### 2.1.1 Spectrally encoded sources

In conventional NIR tomography systems sources are often launched in sequence to avoid mutual interference at detectors, so the time needed for one image is proportional to the number of sources in use, unless temporal or frequency encoding methods are used to carefully overlap the signals in a way in which they can be extracted from the overlapping signals. The new video-rate single-wavelength tomography system uses 8 identical single mode CW LDs (Hitachi HL-7851G) whose nominal center wavelength is 785 nm, and the scheme was to shift the wavelength of individual LD to have approximately 1 to 2 nm interval in between, so that all LDs would be spectrally-encoded and could lase at the same time. In this manner, there is no source switching and the imaging speed can be greatly improved.

Two factors determine the center lasing wavelength of one LD, the laser case temperature and the drive current. Change in the case temperature affects the band gap of the semiconductor junction and therefore the peak wavelength of the laser cavity gain profile. Change in the drive current alters the current density and the instantaneous temperature in the laser junction, which will vary the refractive index of the junction material and therefore the effective cavity length [72]. Because the drive current above threshold level is almost proportional to the lasing power which is strictly limited for human related experiments, case temperature became the main approach to shift the lasing wavelengths of LDs.

According to the datasheet of Hitachi HL-7851G [73], its lasing wavelength can shift from 775 nm to 795 nm by varying its case temperature from -10 oC to 60 oC. So the tunable range was wide enough for our design. But experimentally it was found that

the lasing wavelengths of the LDs were unstable for most of the temperature range because of the existence of mode hopping. The wavelengths of adjacent LDs easily hopped between lasing modes and frequently mixed with each other, which led to the failure of the spectral encoding scheme.

Mode hopping arises when several modes close to each other are competing. This has been a very troublesome issue for LD applications and many factors could come into play, of which the most important factors are the case temperature, the drive current and optical feedback. The optical feedback is the reflection of the laser beam back into the laser cavity, and a quick solution to avoid it is to use distributed feedback LDs. But the unit price of this LD is around \$2000, and it would be too expensive if we used eight for our application. A previous study [74] showed that the lasing wavelength of a LD could be stabilized under certain combinations of case temperature and drive current. But the good combinations are unpredictable and vary laser by laser, and trial-and-error was the only solution. Another layer of complexity was that the “sweet points“ of certain LDs might be overlapped, in which case additional LDs would have to be tried to solve the conflict.

This process was tedious and very time-consuming, but finally eight LDs were chosen and spectrally encoded to have approximately 1.5 nm interval in between. The control of the case temperature was realized by a temperature control board (TCM1000T, Thorlabs, NJ) and a TE-Cooled mount (TCLDM9, Thorlabs, NJ), and the control of drive current was operated by a current control board (LD1255, Thorlabs, NJ). All the LDs and accompanying temperature and current control circuits are installed on a customized cart, as shown in Figure 2.2.

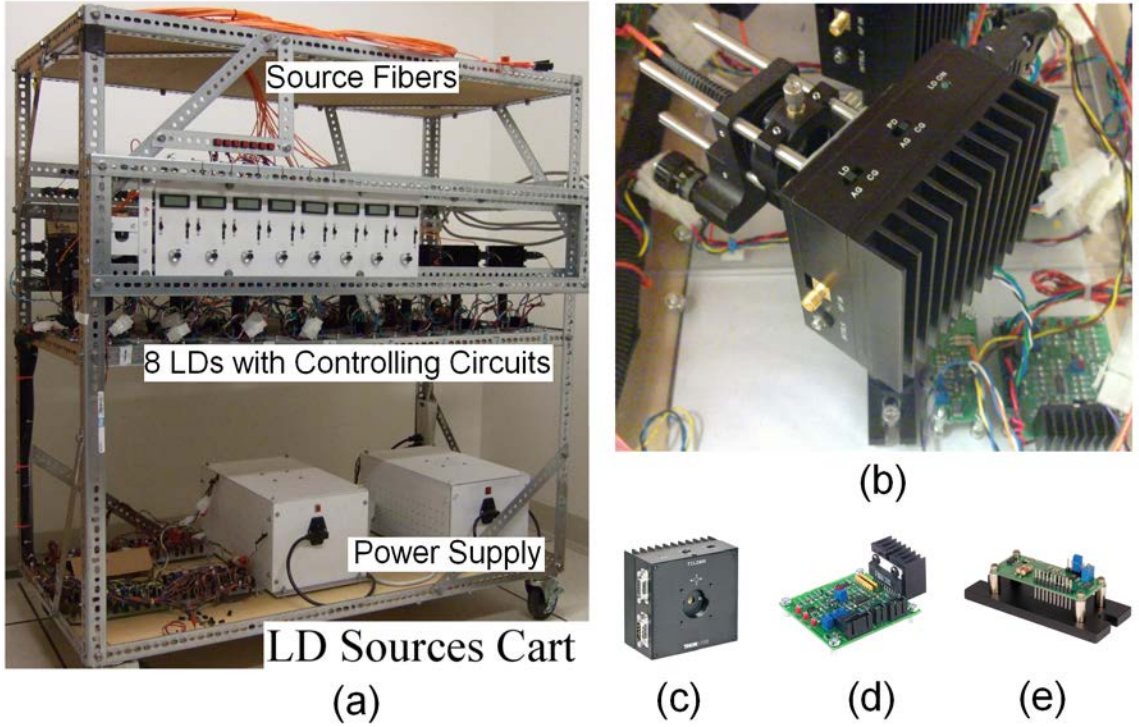


Figure 2.2. (a) The customized cart sitting 8 spectrally encoded LDs [67]. (b) A LD with its supporting components. (c) The TE-Cooled mount. (d) The temperature control board. (e) The drive current control board.

Table 2.1. The optimal current and temperature settings for 785 nm LDs.

LD index	$I_{knob}$	$T_{set}$	$T_{act}$
1	0.494	1.654	1.654
2	0.540	1.394	1.394
3	0.410	1.408	1.408
4	0.664	1.226	1.226
5	0.378	0.817	0.817
6	0.546	1.179	1.179
7	1.000	0.574	0.608
8	0.778	0.968	0.971

The optimal current and temperature settings are listed in Table 2.1.  $I_{knob}$  is the current setting on the rotating knob for the LDs. The knob has a range of 0.02 to 1.00 with 0.02 resolution. The actual LD current corresponding to this value can be measured

on the current control board.  $T_{set}$  is the preset temperature for a LD, and  $T_{act}$  is its actual temperature. The temperature corresponding to  $T_{set}$  and  $T_{set}$  can be calculated from a characteristic curve of the temperature control board. It has to be noted that these settings may need retuning every several months to compensate for the device aging.

The 1.5 nm interval is wide enough for the 1200 grooves/mm grating on the CCDs to separate source signals clearly, so all source LDs can be launched simultaneously to improve imaging speed without interfering with each other. Meanwhile the interval is so narrow that the maximum difference of the absorption coefficient in the whole range is within 5% for whole blood. Therefore the optical properties of the tissue can be treated as constant within the wavelength range.

The stability of the intensity and the wavelength of the 785 nm LDs were both tested by continuously sampling for 15 minutes. The 8 LDs were attached to a slab-shaped homogeneous phantom through fibers, and one spectrometer was coupled to the phantom through a detection fiber. CCD image frames were continuously recorded for 15 minutes at an exposure rate of 10 frames/second. The output intensities of the 8 LDs with regard to time are shown in Figure 2.3(a). The offset intensity differences between the 8 LD sources were simply caused by differences in LD output power and source-detector distances. The intensities of the LDs were normalized to their mean individual values. Then the standard deviation was calculated for each LD and the results are displayed in Figure 2.3(c), where six of the eight LDs show 0.7% to 0.8% variation, and one LD shows a variation slightly above 1%. Similar analysis was performed on the peak positions of the LDs spectra, and the results are shown in Figure 2.3(b) to (d). The wavelength stability is much better compared to that of the intensity, where the maximum

standard deviation of wavelength is only 0.022 nm over these acquisition times, and is thought to be good enough to avoid spectra mixture caused by mode hopping of LDs.

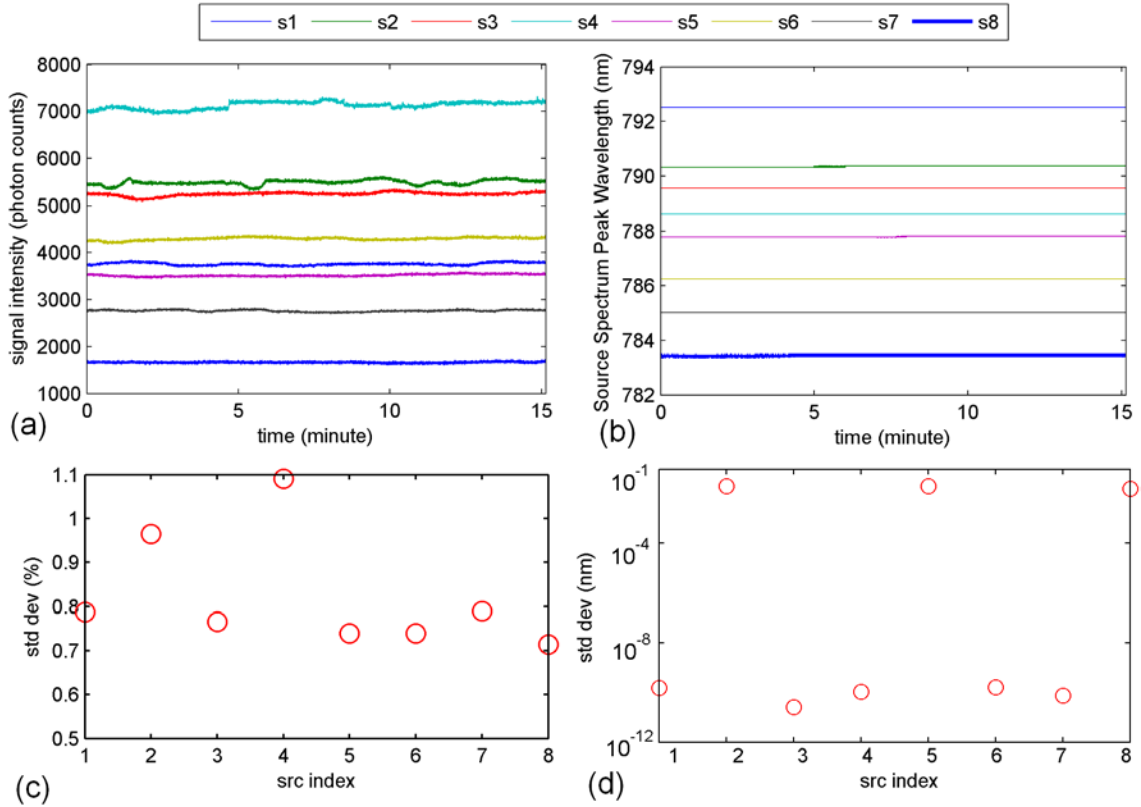


Figure 2.3. Stability test of 8 LD sources in the 785 nm wavelength band. (a) The intensity stability of the LDs. (b) The wavelength stability of the LDs. (c) The standard deviation of intensity divided by the average intensity of the LDs. (d) The standard deviation of wavelength of the LDs.

### 2.1.2 Optical Detectors

The optical detection system shown in Figure 2.4 consisted of 8 Princeton/Acton Insight: 400F Integrated Spectroscopy Systems (Acton, MA) residing in one custom designed wheeled carts (8020, Columbia City, IN) [75]. The Insight 400F consists of a 0.3 m long, F3.9 imaging spectrograph and a low noise, front illuminated CCD cooled to

-70 °C. The 16-bit CCD was vertically binned to maximize detector area/wavelength, which provides a large dynamic range of 0 to 65535 photon counts in each of the 1340 wavelength bins, where the background noise is usually around 500 photon counts. The 1200 grooves/mm grating in front of each CCD provides a spectral coverage of 60 nm which is wide enough to allow simultaneous imaging of all sources in the 785 wavelength band. Its spectral resolution of  $60/1340 = 0.045$  nm is much smaller than the 1.5 nm average laser bandwidth interval, as well as the light spectrum of each laser source. The signal intensity of one LD detected on the CCD is then the integrated photon count of the LD spectrum.



Figure 2.4. The detection system consisting of 8 spectrometers and 8 CCDs [75] is shown.

The linearity and the noise feature of the CCDs were carefully characterized. One LD source was attached to a slab-shaped homogeneous phantom through a fiber, and the detection fibers connecting the CCDs were attached to the same location on the other side

of the phantom sequentially. For each exposure time setting on each CCD, 100 measurements were taken continuously. The exposure time of each CCD was changed within a wide range while the output power of the LD was kept constant. This setting is equivalent to the combination of a precise power-tunable LD and a CCD with constant exposure time setting. The background dark noise of the CCDs was around 600 photon counts, and the maximum intensity perceivable by the CCDs was 65536 photon counts. So the exposure time was chosen to increase from 30 ms to around 5 s which typically led to 1000 to 61000 photon counts on the CCDs. Three parameters of the CCDs were analyzed and the results were plotted in Figure 2.5. The linearity of the CCDs is characterized by the mean signal intensity of the 100 measurements on the CCD versus the exposure time, as shown in the first column of Figure 2.5. The absolute value of noise is characterized by the standard deviation of the 100 measurements versus mean signal intensity, as shown in the second column of Figure 2.5. The noise level in percentage is defined as the ratio of the standard deviation of the 100 measurements divided by the mean value of the 100 measurements, as shown in the third column of Figure 2.5. It has to be noted that only 7 CCDs were characterized here. The reason is that this characterization experiment was carried out after one CCD was removed in building the two-wavelength high-speed system, as stated in Chapter 3.

From the first column of Figure 2.5, it is obvious that all 7 CCDs have very good linear response to the averaged input intensity in the entire detection range. The noise level of all CCDs increases as the intensity of input signal increases, but not in a linear fashion, as shown in the second column of Figure 2.5, which means this noise doesn't only come from the fluctuation of LD power as shown in Figure 2.3, but also from the

CCDs. The linearity of the noise level is much better in the middle range, so extra noise is introduced by the CCDs when the signal intensity is close to the lower and upper limits. The third column of **Error! Reference source not found.** shows that the ratio of noise divided by the signal intensity is around 1% for signal intensities larger than 104 photon counts on CCDs, which agrees with the nearly 1% noise level noticed in the LD power stability experiment in Figure 2.3(c). This ratio increases drastically to around 5% for signal intensities close to the dark noise background, so exposure time should always be chosen to ensure larger intensities on all CCDs in order to minimize this random noise.

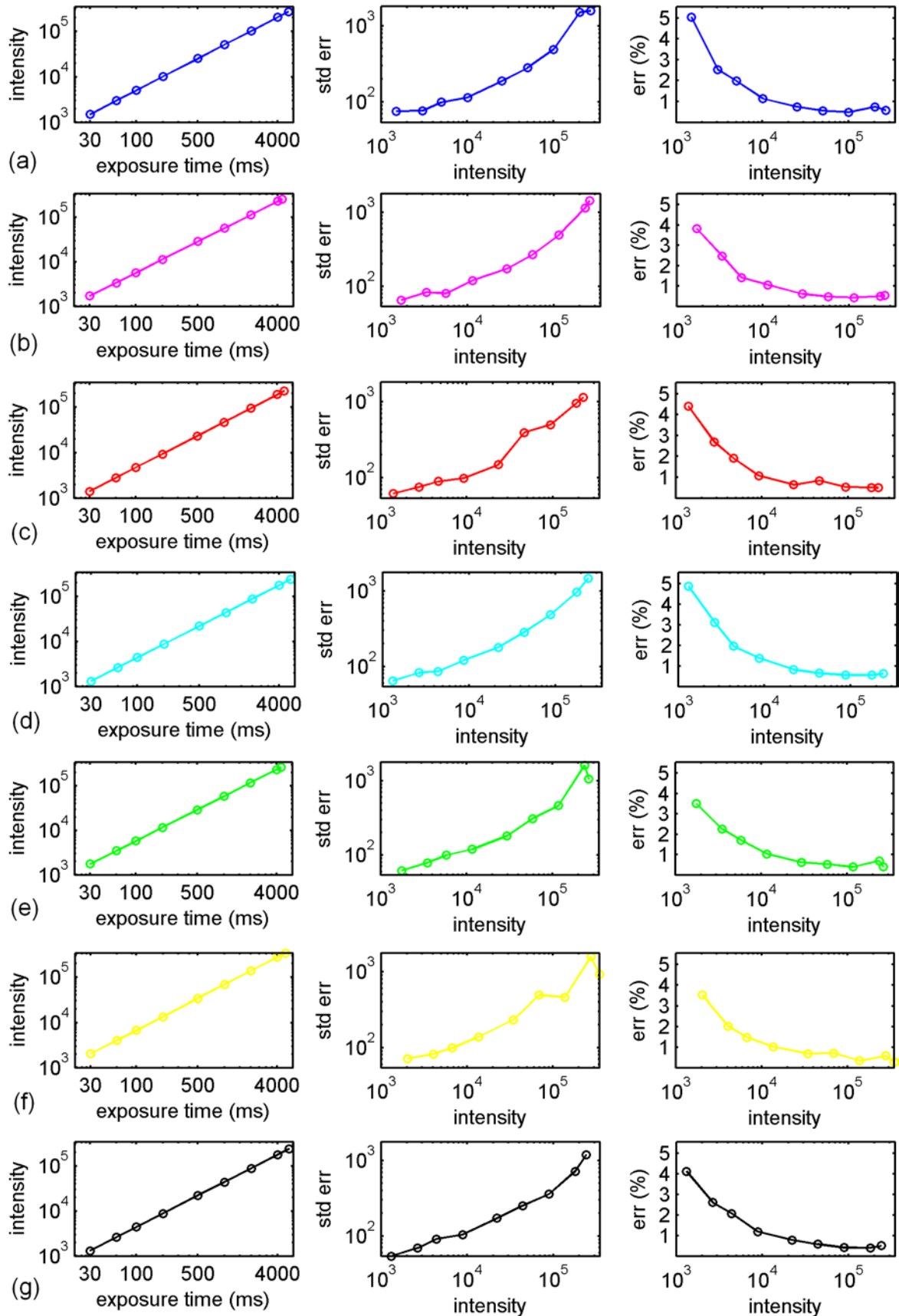


Figure 2.5. Linearity and noise analysis of 7 CCDs, with each row (a) to (g) showing data from one of the CCDs. The first column is the linearity. The second column is the noise level relative to signal intensity. The third column is the noise level in percent.

### **2.1.3 Tissue/Phantom Interface**

Previous attempts at a high-speed NIR tomography system with spectral-encoded sources used the conventional circular coil design with source fibers and detector fibers placed alternatively around the coil [68]. The circular geometry has been the most popular choice since it benefits from a full 2D measurement view over the entire tissue volume which is similar to the CT. But full exploitation of this geometry requires large dynamic range proportional to the size of the object to be imaged. This system works well for fast imaging on small objects where the optical dynamic range is not larger than 3 OD between different source-detector light paths. But for thick tissue imaging, e.g. clinical breast cancer imaging in vivo with diameters of up to 10 cm and magnitude dynamic range up to 8 OD which is common for diffuse optical tomography in scattering dominated breast tissue, it is technically impossible to manufacture reliable optical detectors with such a huge magnitude dynamic range. The result is that for a 16 bit CCD, a signal that is even 4 orders of magnitude smaller than another could not be detected with useful SNR level. Figure 2.6(c) shows the raw data from a measurement on a homogeneous circular phantom with a diameter of 73 mm. The sources and detectors were arranged alternatively as shown in the left part of Figure 2.6(a). The two strongest peaks were signals from the closest sources. Signals from the two second closest sources

could barely be seen, and signals from farther sources were totally merged into the background noise.

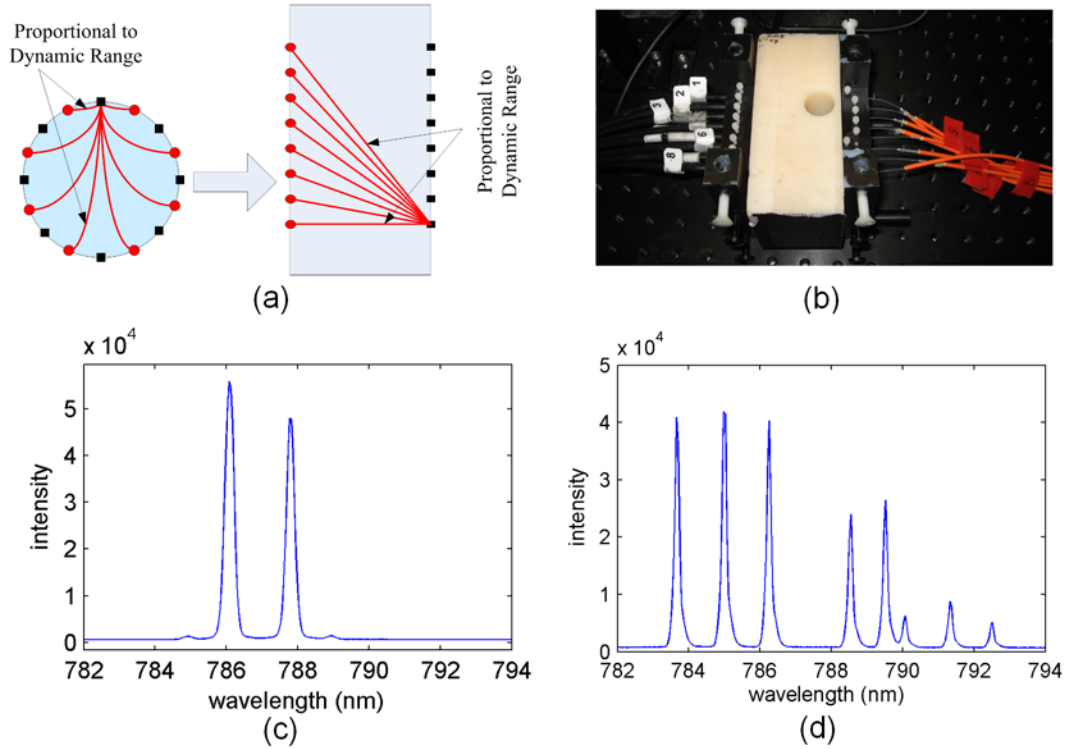


Figure 2.6. (a) The average light paths for the circular geometry and the slab geometry are illustrated. (b) Experimental photograph of a 64.5 mm thick slab phantom is shown with 8 orange source fibers on the right side and 8 black detection fibers on the left. (c) The signals from 8 LDs measured by one CCD with a circular homogeneous phantom. (d) The signals from 8 LDs measured by one CCD with a slab homogeneous phantom. Note in (c) that most of the laser signals are not really detectable.

Meanwhile it is clear that the difference of optical path lengths in the slab geometry is much smaller, as shown in Figure 2.6(b). Thus the slab geometry substantially lowers the requirement of dynamic range to 2 to 3 OD, and fits well for high speed thick tissue

imaging. Figure 2.6(d) shows the raw data from a measurement on a 64 mm thick homogeneous slab phantom. It is clear that signals from all laser sources were distinguishable on the same CCD. Although the view of the slab geometry is limited, it does have an advantage that the compressed tissue provides increased light transmission and resolution, since resolution performance falls off with increasing distance from the source. A flexible fiber holder consisting of two parallel panels with two sliding bars across the bottom was built to hold the source and detector fibers against the tissue/phantom, as shown on Figure 2.6(b). On each panel, 8 holes were drilled with 8 mm intervals across to hold source or detector fibers, and set screws from the top fix the fibers in position. This configuration is flexible for different phantom thicknesses and stable enough for phantom experiments, as well as for future use in tissue imaging.

#### **2.1.4 Exposure Synchronization**

The goal of this work was to image with fast and continuous CCD exposures. The Pixis 400F spectrometer provides a good signal to noise ratio, but uses a slow mechanical shutter in front of the CCD to control the entrance of the input light, so its shutter was set to remain open during fast acquisitions in these experiments. Moreover, all 8 CCDs were synchronized to start and stop exposing at exactly the same time to get meaningful timeline dataset. To achieve this, an periodical external TTL trigger signal was generated by a NI DAQ board (Figure 2.7 (b)), and split into 8 channels by a customized splitter circuit (Figure 2.7(a)), and finally reaches the external sync port on each CCD to accurately synchronize all CCDs. The shape and period of the TTL trigger signal can be easily specified through LabVIEW. The Scientific Imaging Tool Kit for LabVIEW (R Cubed Software, NJ) which is a commercial LABVIEW package to control these

spectrometers doesn't provide a standard mode to continuously expose all CCDs at a synchronized pace. To solve this problem, a "non-standard" high speed acquisition mode was discovered, and all 8 spectrometers were configured to work in this mode. The shutter status on the CCDs was set to open before starting an acquisition sequence. The exposure mode was set to Strobed Mode, meaning each exposure requires an external trigger signal to start. All CCDs were set to Synchronous Focus Mode. This mode alone would make the CCDs continuously acquire at a preset rate and only transfer the latest frame when the console computer was ready to receive, so no synchronization could be realized on the multiple CCDs with this mode alone. But it was discovered that together with the Strobed Mode exposure setting, the CCDs actually will keep exposing until the next trigger signal arrives, and then they transfer the data and clean the built up charges and start a new exposure, which perfectly fits the design requirement. Through repeated measurements, it has been proven that the whole transfer-clean-prepare process for all 8 CCDs takes about 13 milliseconds to complete. Since the shutter remains open, the actual exposure time is the interval between trigger signals, which should not be shorter than the nominal preset CCD exposure time plus 13 milliseconds. With a 100  $\mu\text{m}$  slit-width setting on all spectrometers and 10 mW input laser beams at the tissue entrance, 20 datasets per second can be reached easily on a 64 mm thick resin phantom with satisfactory signal intensity.

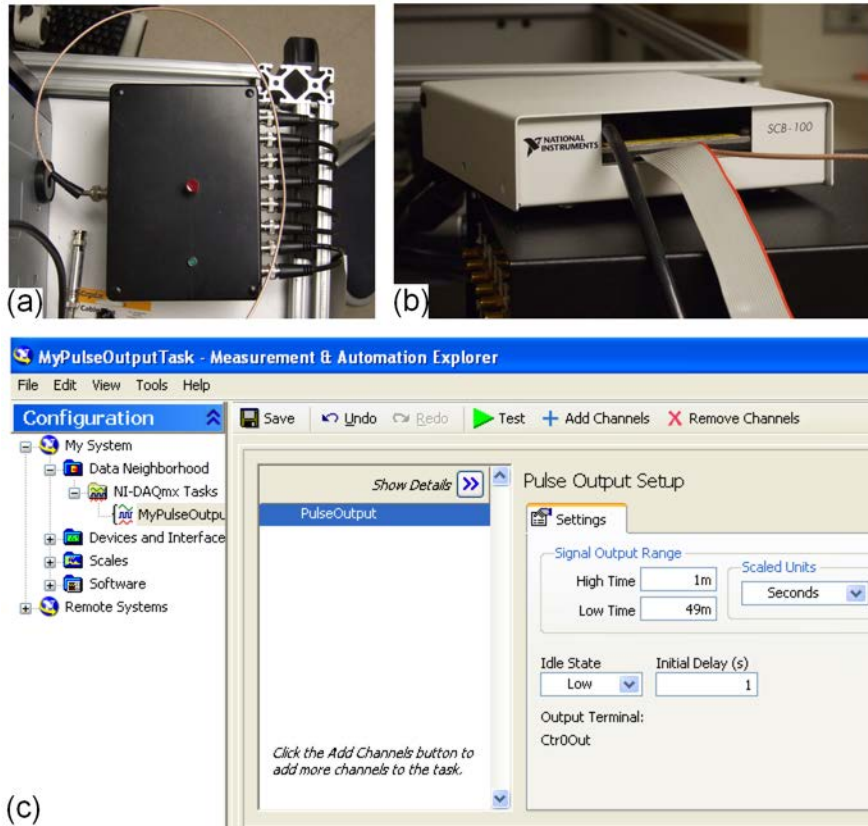


Figure 2.7. (a) The splitter circuit box to convey the trigger signal to the EXT SYNC ports of 8 CCDs. (b) The NI DAQ board to generate trigger signal. (c) The LABVIEW program interface to control the frequency and shape of the trigger signal.

## 2.2 Experimental procedure and raw data process

To perform high speed imaging on an object with this system, three measurements have to be done in addition to the imaging of the object:

- A measurement on a homogeneous phantom for calibration purpose
- Power calibration for all input source channels
- Efficiency calibration for all detection channels

A measurement on a calibration phantom which has similar shape and optical properties is needed for all model-based DOT reconstruction algorithms, including NIRFAST. Calibrations of source channels and detection channels are required specifically for this system to process the raw data prior to reconstruction, and the reasons and procedures are explained below.

### **2.2.1 Calibration of input power of source channels**

The power coming out of a source fiber, usually tuned to between 10 and 15 mW, is determined by the attached laser diode and its temperature and driving current, the focusing optics, and the attenuation inside the source fiber. All these factors are constant during imaging, thus the power out of the fibers should be constant. This power is attenuated before propagating into the object due to the coupling loss at the fiber-object interface, and the coupling loss is variable between experiments. In addition, the output power of a LD can change slightly between experiments. Therefore the power going into the object, called  $P_{obj}$ , has to be calibrated in every experiment. Fortunately, only the ratio of  $P_{obj}$  of all sources is needed for reconstruction program. This ratio, called  $R_{src}$ , is obtained by the procedure shown in Figure 2.8(a). This calibration also removes the errors caused by the possible spatial inhomogeneity of the calibration phantom.

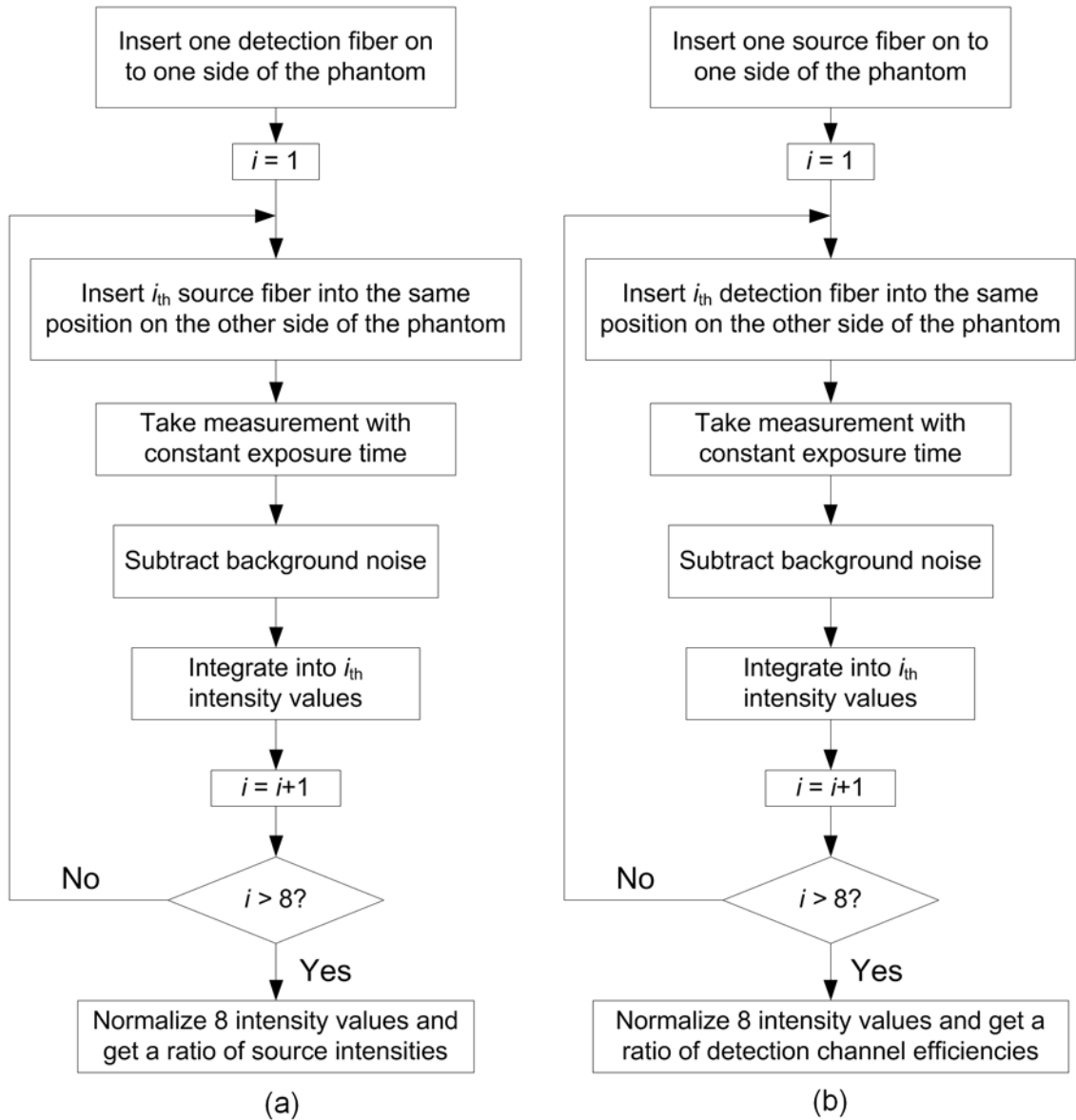


Figure 2.8. (a) The procedure to calibrate source intensities. (b) The procedure to calibrate detection efficiencies of all detection channels.

## 2.2.2 Calibration of detection efficiencies of detection channels

After the light reaches the boundary on the detection side of the object, it is attenuated again by the coupling loss on the object-fiber interface, and then gathered by the detection fiber and attenuated along the way, and partly blocked by the entrance slit in

front of the spectrometer, finally the detection efficiency of the spectrometer will come into play. The entrance slits are manually adjustable and are used to control the signal intensity on CCDs according to the absorbance of the object to be imaged, because the frame rate is predefined, and adjusting the output power of LDs too much may affect the stability of lasing power and wavelengths. Since the coupling loss and widths of entrance slits may change in each experiment, the overall detection efficiency along each detection channel needs calibration in every experiment. Similar to  $R_{src}$ , only the ratio of all detection efficiencies is needed for reconstruction program. This ratio, called  $R_{det}$ , is obtained by the procedure shown in Figure 2.8(b).

### 2.2.3 Raw data process

There are totally 64 spectra in the dataset for one frame, and each spectrum represents the detected signal of one source-detector pair. However, the meaningful data to be used in reconstruction is the attenuation of each source-detector pair. The key to calculate this attenuation is to obtain the intensity of light going into the object, and the intensity of light going out of the object.  $R_{src}$  from section 2.2.1 and  $R_{det}$  from section 2.2.2 are used to achieve this goal. The procedure is shown in Figure 2.9. This calibration procedure has to be performed on both the measurement of a calibration phantom and the measurement of the object. The resulting two datasets of attenuation are put into the calibration program in the NIRFAST software package. The working principle of the calibration program has been fully explained elsewhere [76], but briefly the purpose is to subtract offset errors in the logarithm of the intensity, and put the measured data on the same intensity basis as the simulated light transmission such that the iterative reconstruction routine can fit the data with high accuracy. The data obtained from the

calibration program is then put into the reconstruction program to finally recover the spatial optical properties of the object. The reconstruction program initially assumes a homogeneous volume, as it is based upon a perturbation approach to reconstruction, and a Newton-type algorithm iteratively fits the calibrated data for heterogeneities in the tissue optical properties.

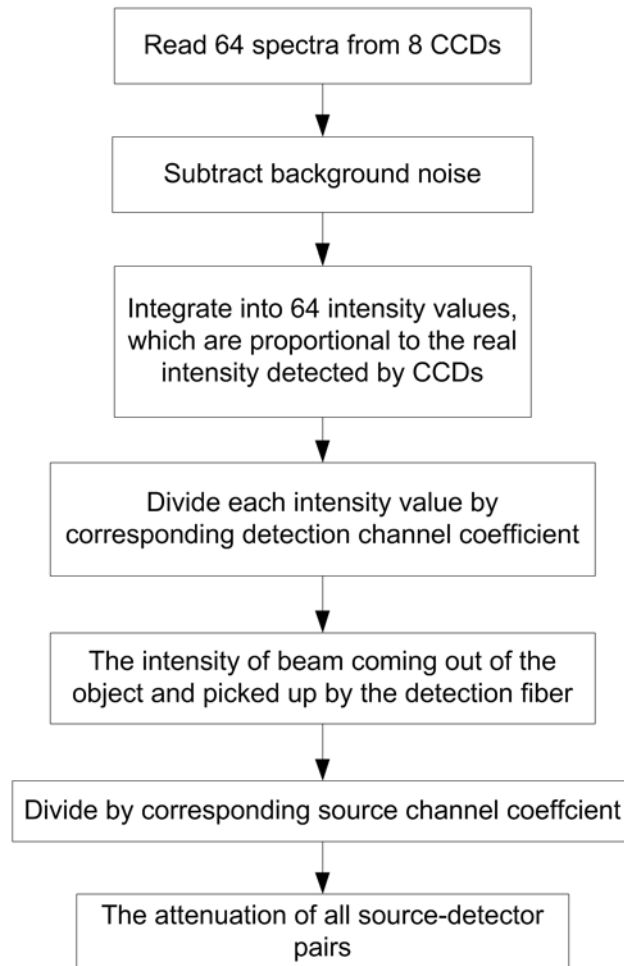


Figure 2.9. The procedure to calculate attenuation from each source-detector pair for one measurement is shown.

### 2.3 Static Blood Phantom Imaging Experiment

A set of heterogeneous phantom experiments was carried out to evaluate the linearity and accuracy of the system. The slab-shaped resin phantom used for this experiment is 134 mm long and 64.5 mm thick. The background optical properties of the phantom at 785 nm,  $\mu_a = 0.004 \text{ mm}^{-1}$  and  $\mu_s' = 1.4 \text{ mm}^{-1}$ , were measured separately using a well characterized frequency domain clinical diffuse optical tomography system [77]. A cylindrical hole with a radius of 10 mm was drilled vertically at about 16 mm away from the center of the phantom. A batch of liquid phantoms with linearly increasing volume fractions of swine whole blood from 0.0% to 4.0% with an interval of 0.5%, were made in 1.0% stock intralipid solution. The CCDs were set to operate at 20 frames per second. Approximately 10 mW of optical power was delivered into the phantom by each of the 8 source fibers. The hole was filled up with one phantom solution at a time and NIR tomographic images were acquired for about 1 second.

As this was a static imaging experiment, a reconstructed image of one representative frame for each phantom solution was displayed. The calibration and reconstruction algorithm used was similar to that described by [78]. Briefly, the reconstruction is based on a modified Newton's method to minimize the difference between measured and model data. The model used here is a finite element discretization of the diffusion equation. The measurement of the phantom was first calibrated to account for offsets due to source-detector fiber transmission, alignment characteristics, and errors in discretization and model-data mismatch. This was accomplished using a homogeneous fitting algorithm [78], which utilized Newton-Raphson method to fit two parameters: the slope of the phase  $\text{lag}(\theta)$  with respect to distance from the source

location, and the slope of the logarithm of intensity times distance ( $\log(rI)$ ) with regard to distance. Since this video-rate tomography system uses CW LDs and hence has no ability to measure the path length of transmission, the spatial distribution of the reduced scattering coefficient  $\mu_s'$  was not attempted to be recovered. Thus an assumption about the spatial distribution of  $\mu_s'$  was needed to reconstruct the spatial distribution of the absorption coefficient  $\mu_a$ . As the scatters were 1.0% intralipid in all phantoms, a homogeneous distribution of  $\mu_s' = 1.0 \text{ mm}^{-1}$  was used as the reduced scattering coefficient in the anomaly. This value was calculated based on a previous study by Staveren et al [79].

### 2.3.1 Direct Reconstruction of $\mu_a$

Direct reconstruction here means to reconstruct for real value of  $\mu_a$  which reflects the actual local absorption property across the 2D imaging plane. The dataset used for reconstruction is obtained from heterogeneous phantom measurement and calibrated with another dataset obtained from homogeneous phantom measurement. The calibration equation is:

$$\Phi_{calibrated}(hetero) = \Phi_{measured}(hetero) - (\Phi_{measured}(homo) - \Phi_{calculated}(homo)) - \Phi_{offset}(net) \quad (2.1)$$

where  $\Phi$  is the data set consisting of logarithm of the amplitude, and the calibrated data set is used for reconstruction. Details about this calibration method can be found in [78].

For each swine blood concentration, about 20 frames of raw data were acquired continuously. After putting all these datasets into the reconstruction program, it was found that the standard deviation of the recovered  $\mu_a$  within the anomaly was less than

1% of the mean value of  $\mu_a$ , so the system and the algorithm were stable and only the result of one frame was listed here for each swine blood concentration. The reconstructed images of  $\mu_a$  on the imaging plane with linearly increasing concentration of swine blood in the anomaly were listed in Figure 2.10(a) to (d). The reconstructed position of the anomaly met with its true position in the phantom. The reconstructed shape of the anomaly appeared to be stretched in the vertical direction and compressed in the horizontal direction. This is believed to be caused by the parallel source-detector arrangement of the slab geometry, which enhances imaging and reconstruction sensitivity in the vertical direction comparing to the horizontal direction. The true value of  $\mu_a$  in each solution was calculated from the hemoglobin concentration measured with a commercial oximeter (Hb 201+, HemoCue AB, Sweden) prior to imaging. The average reconstructed  $\mu_a$  within the inclusion was calculated for each case and a reasonably linear response was observed, as shown in Figure 2.10(f). The absolute value of recovered  $\mu_a$  in the anomaly was found to be slightly larger than the true value, especially when the  $\mu_a$  of the anomaly was close to the background. This could partly be due to the reflection index mismatch on the boundary of the anomaly. Fortunately the  $\mu_a$  of the tumor region is usually much larger than that of the background, so it is not a big problem for clinical use. The artifacts close to the top boundary on these images were mainly caused by the coupling error of source and detector fibers, which can be repeated in simulation. The recovered mean background  $\mu_a$  outside the anomaly remained constant for all phantoms as expected.

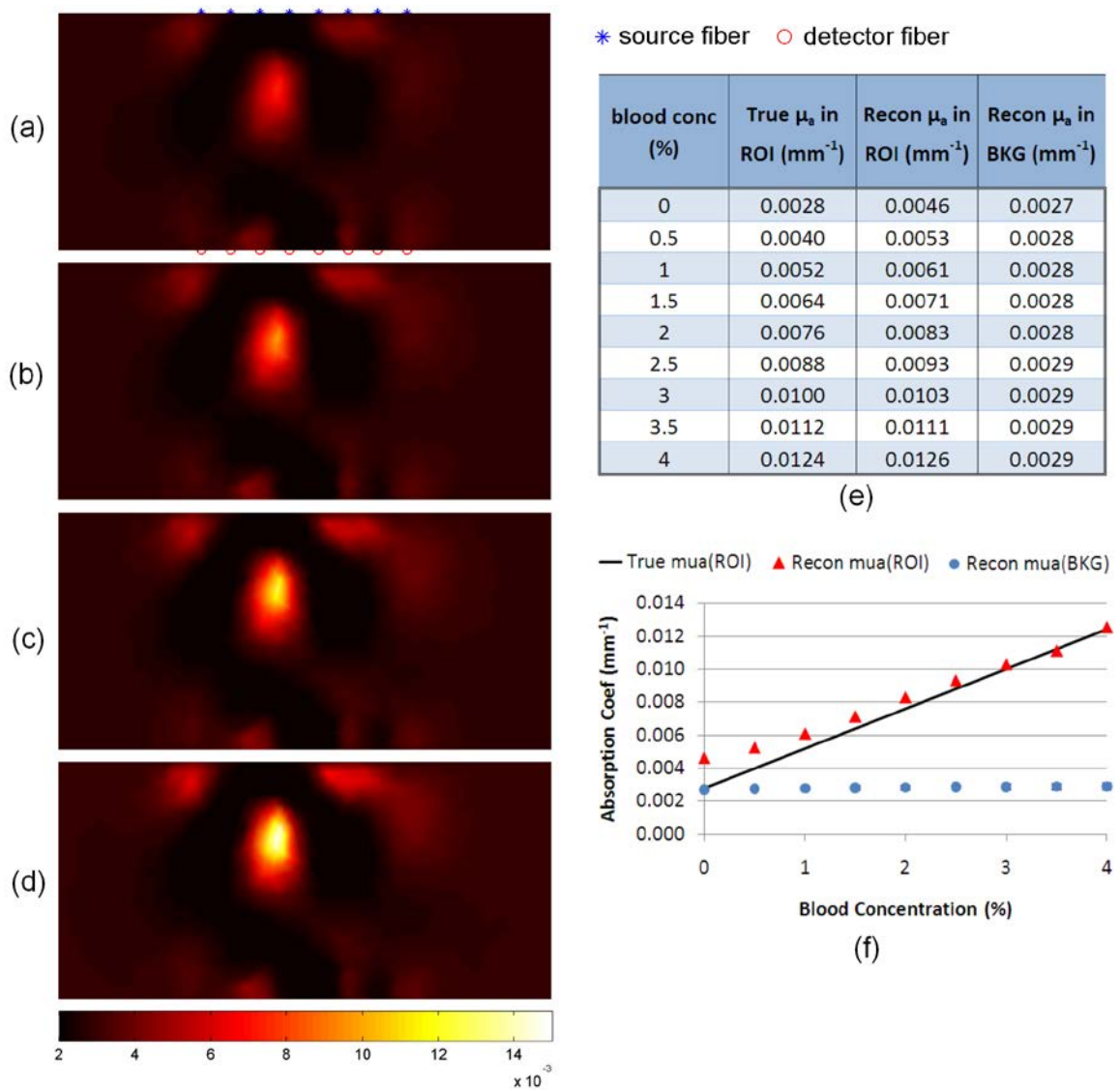


Figure 2.10. Direct reconstruction results of  $\mu_a$  on the imaging plane of a heterogeneous phantom with different blood concentrations in the anomaly. (a)-(d) show reconstructed images of the phantom with swine blood concentration of 1%, 2%, 3% and 4%. The reconstructed and true values of  $\mu_a$  in the anomaly (marked as ROI) and in the background (marked as BKG) of different swine blood concentrations are listed in (e), and plotted in (f).

### 2.3.2 Difference Reconstruction of $\mu_a$

Difference reconstruction method means to reconstruct only for the change of  $\mu_a$  in the imaging plane with datasets of two frames. The equation is:

$$\begin{aligned} \Phi_{difference}^i(hetero) &= \Phi_{homo\_fit}^i(hetero) + \Phi_{measured}^i(hetero) \\ &\quad - \Phi_{measured}^j(hetero) \end{aligned} \quad (2.2)$$

where  $\Phi_{measured}^j(hetero)$  is the logarithmic raw dataset of the chosen frame as the reference, which usually is the first frame.  $\Phi_{measured}^i(hetero)$  is the logarithmic raw dataset of the  $i_{th}$  frame. So  $(\Phi_{measured}^i(hetero) - \Phi_{measured}^j(hetero))$  contains the information corresponding to the change of  $\mu_a$  in the imaging plane.  $\Phi_{homo\_fit}^i(hetero)$  is the homogenous fitting of the actual heterogeneous phantom, and it is used to provide a homogeneous “baseline” for  $\mu_a$  reconstruction. So the dataset  $\Phi_{difference}^i(hetero)$  should generate an image that only displays the difference of  $\mu_a$  of two frames on top of the “baseline” homogeneous background. This information of  $\mu_a$  variation could be more meaningful clinically, especially in hemodynamics monitoring. Another big advantage of this method is that the noise introduced in the experiment could be largely canceled out, leaving an image with much less artifact.

Diffuse tomography reconstruction was performed after pre-processing the experimental data according to Equation 2.2. The time needed to reconstruct one frame depends mainly on the size of the mesh. For the mesh used here which contains 1405 nodes, it takes around 10 seconds to reconstruct one frame on a standard laptop. 200 frames totally took about 33 minutes to process.

The difference reconstruction results of  $\mu_a$  with different swine blood concentrations in the anomaly are listed in Figure 2.11(a)-(d). For the same reason as in the direct reconstruction case, only the reconstructed image of one frame out of about 20 frames was listed in Figure 2.11 for each swine blood concentration. The artifacts around boundaries were largely removed as expected. However, the position of the reconstructed anomaly shifted a little towards the upper boundary of the phantom. It was verified through simulation that this position shift towards the boundary didn't exist with noise-free data, but it became more and more apparent with increasing noise level because closer to the boundary means higher imaging and reconstruction sensitivity. Although the noise was largely canceled with this difference reconstruction method, it is difficult to estimate the effect of the remaining noise on the reconstructed images. The reconstructed mean value of  $\mu_a$  in the anomaly met with the true value reasonably well, and the reconstructed  $\mu_a$  value of the background kept constant as expected, as shown in Figure 2.11.

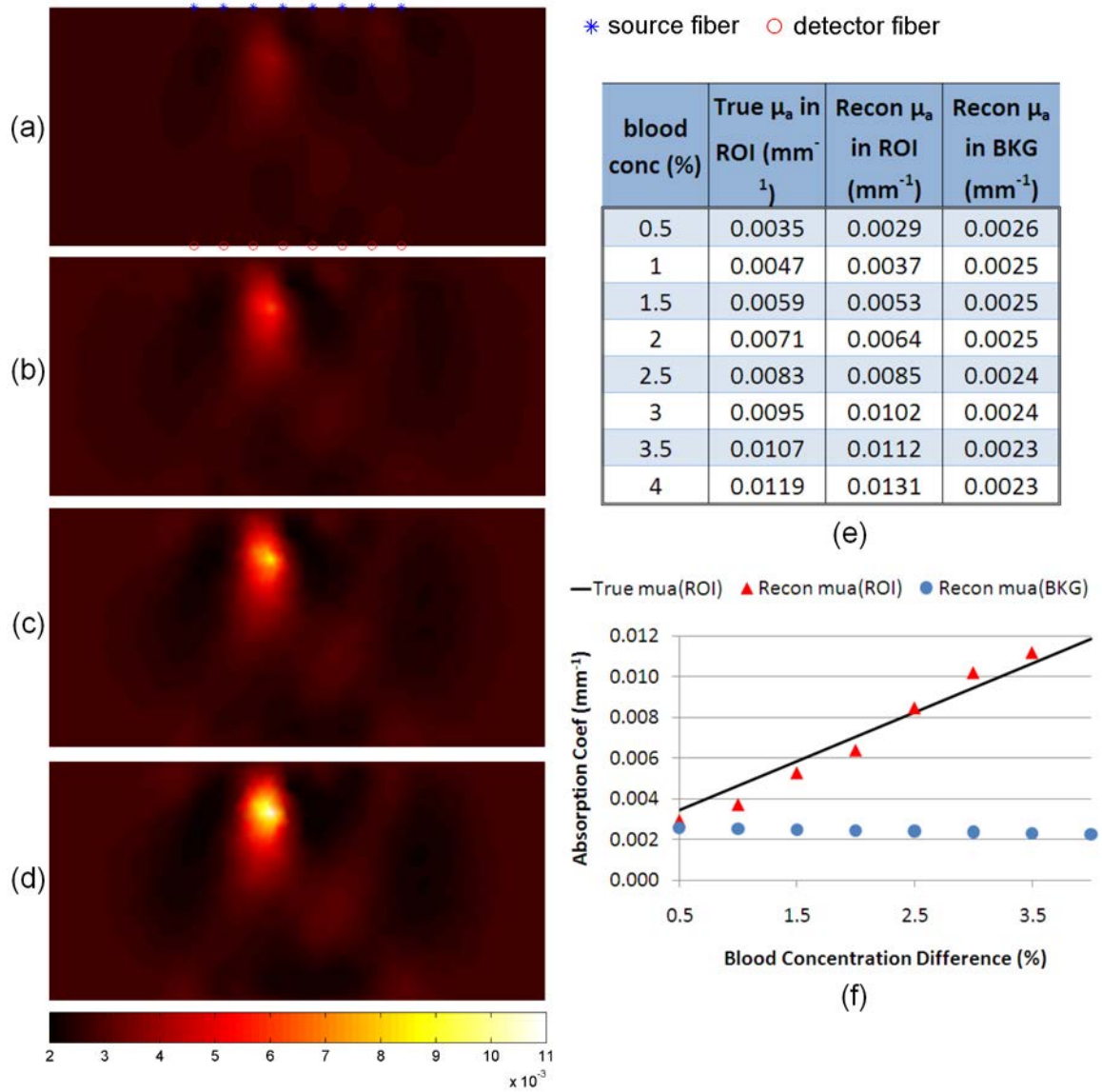


Figure 2.11. Difference reconstruction results of  $\mu_a$  on the imaging plane of a heterogeneous phantom with different blood concentrations in the anomaly. (a)-(d) show reconstructed images of the phantom with swine blood concentration of 1%, 2%, 3% and 4%. The reconstructed and true values of difference  $\mu_a$  in the anomaly (marked as ROI) and in the background (marked as BKG) of different swine blood concentrations are listed in (e), and plotted in (f).

### 2.3.3 Region-based Reconstruction of $\mu_a$

A region-based direct reconstruction method was also applied to this dataset. According to this method, the imaging plane can be segmented into several homogeneous regions based on the structural information obtained in advance from other imaging modalities, e.g. MRI and x-ray CT. The iterative update is then simplified from the situation where nodes are reconstructed individually, to the problem where only the parameters for each homogenous region are estimated in the inversion [80].

In this case, the mesh was segmented into two regions, the anomaly region (marked as ROI) and the background region (marked as BKG), as shown in Figure 2.12(a). So instead of inverting a matrix that is thousands of rows, it has just 2 rows, one for each region. The advantage of this method is that the contrast is enhanced between the anomaly and the background, and artifact and noise are greatly removed because of the strong averaging effect of this algorithm. The figure and table in Figure 2.12(b) and (c) showed a very good linear relationship between blood concentration and the reconstructed  $\mu_a$  in the anomaly. And no obvious offset was noticed with small blood concentration. These features make this method advantageous comparing to the FEM based algorithm in section 2.3.1 and 2.3.2. Although the slope of the reconstructed  $\mu_a$  curve is not as steep as the true  $\mu_a$  curve, the difference is not large at all.

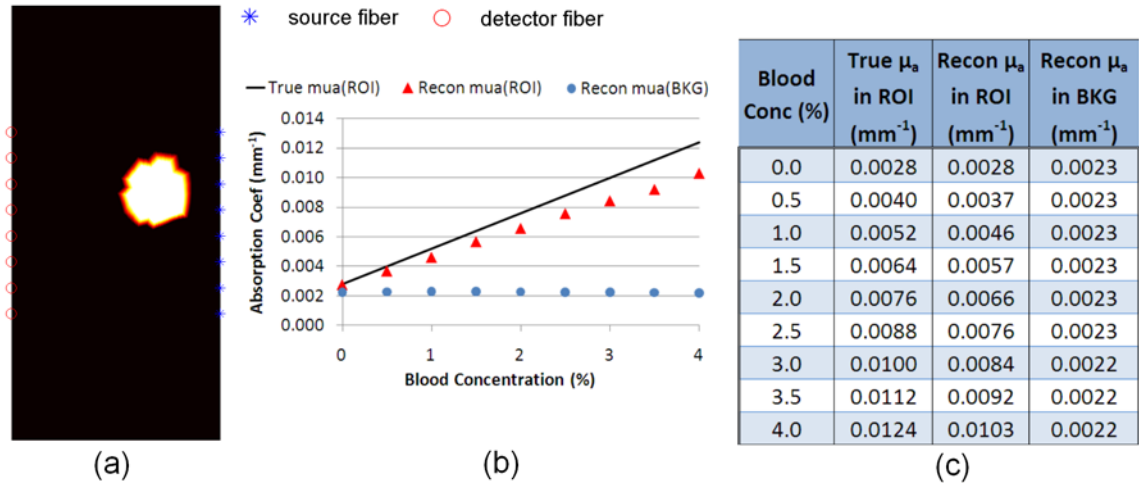


Figure 2.12. (a) The segmented mesh for region-based reconstruction. (b) A plot of the reconstructed and true values of  $\mu_a$  in the anomaly (marked as ROI), and the reconstructed  $\mu_a$  of the background (marked as BKG) of different swine blood concentrations. (c) A list of all reconstruction results in (b).

## 2.4 Dynamic Blood Phantom Imaging Experiment

To verify the responsivity of the system to dynamic changes in absorption contrast, two experiments were designed. The first experiment was to monitor the variation of absorbance inside a static anomaly in a blood phantom. The second experiment was to monitor the position of a moving anomaly in a blood phantom.

### 2.4.1 Static anomaly with varying absorption property

The phantom and system setup were the same as the static phantom experiment described in section 2.3. Initially, the anomaly was filled with 1% intralipid solution. After imaging the phantom at 20 frames per second for about 30 seconds, swine whole blood was added into the anomaly slowly by manually pushing the blood out of a syringe.

The adding process took about 50 seconds, and the phantom was continuously imaged for about 40 seconds after finishing adding blood.

Result of direct reconstruction was shown in Figure 2.13. The time of the first rising point and the time  $\mu_a$  reached the maximum value fitted well with the experiment procedure. The reconstructed  $\mu_a$  value in Figure 2.13(a) couldn't be verified by the averaged concentration of the swine blood, because the solution in the anomaly was not stirred during the whole imaging process to avoid the impact of the stirring tool. Therefore the blood was not evenly distributed in the anomaly, and it was meaningless to calculate the true  $\mu_a$  value based on the volume of swine blood added into the inclusion. Some boundary artifact was noticeable in Figure 2.13(b). But generally the position of the anomaly and the trend of  $\mu_a$  met with the actual situation.

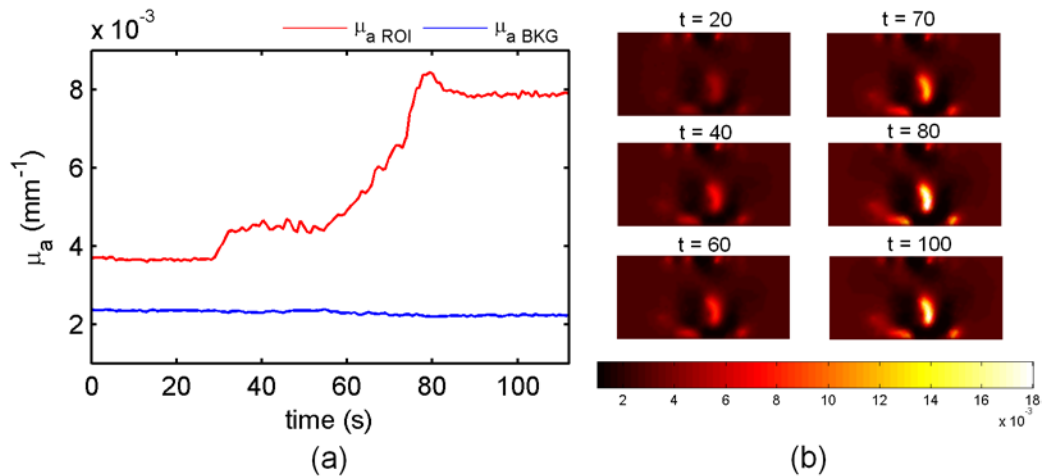


Figure 2.13. (a) The reconstructed  $\mu_a$  of the anomaly (marked as ROI) and the background (marked as KG), using the direct reconstruction method. (b) Reconstructed images at several time points (in seconds).

Result of difference reconstruction was shown in Figure 2.14. The dataset of the first frame was used in the difference reconstruction as the “baseline” to be subtracted by

the datasets of following frames. In the first 30 seconds there is no change of the absorber in the anomaly because no blood was added, so after subtraction only the homogenous fitting part was left in the dataset and the reconstructed images should appear homogeneous, which agreed well with the first 30 seconds of the  $\mu_a$  curves in Figure 2.14(a). As more blood was added into the anomaly,  $\mu_a$  in the anomaly gradually increased to a peak at around 80 seconds and then reached a stable status, as curve  $\mu_{aROI}$  shown in Figure 2.14(b). The recovered images have much less boundary artifact, and the position of the anomaly was shifted a little towards the boundary, which agreed with the findings about the features of difference reconstruction method in section 2.3.2.

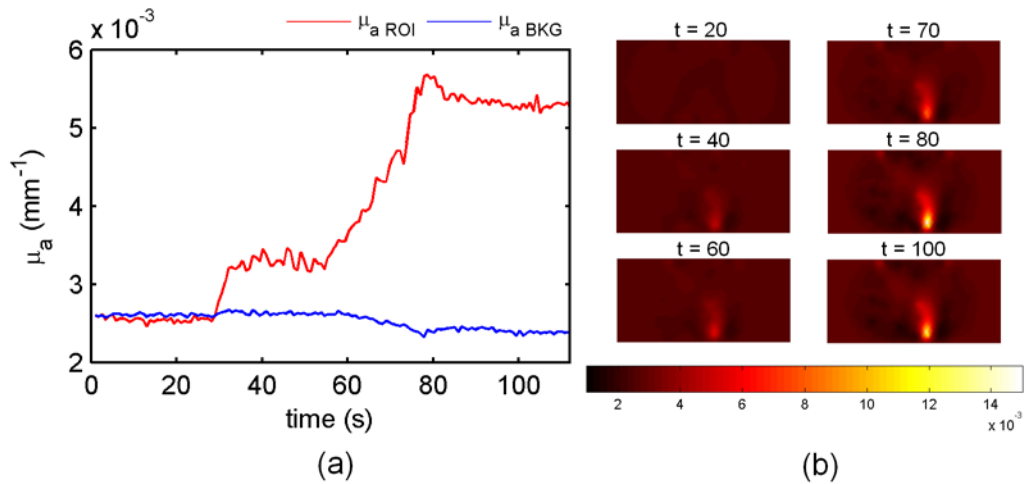


Figure 2.14. (a) The reconstructed  $\mu_a$  of the anomaly (marked as ROI) and the background (marked as BKG), using the difference reconstruction method. (b) Reconstructed images at several time points.

Result of region-based reconstruction was shown in Figure 2.15. The curve  $\mu_{aROI}$  is identical to the curve of the direct reconstruction method in Figure 2.13(a) with two exceptions. The first is that the  $\mu_a$  value of this method is slightly smaller than that of

the direct reconstruction method. The second is that the first 30 seconds of the curve  $\mu_{a\ ROI}$  of the region-based reconstruction method is smaller than that of the direct reconstruction method. These two exceptions agreed very well with the comparison in section 2.3, where it has been found that the region-based reconstruction method has better linearity than the direct reconstruction method when the contrast between the anomaly and the background is small, and the  $\mu_a$  value recovered by the region-based method is usually slightly smaller than that recovered by the direct reconstruction method.

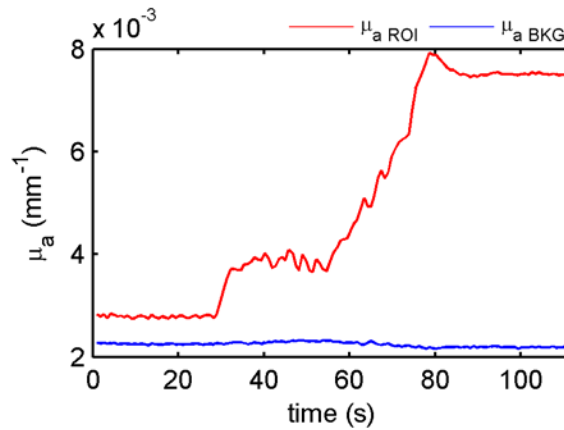


Figure 2.15. The reconstructed  $\mu_a$  of the anomaly (marked as ROI) and the background (marked as BKG), using the region-based reconstruction method.

Overall, the results listed in Figure 2.13 to **Error! Reference source not found.** demonstrated the reliable functioning of this video-rate tomography system to catch dynamic varying absorption property at imaging speed of 20 frames per second through a thick tissue-like phantom. And all three reconstruction methods can recover the temporal variation of  $\mu_a$  in the anomaly.

### 2.4.2 Moving anomaly with constant absorption property

This experiment was designed to test the system's ability to catch the position of a moving anomaly inside a slab-shaped liquid phantom. Because the view of the slab-shaped interface design is limited comparing to the conventional circular design, it is important to test the effective view range of the system.

The experimental setup is shown in Figure 2.16. A 72 mm thick slab-shaped high-density polypropylene bottle (32 oz HDPE Rectangular Bottle, Nalgene) was filled with 1% intralipid solution. Swine blood was added in and mixed well. Source fibers and detection fibers were placed on two sides of the liquid phantom. 7 sources and 7 detectors were used in this experiment. A half-transparent white plastic tube of 20 mm in diameter containing the mixture of swine whole blood and 1% intralipid was immersed into the solution vertically. The tube moved slowly from side to side while the CCDs on the detection cart were synchronized to image continuously at 10 Hz.

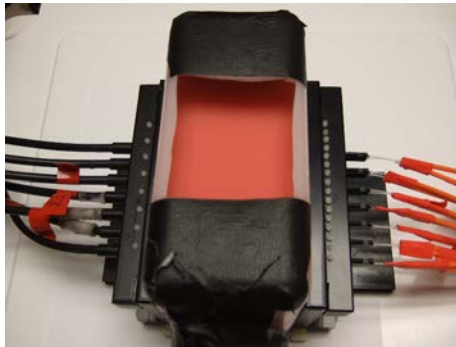


Figure 2.16. The setup of the moving anomaly experiment with the slab tank which contained solution made of intralipid and blood. Here the black fibers were for detection, and the orange fibers were source delivery from laser diodes.

After careful calibration, both direct and difference reconstruction methods were applied to the dataset. Region-based algorithm was not used in this case because prior information about the position of the tube was unavailable in this experiment.

The results of the direct and difference reconstruction algorithm are shown in Figure 2.17 and **Error! Reference source not found.** separately. In this experiment, the coupling error didn't appear to be large, and no severe boundary artifact was noticed in both methods. Thus there is no obvious difference in the image quality of these two methods. The view limitation of the slab geometry is obvious in both cases, and the tube couldn't be well characterized when it moved close to the uppermost or lowest source-detector pairs. The location and the shape of the tube were better characterized when it was closer to the center of the source-detector arrays.

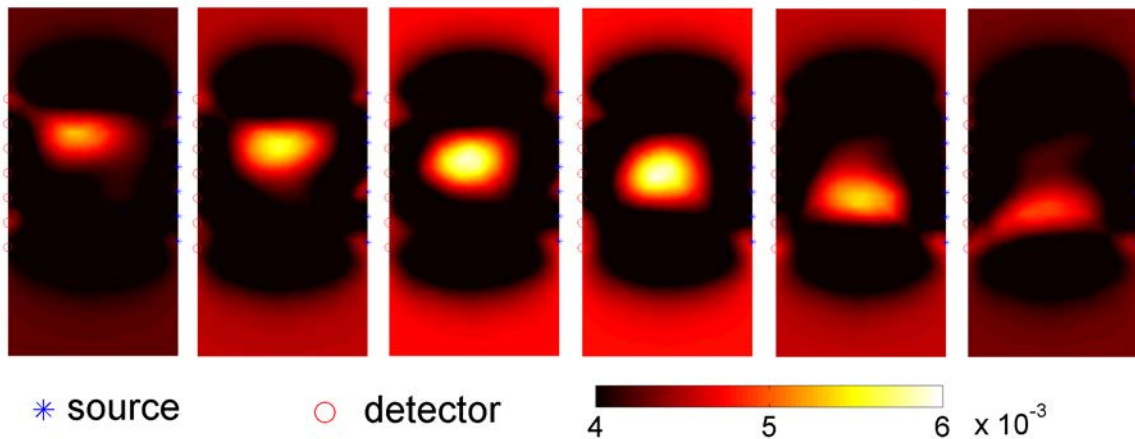


Figure 2.17. Images of the tube at different locations recovered with the direct reconstruction method.

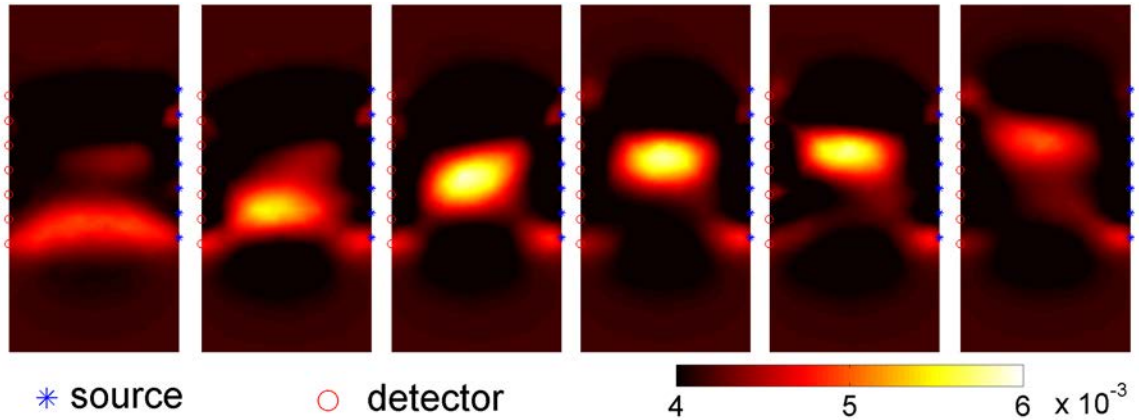


Figure 2.18. Images of the tube at different locations recovered with the difference reconstruction method.

## 2.5 Pulsatile Phantom Experiment

The clinical goal of this video-rate NIR tomography system was to image tissue hemodynamics. Thus a pulsatile phantom experiment was carried out to test the ability of this system to image an anomaly in real-time whose absorption property varied at a preset frequency and had moderate effect on the transmitted signal. The experimental setup is illustrated in Figure 2.19. Solution made of 1% intralipid and low concentration of indian ink was filled into a 72 mm thick slab-shaped high-density polypropylene bottle (32 oz HDPE Rectangular Bottle, Nalgene) to provide a homogeneous background with low  $\mu_a$ . The plastic bottle was colorless with a cloudy appearance that prevented straight light channeling laterally, so it was a fairly good container for this experiment. Several sides of the bottle were sealed with black tape to minimize the impact of boundary mismatch. Another tank held liquid solution of the same 1% intralipid and 3 times concentration of indian ink as that in the Nalgene bottle. So the absorption contrast of two solutions was 3:1. The high  $\mu_a$  solution was continuously pumped from the tank into a latex tube with

an internal diameter (ID) of  $\frac{1}{4}$  inch. This tube was connected to one end of a T-shape connector. The second end of the T-shape connector was connected to an outgoing clear vinyl tube with the same ID and directed the high absorbing solution back to the tank. A white balloon was tied up to the third end of the connector and sealed with water-proof glue. The connector was fixed on a three-jaw chuck with the balloon submerged into the low  $\mu_a$  solution in the Nalgene bottle. The incoming tube was periodically compressed by the rotational part of a pump (503U/RL, Watson-Marlow L.L.C.) at a preset frequency. The pump was driven by a frequency-adjustable 0~10 Volt square wave voltage generator. Therefore the high  $\mu_a$  solution was pumped through the T-shape connector in pulsatile mode at the same frequency, and so does the expansion and contraction of the balloon.

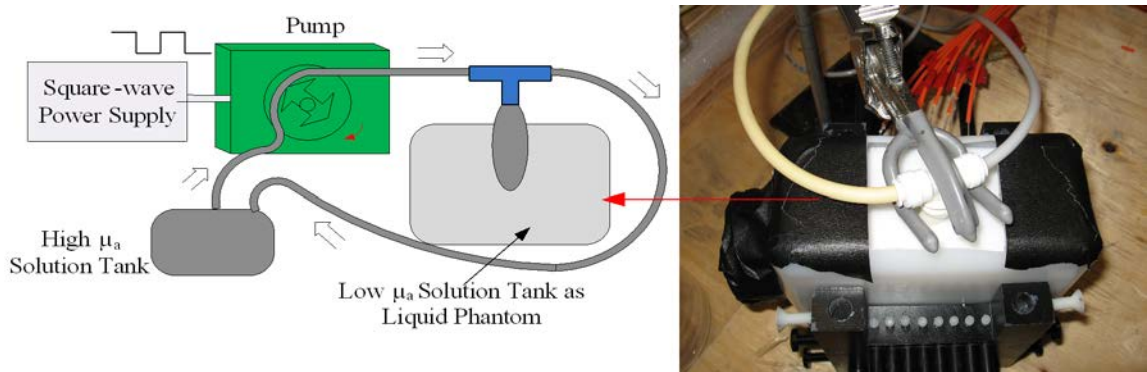


Figure 2.19. System setup of the pulsatile phantom experiment is shown. High  $\mu_a$  solution was continuously pumped through a balloon at 0.5 Hz. The balloon was submerged in a 72 mm thick slab container filled with low  $\mu_a$  solution. The absorption contrast of the solution inside the balloon against outside was 3:1. Eight LDs were launched as sources, and 6 CCDs were set as detectors to acquire data at 10 frames per second. Slit widths on all spectrometers were set to 100  $\mu\text{m}$ .

This pumping system was designed to mimic the periodical change in absorption seen in vaso-activity within tissue. The video-rate tomography system was used to image and recover this pulsatile change of the absorbing content, and quantify the magnitude of the effect upon the transmitted signal. The experiment was designed such that the elasticity of the balloon would only allow response below pumping frequencies of 1 Hz. 0.5 Hz was chosen as the pumping frequency for this experiment. Most of the high  $\mu_a$  solution was pumped through the T-shape connector directly. Only a small amount of the high  $\mu_a$  solution was pushed into the balloon because of the small pressure difference between the incoming and outgoing tubes. The volume of high  $\mu_a$  solution in the balloon and thus the size of the balloon would vary periodically according to the pumping frequency, but only on a very subtle scale which was barely apparent and not measurable. So the variation of  $\mu_a$  in the balloon was expected to be very small.

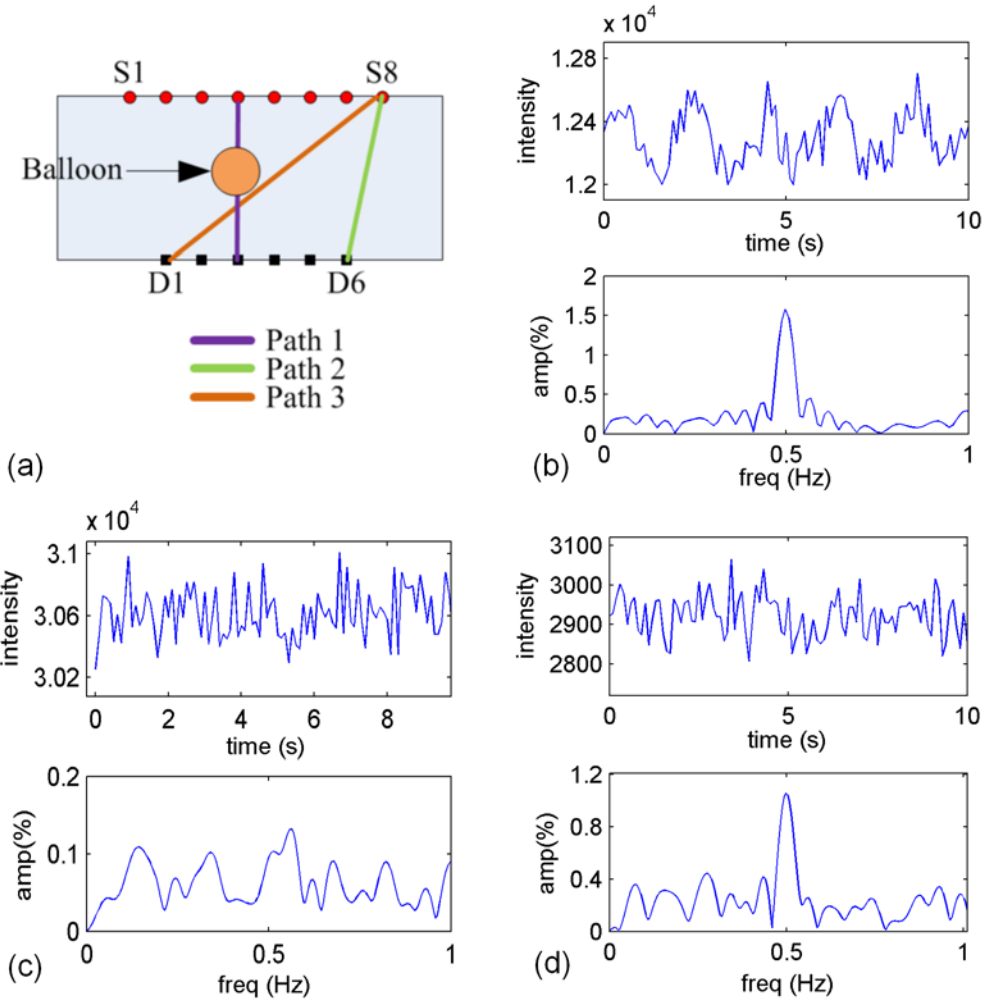


Figure 2.20. Raw signals of different S-D pairs in frequency domain. (a) illustrates the 3 different optical paths through the phantom with straight lines. D1 to D6 were 6 detection spots connected to spectrometers through detection fibers. S1 to S8 were 8 laser beam input spots connected to LDs through source fibers. (b) shows the time domain signal and its frequency domain spectrum of path 1. The frequency domain amplitude has been normalized to its mean value. (c) shows the time domain signal and its frequency domain spectrum of path 2. (d) shows the time domain signal and its frequency domain spectrum of path 3.

The detected signals for 3 optical paths in the frequency domain are displayed in Figure 2.20. After subtracting the mean value of each signal to remove DC component, each signal was Fourier transformed and normalized to the intensity of its DC component. The relative intensity of every frequency component in the frequency domain spectrum reflects the portion of signal caused by the varying portion of  $\mu_a$  versus that by the  $\mu_a$  background. It is obvious from Figure 2.20(b) that path 1, which was the shortest and went directly through the balloon, received the strongest 0.5 Hz pulsatile information which was up to 1.5% of DC component. Path 2 received almost no pulsatile signal since its light path was far from the balloon. Path 3 was the longest, but it did receive a moderate pulsatile signal because the balloon was in its light path. The pulsation part of flow below 1.5% is approximately what is seen in pulse oximetry, so this experiment is a good example with typical physiological signal level.

After imaging the pulsatile phantom at 10 frames per second for 20 seconds, the raw dataset was calibrated and put into the reconstruction program. Mean  $\mu_a$  of the balloon using direct reconstruction algorithm versus time is shown in Figure 2.21(a). It shows a blurry periodical trend, but it is hard to be distinguished from the noise. A Fourier transform was applied to the  $\mu_a$  curve, and the result was shown in Figure 2.21(b). Since the experimental imaging speed was 10 Hz, the highest distinguishable frequency after Fourier transform was 5 Hz. There is a peak right at 0.5 Hz, but several other peaks with similar intensity at higher frequencies made it not convincing to conclude the system had picked out the desired pulse. The result of difference reconstruction was not listed here, because the difference  $\mu_a$  was very small and could not be clearly discerned from reconstruction artifacts around.

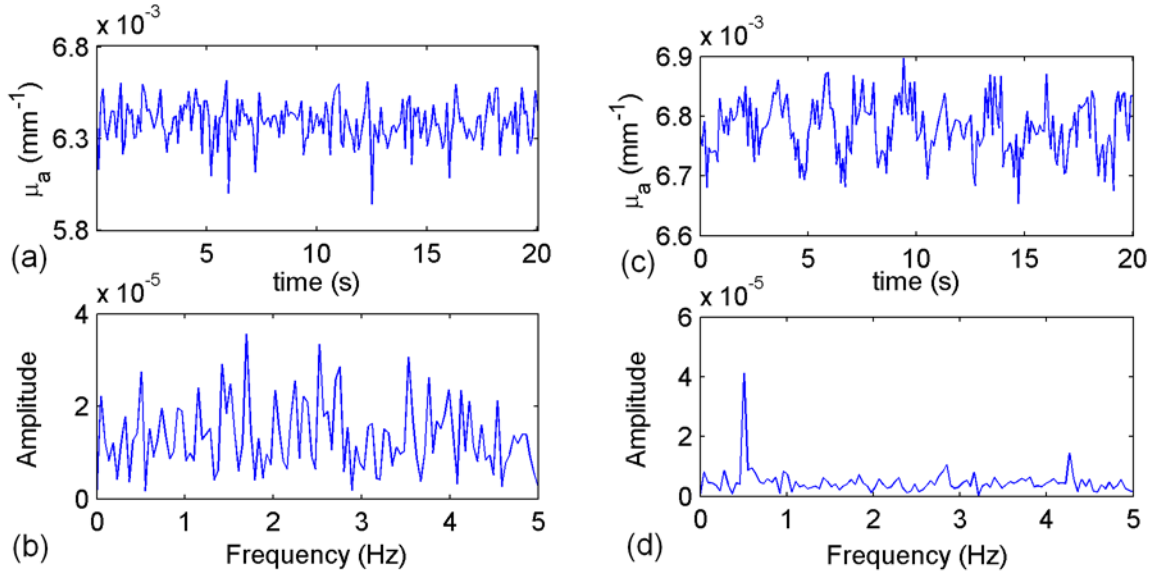


Figure 2.21. (a) Mean value of reconstructed  $\mu_a$  in the balloon versus time using direct reconstruction method. (b) Fourier transform of  $\mu_a$  in (a). (c) Mean value of reconstruct  $\mu_a$  in the balloon versus time using the region-guided reconstruction method. (d) Fourier transformed of  $\mu_a$  in (c), which shows the dominance of the 0.5 Hz signal in the frequency spectrum.

The region-based reconstruction method was also applied to this dataset. The two regions defined in this experiment were from direct measurement of the size of the container and the shape and location of the balloon. Since the change of the balloon size was too small to measure between the pulsatile motion, it was assumed to be constant. In Figure 2.21(c) the recovered  $\mu_a$  of the balloon versus time showed a clear periodical trend, and after Fourier transformation a sharp peak at 0.5 Hz was recovered in Figure 2.21(d), which is much higher than the background. This peak verifies that the region-based method does allow recovery of the pulsatile varying absorption content in the

balloon, because of its strong noise suppression and superior linear response, as discovered before in the static phantom experiment.

## 2.6 Summary

The goal of this system is to achieve high-speed imaging of the dynamics of blood pulsation, and to validate that this system can be used to recover subtle signals in tissues. These phantom experiments have shown the feasibility of using this single wavelength spectral-encoded tomography system to perform high speed imaging through thick tissues, of the size required in clinical breast imaging.

This system was built around CCD detection which allows only CW detection, and does not have the capability to image frequency domain data. This choice was intentionally made because PMT or APD cannot detect multiple wavelengths simultaneously without frequency modulation, and frequency modulation has its own problem of large signals overwhelming small signals. The tradeoff is the lack of the capability to accurately recover exact  $\mu_a$  and  $\mu_s'$  independently from one another. However the application of this system at this stage is focused on vascular pulsatile flow imaging, and in this case  $\mu_s'$  remains largely static. Thus the errors in assumed  $\mu_s'$  will mostly contribute to an overall offset of recovered  $\mu_a$ . And this offset could be small if a reasonable value of  $\mu_s'$  is used.

The static and dynamic phantom experiments in section 2.3 and 2.4 illustrated the ability of the system to image heterogeneities through tissue-like media of 7 cm thick at high speed. Both the direct and difference reconstruction methods worked well in recovering the anomaly in slab-shaped phantoms, especially when the contrast between the anomaly and the background was large enough. The benefit of the direct

reconstruction method is that the reconstruction result is a straightforward depiction of the distribution of  $\mu_a$ , while its flaws include slight overshoot in the reconstructed  $\mu_a$  values with small contrast of the anomaly and the background, and apparent artifact around boundaries caused by experimental noise. The difference reconstruction method is better at suppressing boundary artifact, but the position of the anomaly always shift a little towards the boundary, and the fitted homogeneous background doesn't have a clear physiological meaning. The region-based reconstruction method is the strongest in noise suppressing, and it has superior linear response even with small  $\mu_a$  contrast in the media, but it heavily relies on the prior structure information of the media, the heterogeneity in each region cannot be recovered, and it is not appropriate for imaging applications with moving regions.

In the pulsatile phantom experiments, the pumping system was used to create the challenge of accurately detecting very subtle periodic variation of absorbance. The tiny volume change of the anomaly resulted in 1% periodic change in the observed transmission signal. The  $\mu_a$  variation of the anomaly could not be usefully recovered with the direct and difference reconstruction methods, as might be expected for a system where the signal change is only 1% and the system noise always exists. Thus, the application of algorithms based solely on diffuse tomography will be limited in a realistic tissue imaging situation, without a significant improvement in signal to noise or calibration of the system. However, image-guided reconstruction of  $\mu_a$ , using a region-fitting based method, did recover the subtle signal changes with great SNR. Thus in the following sections of this thesis, this reconstruction method is utilized in the context of MRI-guided hemodynamic imaging.

## **Chapter 3. Dual-wavelength Near-Infrared Dynamic Oximetry Imaging System**

Regions with increased vasculature density and chaotic blood circulation within breast tumors can be used to distinguish the most aggressive parts of a tumor from the surrounding tissue. Tumors have increased hemoglobin levels and potentially decreased oxygen saturation [23, 24], and these two critical pathophysiologic biomarkers are detectable with NIR optical tomography. The system described in Chapter 2 can recover the spatial distribution of  $\mu_a$  at 785 nm, which represents the total absorbance of all chromophores at that wavelength. To make the video-rate NIR tomography technique more appropriate for clinical breast diagnosis, the system was updated to include one more wavelength band at 830 nm, aiming at recovering temporal spatial information about total hemoglobin ( $\mu_a$ ) and oxygen saturation ( $S_{O_2}$ ). The lasers were all injected into one side of the breast and the spectrometer detection was collected on the opposite side. This chapter describes this dual-wavelength band approach to NIR imaging which allows dynamic oximetry assessment.

### **3.1 System Design**

There are four major chromophores in breast tissue, i.e. oxyhemoglobin, reduced hemoglobin, water and lipid. Therefore at least four LD sources at different wavelength are required to fully recover the concentration of each chromophore, from which  $\mu_a$  and  $S_{O_2}$  could then be calculated. And that is why many NIR tomography systems apply a multi-spectral approach to measurement, with four to seven wavelengths. But it is hard to realize such a design with the spectrally-encoded laser diode technique, because currently

it is technically difficult to produce a CCD which has a spectrum coverage of hundreds of nanometers for widely separated laser wavelengths while maintain the resolution of sub-nanometer to distinguish between spectrally-encoded laser diodes within the same wavelength band. The combination of one grating with multiple CCDs inside a spectrometer may make this design feasible, but the cost and effort involved would be tremendous.

Facing these challenges, the only practically feasible design at current stage was to include one more spectral-encoded source band in addition to the existing 785 nm wavelength band. Dynamic information about HbO and Hb were chosen to be the target for this new dual-wavelength NIR tomography system, because they have relatively large temporal variation in vivo and can be used to calculate  $\mu_a$  and  $\mu_s'$  which are important biomarkers for breast cancer diagnosis, while the concentration of water, lipid, and prior information of  $\mu_s'$  are relatively constant over time and can be obtained from other imaging modalities, such as MRI or another multi-spectral NIR tomography system.

The 830 nm LDs were chosen as the second spectral-encoded source band for several reasons. Firstly, wider wavelength coverage and larger difference in absorption spectra are generally more beneficial for the recovery of chromophore concentrations. Since the maximum coverage of the spectrometer is about 55 nm with the 1200 grooves/line grating, the possible options for the second wavelength band were from 730 nm to 840 nm. Secondly, the isobestic point of the absorption spectra of Hb and HbO is at 805 nm. The crossing pattern formed around this isobestic point by  $\mu_a(Hb)$  and  $\mu_a(HbO)$  at 785 nm and 830 nm is more beneficial for the separation of Hb and HbO than that of the combination of 785 nm and 730 nm. Thirdly, there were many more LD

types and manufacturers to choose from at 830 nm, so it was much more economical to proceed with this wavelength.

Even so, it was much harder to find appropriate 830 nm LDs than 785 nm LDs. And a long time was spent in selecting 830 nm LDs whose wavelengths could keep stable at a fixed wavelength without mode hopping to other lasing wavelengths. Finally seven 830 nm LDs of three types (DL5032-001 from Sanyo, HL8325G from Hitachi, and LT015MD from Sharp) were selected and installed on the source cart to form the second wavelength band. To avoid saturating the CCDs, the LDs of both wavelength bands were settled on the same side of the slab interface in the following experiments, while all CCD detectors were coupled from the other side of the interface. To save space, seven fiber couplers were made, each of which had two 400  $\mu\text{m}$  core fibers threaded through and glued tightly, one connected to a 785 nm LD and the other connected to an 830 nm LD, as shown in Figure 3.1(a). These fiber couplers were inserted into the customized holes with 0.4 inch interval in between on the source side of the slab interface in the following experiments.

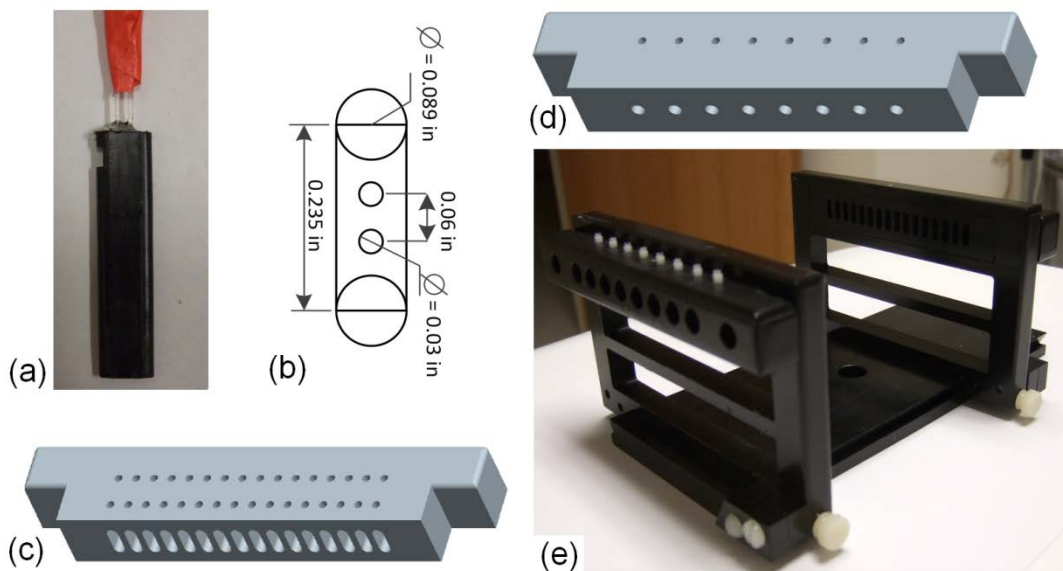


Figure 3.1. (a) The fiber coupler housing two 400  $\mu\text{m}$  core fibers. These two fibers were aligned vertically with 0.06 inch center-to-center distance. (b) The cross section dimensions of the fiber coupler. (c) The source fiber plate. (d) The detector fiber plate. (e) The tissue/phantom interface.

Seven spectrometers were used as detectors, and the center wavelength of the gratings was set to be 805 nm so that signals of all LDs of both wavelength bands could be covered. The normalized spectra of all laser LDs measured in turn by the same CCD are shown on Figure 3.2. The synchronization and data collection parts were the same as the single-wavelength system described in Chapter 2.

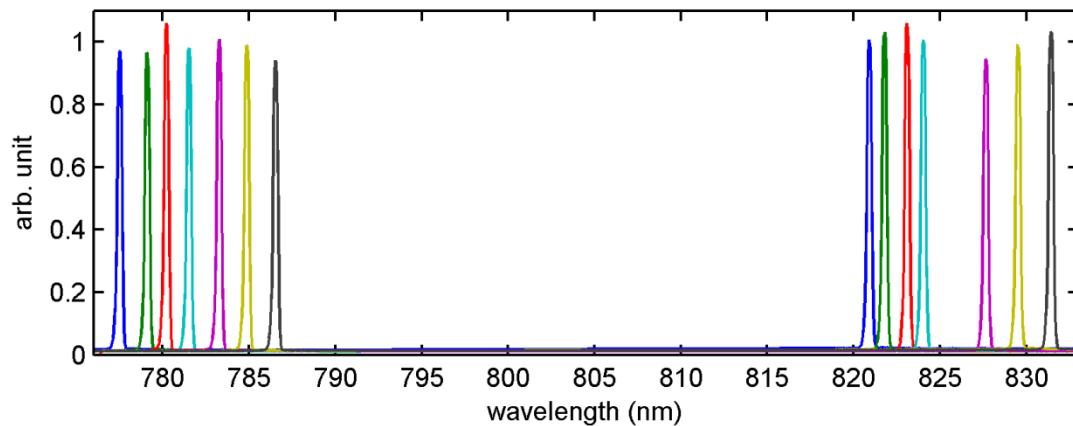


Figure 3.2. The spectra of 14 LDs of two spectrally-encoded source bands is shown as read out on a single spectrometer sequentially.

The stability of the output power and wavelength of the 830 nm band LDs were also tested in a 20 minutes continuous sampling experiment similar to the one did on 785 nm band LDs in section 2.1.1. And the results are shown in Figure 3.3. The output intensities of the seven 830 nm LDs with regard to time are shown in Figure 3.3(a). Besides the offset intensity differences caused by differences in LD output power and source-detector distances, there were obvious large hops of output power around the

minute and the minute. These were caused by mode hopping of the 830 nm LDs, which manifests itself by the lasing wavelength of a LD suddenly changing and mixing with the wavelength of another LD. This phenomenon could be seen in the wavelength stability plot shown in Figure 3.3(b). Fortunately the signal intensity variation caused from mode hopping and wavelength mixing was so large that those abnormal time points could be easily picked out of the final data with a customized automatic MATLAB routine. The standard deviation divided by the output power of the 830 nm LDs is shown in Figure 3.3(c), and the standard deviation of wavelengths of 830 nm LDs is shown in Figure 3.3(d), both of which were calculated after removing mode hopping points. Most 830 nm LDs showed output power variation between 0.4% and 0.8% except the first one. And the maximum wavelength deviation of 0.17 nm of LD #4 was deemed acceptable for use in the system once characterized. The optimal temperature and current setting for all 830 nm LDs are listed in Table 3.1. The optimal current and temperature settings of the seven 830 nm LDs are listed in Table 3.1.  $I_{\text{knob}}$  is the current setting on the rotating knob for the LDs. The knob has a range of 0.02 to 1.00 with 0.02 resolution. The actual LD current corresponding to this value can be measured on the current control board. The  $I_{\text{knob}}$  values of the and 830 nm LDs are the actual current value in the unit of mA, because their current control boards were of different types and were not connected to the knob or display screen.  $T_{\text{set}}$  is the preset temperature for a LD, and  $T_{\text{act}}$  is its actual temperature. The temperature corresponding to  $T_{\text{set}}$  and  $T_{\text{set}}$  can be calculated from a characteristic curve of the temperature control board. It has to be noted that these settings may need retuning every several months to compensate for the device aging.

Table 3.1. And a LABVIEW program customized to collect data of both wavelength bands from all the CCDs is shown in Figure 3.4.

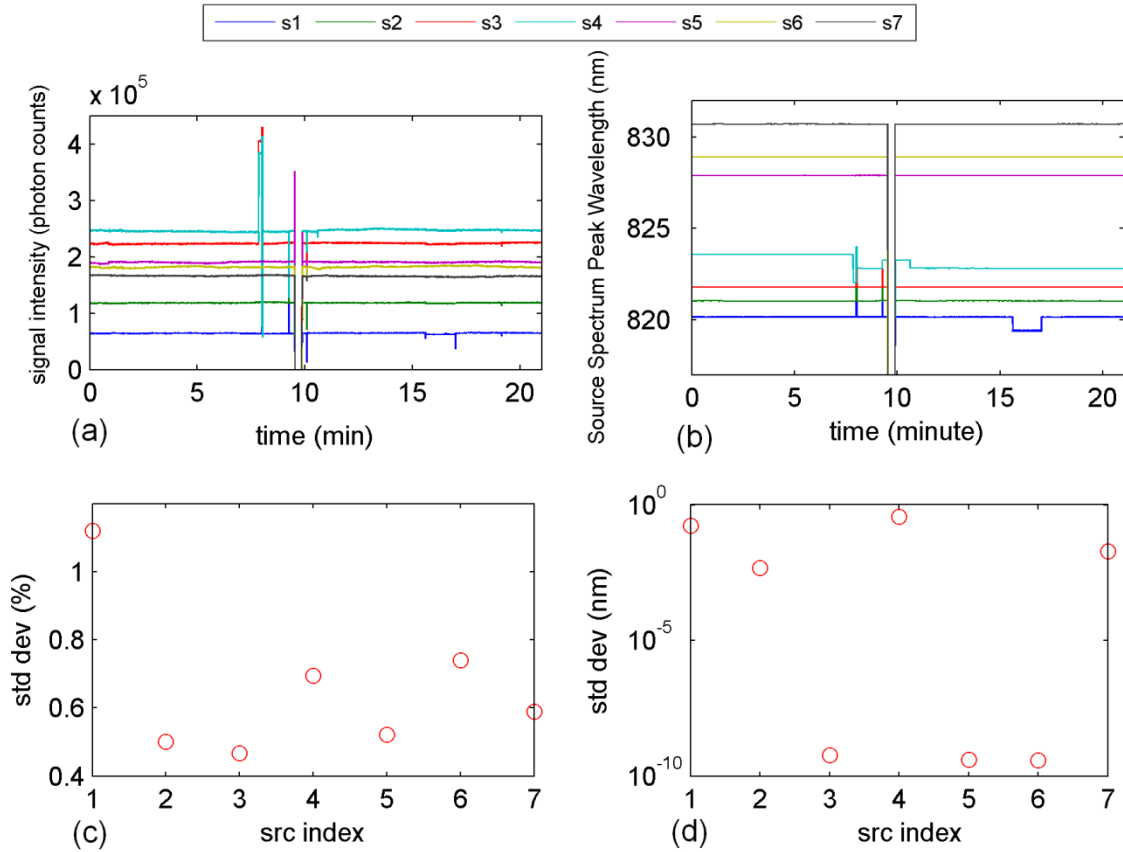


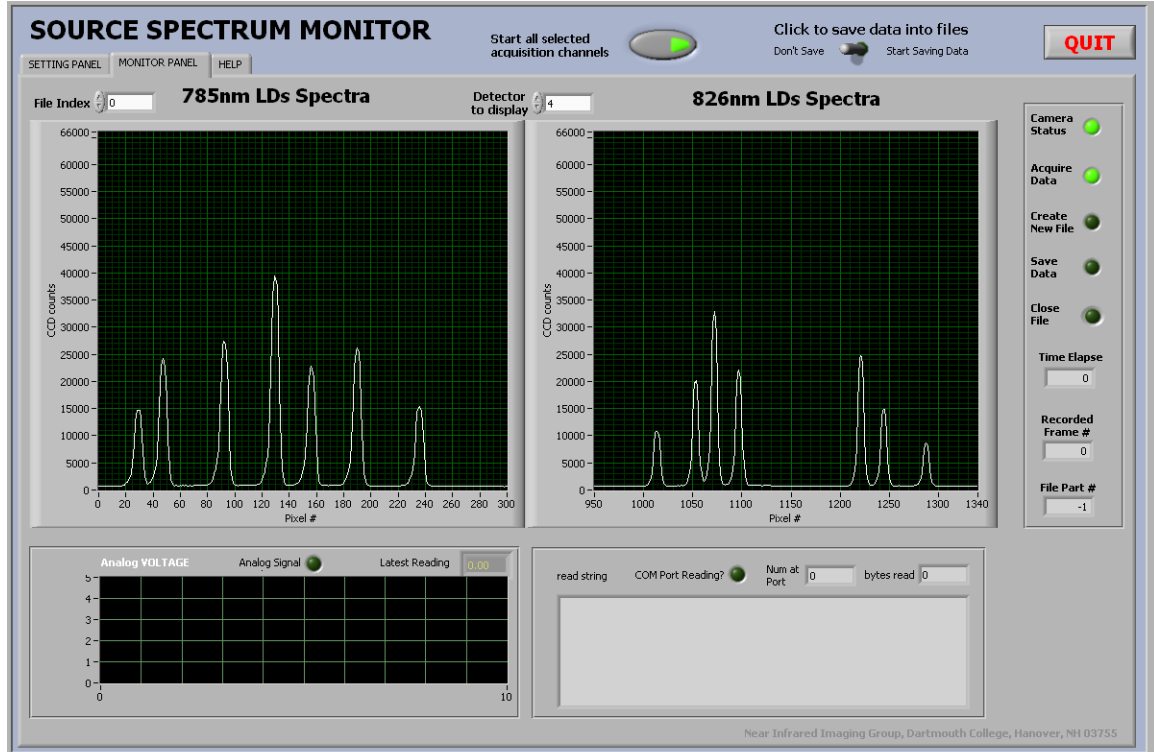
Figure 3.3. Stability test of the 7 LD sources in the 830 nm wavelength band are shown including: (a) The intensity stability of the LDs. (b) The wavelength stability of the LDs. (c) The standard deviation of intensity divided by the average intensity of the LDs. (d) The standard deviation of wavelength of the LDs.

The optimal current and temperature settings of the seven 830 nm LDs are listed in Table 3.1.  $I_{knob}$  is the current setting on the rotating knob for the LDs. The knob has a range of 0.02 to 1.00 with 0.02 resolution. The actual LD current corresponding to this value can be measured on the current control board. The  $I_{knob}$  values of the and 830 nm LDs are the actual current value in the unit of mA, because their current control boards

were of different types and were not connected to the knob or display screen.  $T_{set}$  is the preset temperature for a LD, and  $T_{act}$  is its actual temperature. The temperature corresponding to  $T_{set}$  and  $T_{set}$  can be calculated from a characteristic curve of the temperature control board. It has to be noted that these settings may need retuning every several months to compensate for the device aging.

Table 3.1. The optimal current and temperature settings for 830 nm LDs.

LD index	$I_{knob}$	$T_{set}$	$T_{act}$
1	0.490	1.973	1.885
2	1.000	1.553	1.553
3	0.984	1.635	1.634
4	0.980	0.978	0.979
5	87.1	1.869	1.796
6	1.000	1.190	1.189
7	100.8	1.081	1.081



(a)

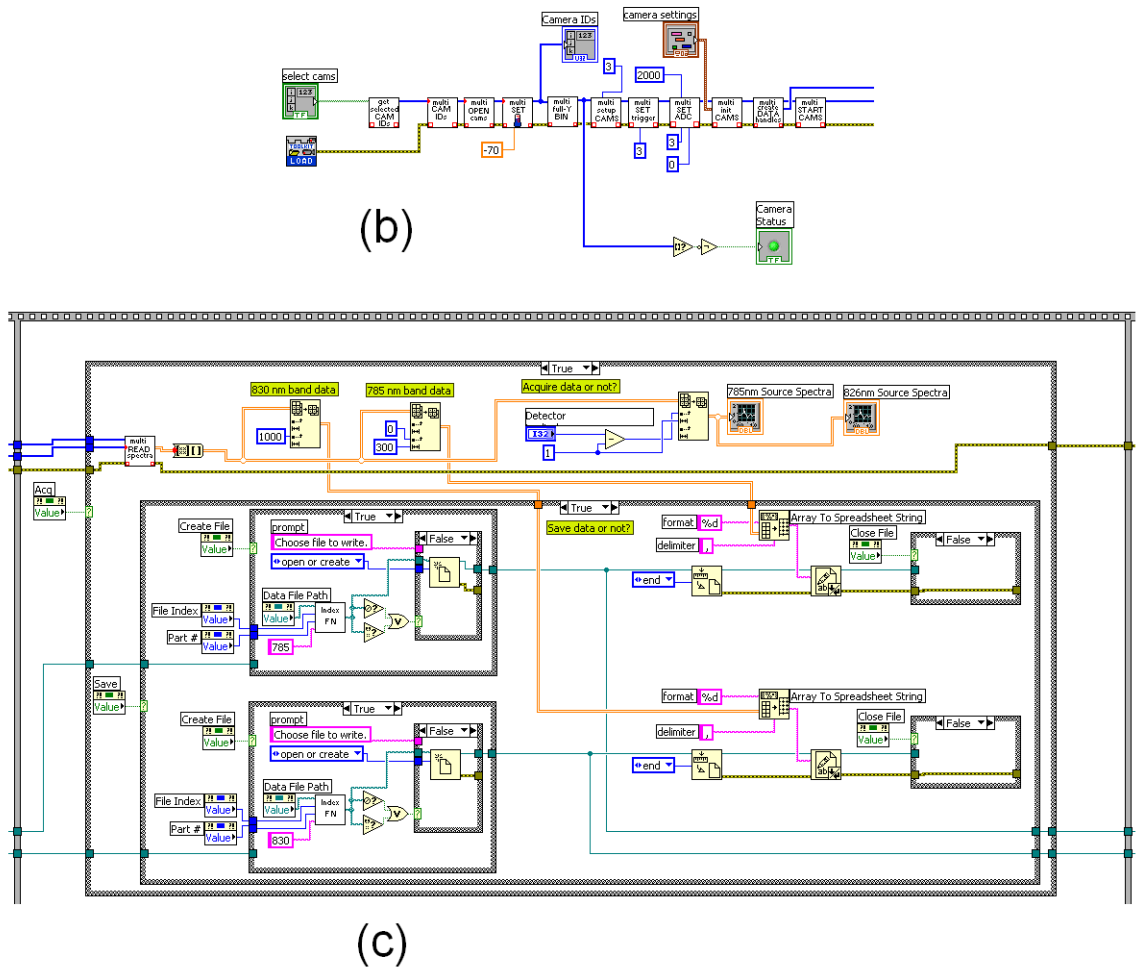


Figure 3.4. (a) The interface of the LABVIEW program to collect and display the spectra of detected signals on the CCDs. (b) The LABVIEW VI section to initialize all CCDs with preset parameters. (c) The LABVIEW VI section to collect and display data of all CCDs.

### 3.2 Total hemoglobin recovery

To accurately recover the total hemoglobin within the target media is an important function of this dual-wavelength system. A tissue-simulating phantom with a thickness of 63 mm and a lateral dimension of 120 mm was made from agarose powder, intralipid,

porcine whole blood and phosphate buffered saline (PBS), according to a previously published procedure [81], and is pictured in Figure 3.5. The 0.75% intralipid concentration of the phantom resulted in a reduced scattering coefficient  $\mu'_s$  of  $0.76 \text{ mm}^{-1}$  at 785 nm and  $0.72 \text{ mm}^{-1}$  at 830 nm [79]. was set to  $15 \text{ }\mu\text{M}$  in the phantom, which was within the normal range for level in human breast tissue. of the phantom were close to 100%, because of the fresh porcine whole blood used in making the phantom. The phantom included a cylindrical anomaly of 20 mm diameter in the middle of the phantom. The anomaly was first filled with a solution of  $15 \text{ }\mu\text{M}$  and 0.75% intralipid to make the phantom optically homogeneous, and a measurement was made. Then the solution in the anomaly was manually withdrawn with a syringe, and the anomaly was filled with a batch of solutions of increasing and constant 0.75% intralipid concentration. One measurement was made for each new solution. The of the solution batch increased from  $15 \text{ }\mu\text{M}$  to  $40 \text{ }\mu\text{M}$ .

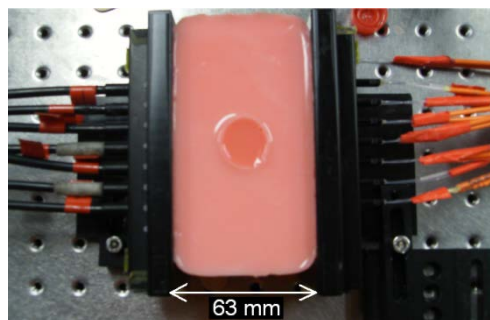


Figure 3.5. The agarose phantom with a liquid anomaly in the middle, used to vary hemoglobin levels in a single inclusion. The light sources were guided by the orange fibers on the right, and the black detection fibers on the left were connected to the spectrometers.

After compensating for the intensity of the different lasers and the efficiency of the detectors, each dataset was calibrated with the homogeneous measurement. A 2D slab-shaped mesh of 5249 nodes was created and segmented into the anomaly region and the background region according to the exact dimensions of the phantom. Then the region-based reconstruction method was applied to the datasets to fit for oxyhemoglobin and deoxyhemoglobin values. The results from a systematic increase in total hemoglobin and corresponding fits are shown in Figure 3.6.

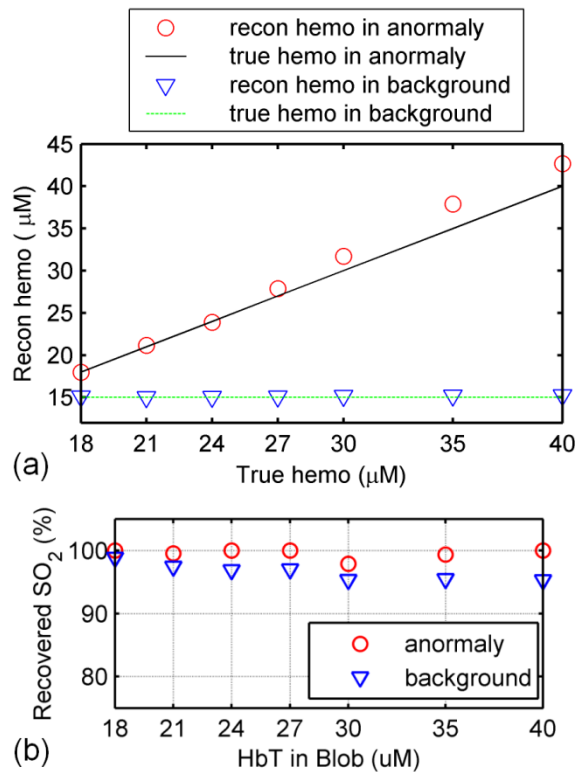


Figure 3.6. (a) The reconstructed and true total hemoglobin in the anomaly region and the background are plotted, showing the expected linear and flat trends. (b) The reconstructed  $\text{SO}_2$  in the anomaly and the background are shown, with less than 2% standard error in both cases.

The of both the background and the anomaly had small fluctuations, with approximately 2% error (standard deviation of the ratio between recovered and true ). The reconstructed of the background remained constant and agreed very well with the true value of 15  $\mu\text{M}$ . The of the anomaly agreed well with the true value for lower solutions, and was slightly overestimated with increased in the anomaly region. Besides system noise, hemoglobin residual from previous syringe withdrawn could be a cause, and local variations in total hemoglobin in the anomaly liquid might contribute as well. However, the largest absolute error was only 8.3% in the 35  $\mu\text{M}$  case, which was quite reasonable for breast imaging with this system, especially given there are only two wavelength bands and relatively narrow wavelength coverage.

### **3.3 Dynamic Oxygen Saturation Recovery**

Oxygen saturation is another important biomarker for breast cancer diagnosis. To test the system's ability to recover especially at high speed, a deoxygenation experiment with yeast was carried out. A slab-shaped agarose phantom identical to the one in Figure 3.5 was made and used as the background, while the anomaly in the middle was filled with solution of high concentration and 0.75% intralipid. A reflectance-based tissue oximeter (T-Stat 303, Spectros Corporation, Portola Valley, CA) was set up to monitor the in the anomaly simultaneously with the NIR system, as shown in Figure 3.7. The tissue oximeter utilizes a reflectance signal from the visible wavelength range of 420 nm to 700 nm for hemoglobin oxygenation spectral fitting, so its signal was filtered out by the grating on the NIR system and didn't contaminate the NIR signal on the detector, allowing both systems to operate at the same time. Yeast was added to the liquid anomaly region and mixed well immediately before measurements were recorded. The tissue

oximeter sampled at 1 Hz, while the sampling period of the NIR system was 60 ms. The entire deoxygenation process lasted for 10 minutes before the reading of the tissue oximeter settled to a constant value near 5% saturation, effectively showing the minimum value detectable for desaturation.

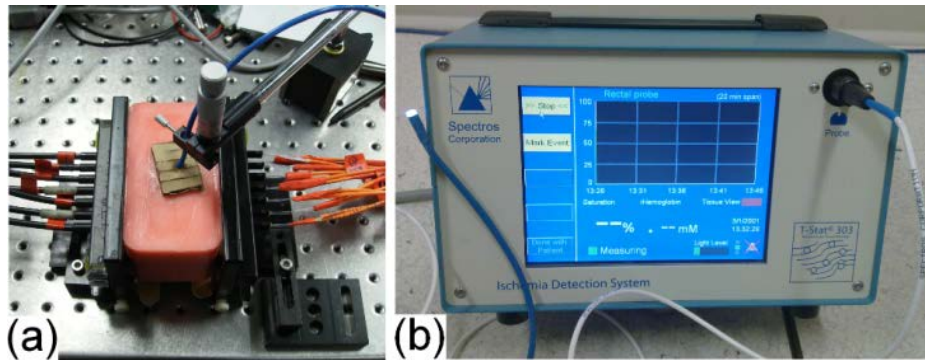


Figure 3.7. (a) The setup of the deoxygenation experiment is shown, with the blue probe of the reflectance tissue oximeter extended into the anomaly in the phantom. (b) The interface of the reflectance tissue oximeter (T-stat, Spectros Inc.).

The NIR data was calibrated and reconstructed frame by frame using the region-based reconstruction method. The reconstructed of the solution in the anomaly was plotted together with the reading from the tissue oximeter in Figure 3.8. Compared with the reading of the tissue oximeter (marked as reference in Figure 3.8), the slope of the curve of the NIR system was less steep, and the reading was slightly underestimated above 52% saturation and overestimated below this level. Although these two systems showed larger discrepancy for cases with very low situations, for most clinical applications where is usually above 40%, the difference of these two modalities was within a maximum of 10% difference. And if needed, the calibration of the NIR system should be easy since its reading was smooth and stable. The possible error of the

absorption caused by yeast in this experiment was not quantified, so the actual difference of these two systems could be even smaller.

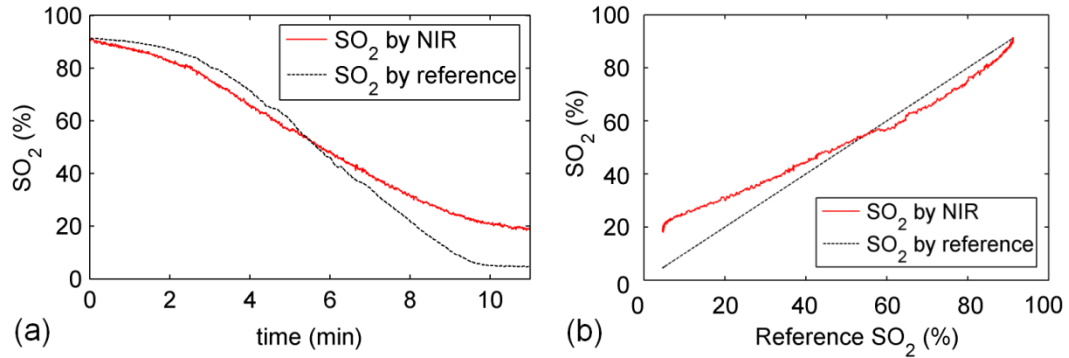


Figure 3.8. (a) The readings from the two modalities (visible reflectance probe *reference* and spectrally-encoded *NIR* tomography) versus time of the experiment are shown. The same data is replotted in (b) for from *NIR* tomography versus by reflectance probe reference.

### 3.4 Pulse Oximetry using NIR light

can be reconstructed from diffusion theory based finite element equations, and the value of the recovered is a static parameter indicating the ratio of HbO to in the volume of illuminated tissue. There is another NIR-based technique called pulse oximetry which can recover the of only the pulsing arterial blood. This ratio is usually called  $S_pO_2$ , and has been found to be clinically useful as stated in section 1.3. Therefore, it could be potentially useful for the clinical diagnosis of breast tissue if the  $S_pO_2$  of the breast tissue can be recovered from the NIR measurement with the dual-wavelength high-speed NIR tomography system. This section will explore the possibility of using the two wavelengths of this system to recover  $S_pO_2$  in thick tissue.

Pulse oximeters calculate  $S_pO_2$  from the light attenuation of two wavelengths, typically a red light wavelength (e.g. 660 nm) and a NIR wavelength (e.g. 940 nm). The signal processing technique of pulse oximetry is called the “Ratio of the Ratios”, which is based primarily on Beer’s law [19]. Take a finger pulse oximeter as an example. Absorbers in the finger include arterial blood, venous blood, bone, skin, muscle etc. Among these absorbers, the volume of arterial blood dominates the temporal change of the total absorbance, with diastole and systole phases being visible in the signal. So the time fluctuations of the transmitted light are caused mostly by the varying part of arterial blood.

The absorbance related to the static part of transmitted light can be defined as  $\mu$ , which is the combined absorbance of all the static absorbers and scatter attenuation. The absorbance of arterial blood is defined as  $\mu_A$ . The original optical path length is  $d$ , and the increase of optical path length caused by pulse arterial blood is  $\Delta d$ . Supposing the intensity of incident red light to be  $I_0$ , then average intensity of the transmitted light, or the static part, named  $I_1$  is:

$$I_1 = I_0 e^{-\mu \cdot d} \quad (3.1)$$

The minimum of transmitted light signal, named  $I_2$  is:

$$I_2 = I_0 e^{-(\mu \cdot d + \mu_A \cdot \Delta d)} \quad (3.2)$$

To eliminate the factors including the incident light intensity  $I_0$ , and the unknown and patient-dependent combined absorbance  $\mu$ , a ratio  $R$  is defined as:

$$R = I_2/I_1 = e^{-\mu_A \cdot \Delta d} \quad (3.3)$$

And for red light and near-infrared light, these two ratios can be obtained as  $R_R$  and  $R_{NIR}$ . The next step is to eliminate the unknown variable  $\Delta d$ . A ratio of the two ratios of two wavelengths, called  $RR$ , is defined as:

$$\begin{aligned}
 RR &= \frac{\ln(R_R)}{\ln(R_{NIR})} = \frac{-\mu_A(R) \Delta d}{-\mu_A(NIR) \Delta d} = \frac{\mu_A(R)}{\mu_A(NIR)} \\
 &= \frac{Conc(Hb_T) \times S_pO_2 \times EXT(HbO, R) + Conc(Hb_T) \times (1 - S_pO_2) \times EXT(Hb, R)}{Conc(Hb_T) \times S_pO_2 \times EXT(HbO, NIR) + Conc(Hb_T) \times (1 - S_pO_2) \times EXT(Hb, NIR)} \\
 &= \frac{S_pO_2 \times EXT(HbO, R) + (1 - S_pO_2) \times EXT(Hb, R)}{S_pO_2 \times EXT(HbO, NIR) + (1 - S_pO_2) \times EXT(Hb, NIR)} \tag{3.4}
 \end{aligned}$$

From Equation 3.4 it is apparent that the value of  $RR$  only relates to the absorbance of arterial blood at two wavelengths, which in turn is determined by  $S_pO_2$  in the arterial blood and the extinction coefficients of HbO and Hb at two wavelengths (shown as  $EXT(HbO, R)$ ,  $EXT(HbO, NIR)$ ,  $EXT(Hb, R)$  and  $EXT(Hb, NIR)$  in Equation 3.4). Based on Equation 3.4 a curve of  $RR$  *v.s.*  $S_pO_2$  can be calculated, from which the  $RR$  reading from a pulse oximeter attached on a human subject can be easily translated into the  $S_pO_2$  value for clinical usage. But this curve is directly derived from Beer's law which doesn't consider scattering in tissue at all, so calibration for this curve is necessary. Additionally, there are actually four kinds of hemoglobins in human, HbO, Hb, methemoglobin and carboxyhemoglobin, while this curve only considers HbO and Hb, which could be another source of error for the curve. Therefore all pulse oximeter producers develop their own empirical curve of  $RR$  *v.s.*  $S_pO_2$  from a large amount of patient sampling and calibration. Still the curve derived directly from Equation 3.4 can be used in this study to explore the possibility of using the two wavelengths of the high-speed NIR tomography system to recover  $S_pO_2$  in thick tissue.

A figure containing two curves of  $RR$  *v. s.*  $S_pO_2$  is shown in Figure 3.9(a). The curve PO  $\mu_a$  in Figure 3.9(a) only considers absorption, and was directly calculated from Equation 3.4 after bringing in the extinction coefficients of HbO and Hb at 660 nm and 940 nm. The curve PO  $\mu_{eff}$  in Figure 3.9(a) considers both absorption and scattering, and it was calculated by replacing  $\mu_A$  with  $\mu_{eff}$  in Equation 3.4, where  $\mu_{eff}$  is the effective attenuation coefficient, and its relation with absorption and scattering is:

$$\mu_{eff} = \sqrt{3\mu_a(\mu_a + \mu_s')} \quad (3.5)$$

The reduced scattering coefficient  $\mu_s'$  at two wavelengths was calculated from an approximation to Mie scattering theory:

$$\mu_s(\lambda) = A\lambda^{-SP} \quad (3.6)$$

where  $A$  is the scattering power, and  $SP$  is the scattering amplitude.  $A = 1.0$  and  $SP = 0.8$  were used in this figure. Although these numbers may not meet exactly with the practical situation, the trend and conclusion are the same. As shown in Figure 3.9(a),  $RR$  increases from 0.3 to 4.7 as  $S_pO_2$  varies between 0% and 100% on the curve PO  $\mu_a$ . This range of  $RR$  is much larger than that of the curve PO  $\mu_{eff}$ , which means the difference in pulsation amplitude of two wavelengths are larger and thus SNR is larger when only absorption is considered. And this is a very important reason why most pulse oximeters are designed to be used on very thin tissues such as fingers and earlobes where the impact of scattering is small.

The same calculation was performed on the 785 nm and 830 nm light of the NIR system, and the corresponding curves were plotted in Figure 3.9(b) as NIR  $\mu_a$  and NIR  $\mu_{eff}$ . Because the difference of absorption properties at these two NIR wavelengths is much smaller than that of the PO, the  $RR$  range of the NIR wavelengths to cover the

whole  $S_pO_2$  range is only about one sixth of that of the PO wavelengths, which means the SNR of the NIR system would degrade proportionally. Besides, it is apparent that the existence of scattering steepened the slope of the curve NIR  $\mu_{eff}$  and thus further reduced the SNR in half compared with the curve NIR  $\mu_a$ . The  $RR$  ranges to cover the whole  $S_pO_2$  range (0% to 100%) for the four curves in Figure 3.9 are 4.4 (PO  $\mu_a$ ), 1.9 (PO  $\mu_{eff}$ ), 0.64 (NIR  $\mu_a$ ) and 0.32 (NIR  $\mu_{eff}$ ). Since it is impossible to ignore the impact of scattering for thick breast tissue, the curve NIR  $\mu_{eff}$  is the one that applies to the thick tissue with the NIR system using the “Ratio of the Ratios” method, whose SNR is nearly one fourteenth ( $0.32:4.4 \approx 1/14$ ) of that of a typical PO.

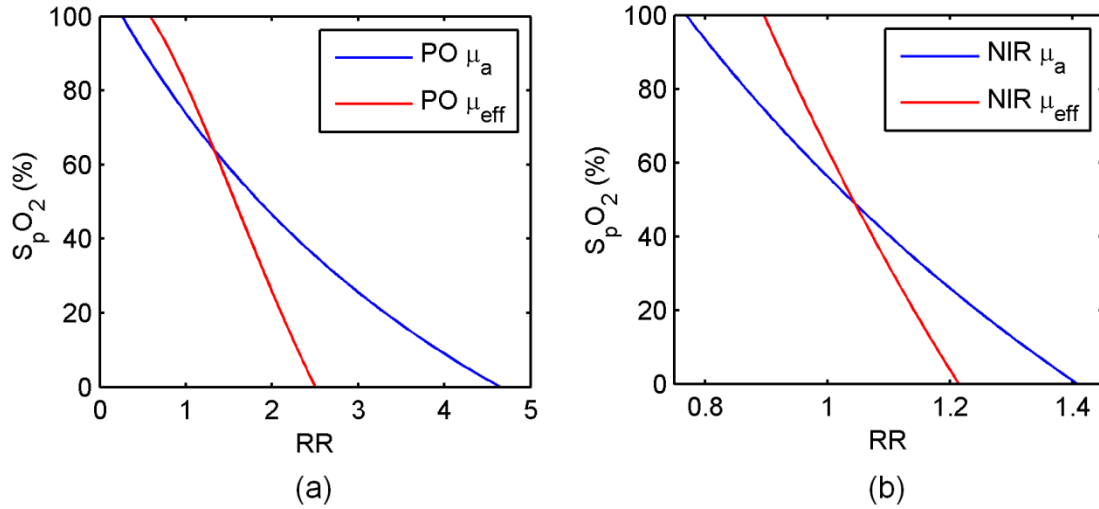


Figure 3.9. (a) The  $S_pO_2$  -  $RR$  curve when typical PO wavelengths (660 nm and 940 nm) are used. (b) The  $S_pO_2$  -  $RR$  curve when two wavelengths of the NIR system (780 nm and 830 nm) are used. Curves with a postfix of  $\mu_a$  only consider absorption, while curves with a postfix of  $\mu_{eff}$  consider both absorption and scattering.

To apply the “Ratio of the Ratios” method to the NIR system to measure  $S_pO_2$ , the first step is to test whether the severely deteriorated SNR of the NIR system is good enough to generate a stable output. If the system noise itself is large enough to disrupt the measurement, then this approach is definitely infeasible. To verify this, a balloon was filled with solution of 1% intralipid and diluted porcine whole blood and tied up. The balloon was then compressed between the slab phantom interface, with one source fiber and one detection fiber on each side. One 785 nm LD and one 830 nm LD was turned on as the sources, and one spectrometer was used as the detector to collect data at 20 Hz. The setup is shown in Figure 3.10.

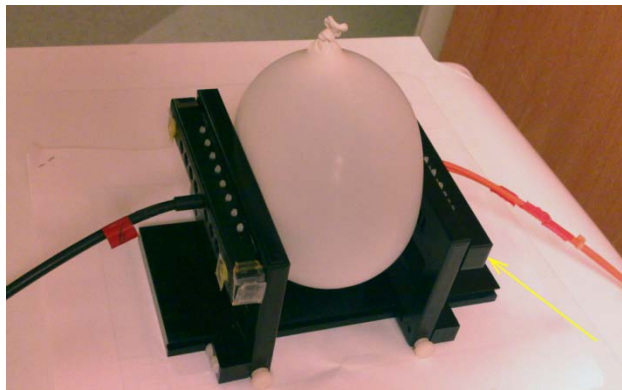


Figure 3.10. The experimental setup for the balloon experiment.

The source fiber plate was slightly tilted repeatedly at a constant rate in the direction of the yellow arrow shown in Figure 3.10 during imaging. The volume change of the balloon was tiny, so the varying absorbance of the balloon was caused mostly by the small variation of the path length of the blood solution between the fiber plates. This dynamic process was designed to mimic the very similar pulsation of the arterial blood flow. Because the composition of the solution inside the balloon didn't change, constant  $S_pO_2$  reading out of the measurement was expected. The whole imaging process took 150

seconds, and 10 seconds of the raw data of two wavelengths and their Fourier transform are shown in Figure 3.11 below. The raw data showed a clear periodic trend, and the Fourier transform spectra also showed a strong peak around 1.1 Hz. Three methods, which include direct calculation, statistical analysis based calculation, and frequency analysis based calculation, were used to calculate the  $RR$  value of the balloon experiment, trying to get stable reading of  $S_pO_2$ .

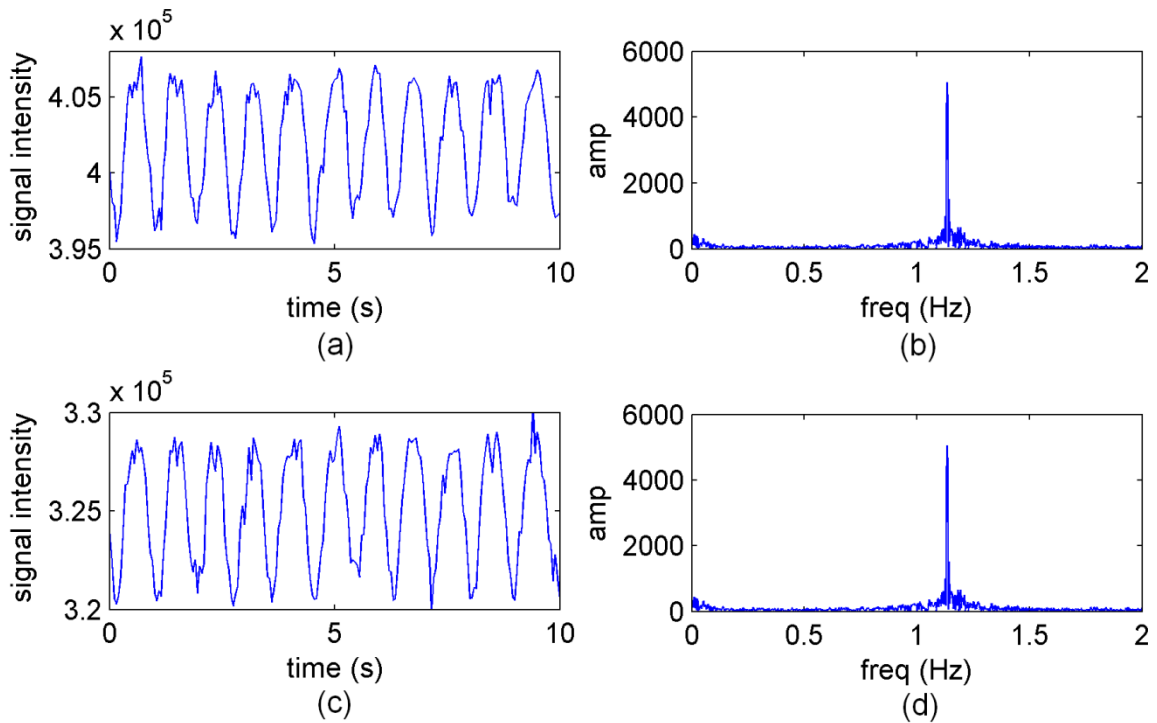


Figure 3.11. (a) A 10-second data stream of the 785 nm raw data. (b) The Fourier transform of (a). (c) A 10-second data stream of the 830 nm raw data. (d) The Fourier transform of (c).

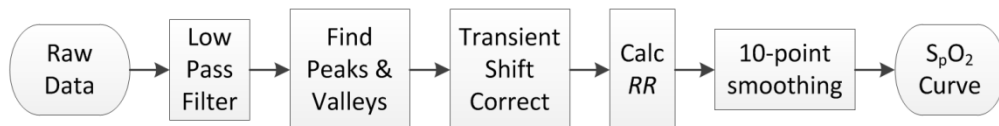


Figure 3.12. The flow chart of the direct calculation method to calculate  $RR$  and  $S_pO_2$ .

The flow chart of the direct calculation method is shown in Figure 3.12. This method was based directly on the idea of the “Ratio of the Ratios”. To calculate the value of  $RR$ , the peaks and valleys of the raw data of the two wavelengths are needed, where the peak values are used as  $I_1$  in Equation 3.1, and the valley values are used as  $I_2$  in Equation 3.2. But as shown in Figure 3.11, there were high frequency noises in the raw data from the NIR system which made it difficult to tell the exact positions of the true peaks and valleys. Thus a low pass filter was used at first to smooth the curve. The filtering process should not have altered the result, because the main frequency component of interest was preserved, and the principle of “Ratio of the Ratios” should be applicable to any non-zero frequency component of the pulsation. The second step was to calculate the forward difference, and the zero-crossing points were the location of peaks and valleys, as shown in an illustration in Figure 3.13.

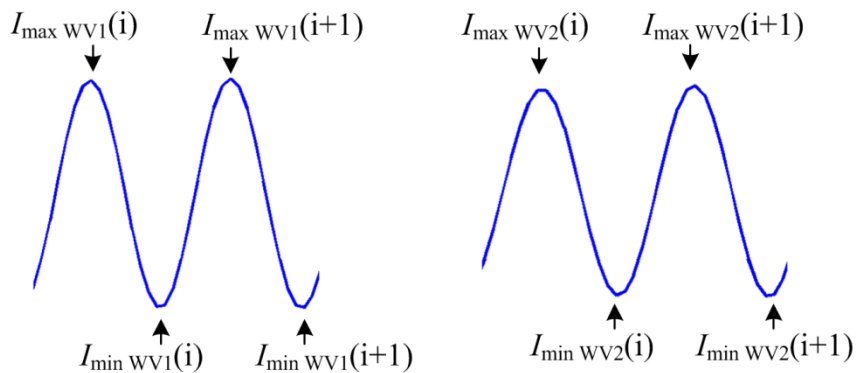


Figure 3.13. Illustration of finding peaks and valleys of detected optical signal of two wavelengths during the steady state in order to calculate  $RR$  values.

In order to avoid the influence of slightly changed source intensity, surrounding lighting, or average blood saturation which may result in a relatively large effect on the

difference in maximum and minimum intensity of the light levels, linear interpolation is commonly used to correct for the drift [19], which was the step 3 in Figure 3.12. An illustration of the optical signal under transient variation is shown in Figure 3.14, and the equation of the linear interpolation method is:

$$I_{\max}(i)^* = I_{\max}(i) + [I_{\max}(i+1) - I_{\max}(i)] \times \frac{[t_{\min}(i) - t_{\max}(i)]}{[t_{\max}(i+1) - t_{\max}(i)]} \quad (3.7)$$

where  $I_{\max}(i)^*$  is the peak value after correction. The correction for valley values was similar.

After the correction step, the  $RR$  value of the  $i^{th}$  period can then be calculated as:

$$RR(i) = \frac{\ln[I_{\max wv1}(i)^*/I_{\min wv1}(i)^*]}{\ln[I_{\max wv2}(i)^*/I_{\min wv2}(i)^*]} \quad (3.8)$$

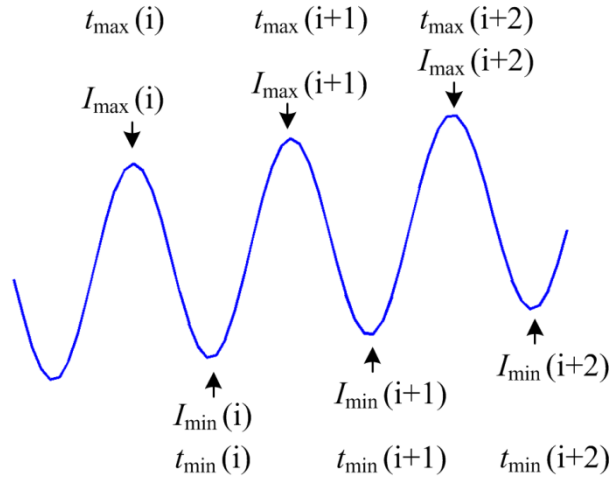


Figure 3.14. Illustration of a detected optical signal during transient state.

The  $RR$  curve was smoothed with the 10-point smoothing algorithm, based on which the  $S_pO_2$  curve could be calculated finally. The result is shown in Figure 3.15. The

stability of both the  $RR$  curve and the  $S_pO_2$  curve was not satisfying, as the recovered  $S_pO_2$  varied within a large range of 20% instead of being constant as expected.

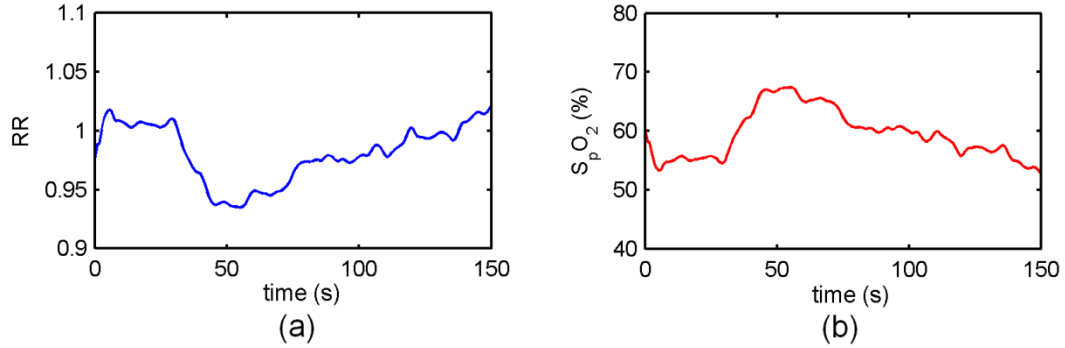


Figure 3.15. (a) The  $RR$  curve obtained with the first method in equation 3.8. (b) The  $S_pO_2$  curve calculated from (a) according to equation 3.4.

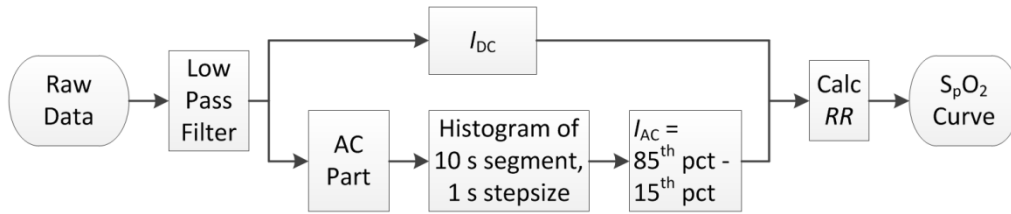


Figure 3.16. The flow chart of the statistical analysis based method to calculate  $RR$  and  $S_pO_2$ , where pct is short for percentile.

The flow chart of the statistical analysis based method is shown in Figure 3.16. Similar to the first method, the raw data at one wavelength was first low-pass filtered to remove high frequency noise. The intensity of the DC signal could be easily calculated by averaging local points. To get a stable estimation of the AC signal at every time spot, a histogram was generated from 10 seconds of data, and the difference of the percentile and the percentile was used as the intensity of the local AC signal. This process was repeated with 1 second step size throughout the data stream, and then repeated on the raw

data of the other wavelength. Then the  $RR$  value and  $S_pO_2$  could be calculated. The result obtained with this method is shown in Figure 3.17. Although this method was based on statistical analysis, the stability of both the  $RR$  curve and the  $S_pO_2$  curve with this method showed no improvement over that of the first method. But the general trends of both methods were similar.

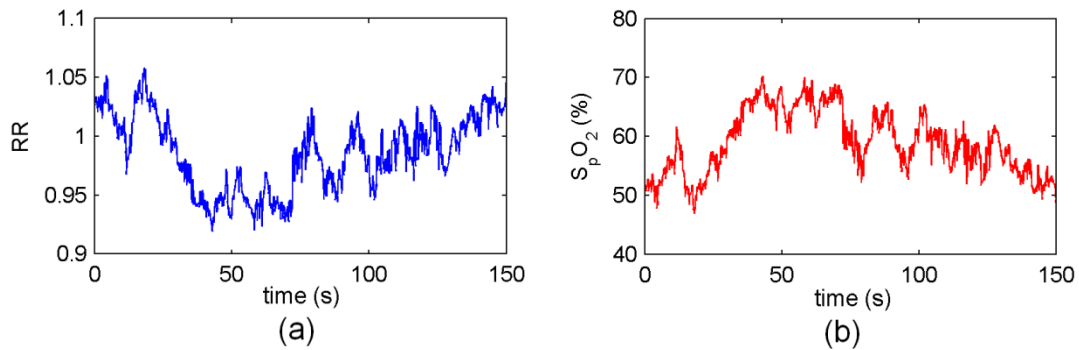


Figure 3.17. (a) The  $RR$  curve obtained with the statistical analysis based method. (b) The  $S_pO_2$  curve calculated from (a) is shown.

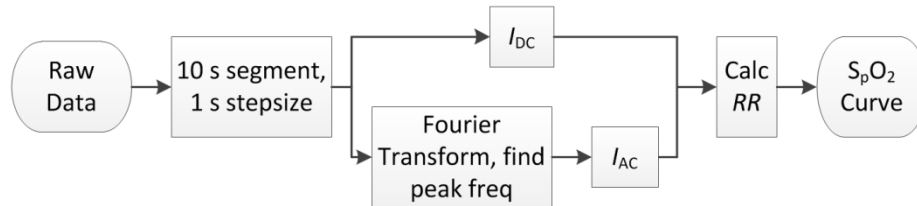


Figure 3.18. The flow chart of the frequency analysis based method to calculate  $RR$  and  $S_pO_2$ .

The flow chart of the frequency analysis based method is shown in Figure 3.18. Instead of finding the peaks and valleys of the raw data to estimate the intensity of the AC component, the third method calculated the intensity of the AC component directly through Fourier Transform of the raw data after removing DC component. The actual AC

component was chosen as the maximum intensity in the Fourier spectrum. The result obtained with this method is shown in Figure 3.19. This method generated the smoothest  $RR$  and  $S_pO_2$  curves compared with the other two, and the general trends of these three methods were similar. But the variation range of  $S_pO_2$  recovered was around 15% and still far from the constant value as expected.

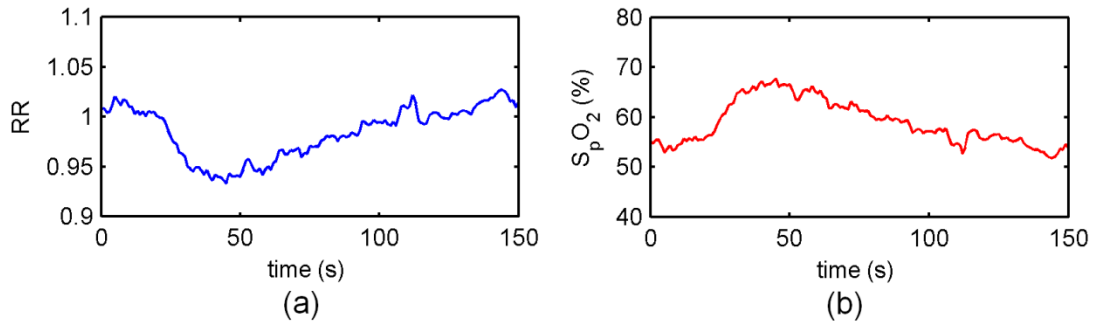


Figure 3.19. (a) The  $RR$  curve obtained with the frequency analysis based method.

(b) The  $S_pO_2$  curve calculated from (a) is shown.

As can be seen above, three different methods were examined in this balloon experiment, aiming at get a stable reading of  $S_pO_2$ . The first method was directly based on finding peaks and valleys to calculate  $RR$  and  $S_pO_2$ . The second method chose peaks and valleys within a stable range from statistical analysis to calculate  $RR$  and  $S_pO_2$ . The third method estimated the intensities of DC and AC components through Fourier Transform in order to calculate  $RR$  and  $S_pO_2$ . The curves of  $RR$  and  $S_pO_2$  generated from these three methods agreed with each other on the general shape and trend, while the third method gave the most stable and smoothest result. The small variation of  $RR$  between 0.93 and 1.03 could lead to a nearly constant curve of  $S_pO_2$  if the PO wavelengths were used. But for the two wavelengths of the NIR system, the

corresponding range of  $S_pO_2$  was between 52% and 67%. These large ranges are unacceptable for the balloon experiment where constant reading of  $S_pO_2$  were expected. The oxygen saturation status of the blood solution inside the balloon might vary during the experiment, but shouldn't be large since the balloon was sealed and remained static during the experiment. The small separation of the two wavelengths used on the NIR system should contribute the most to the unexpected large range of  $S_pO_2$ . As seen on Figure 3.9, for the same  $S_pO_2$  change, the corresponding change in  $RR$  with the PO wavelengths was about six times that with the wavelengths of the NIR system. And the existence of scattering in thick tissue further amplifies the difference to about 14 times. Thus the SNR of the NIR system is only about one fourteenth of that of the PO, which may push the NIR system out of the usable range with the "Ratio of the Ratios" method. As stated in Chapter 2, increasing the length of the spectrometer and the number of CCDs could sit wider separated LD wavelengths onto the NIR system, but the system would be much more complicated and expensive. So this "Ratio of the Ratios" method was not adopted in this study.

### **3.5 Summary**

The agarose phantom experiments with varying total hemoglobin and oxygen saturation have shown that, with known water content and scattering properties, it is feasible to use this two-wavelength NIR system to measure total hemoglobin and oxygen saturation at high speed *in vivo*. The region-based reconstruction method, which is based on the diffusion theory, demonstrated its capacity in linear response and noise

suppressing. And it will continue to be used to extract useful functional information from the breast tissue NIR measurements in the studies shown in the next chapter.

The stability of LDs doesn't appear as a problem for this system, since mode hopping didn't happen frequently during the 20-minute stability test, and abnormal signal intensities caused by mode hopping could be easily distinguished through customized MATLAB routines.

Pulse oximetry was experimented with the high-speed NIR system on a balloon phantom filled with a solution of dilute intralipid and whole blood to mimic the optical properties of soft tissue. Three different methods, all based on the working principle of pulse oximetry, were examined to calculate the value of  $S_pO_2$  from the two wavelength data, but none of these methods were capable of generating a stable reading of  $S_pO_2$  as expected. It was concluded that the small wavelength separation of the NIR system, combined with the high scattering in thick tissue contributes to the greatly decreased SNR of the NIR system, as compared to that of the commercial pulse oximetry set up. Therefore the pulse oximetry algorithm to estimate  $S_pO_2$  was determined to be not as useful for this NIR system.

## **Chapter 4. Human Subject Imaging Experiments**

In previous chapters, the high-speed NIR tomography system has demonstrated its capacity to image through tissue-like media of seven centimeters thick at 20 Hz. With two wavelengths, and prior knowledge of the scattering properties and the dimension of the anomaly, the system can recover hemoglobin content and oxygen saturation, as shown in a series of phantom experiments. In this chapter, a description of the system integration into a clinical MR is given, to monitor the variation of absorption properties in breast tissue at two wavelengths caused by breast hemodynamics of healthy human subjects, where the MR system was used to provide structural adipose and fibroglandular tissue for reconstruction. Possible error sources with the multimodal setup and their impact on absorption recovery were examined through simulation. Then two healthy human subjects were imaged with this multimodal imaging system and the results were shown.

### **4.1 Experimental Setup**

The concept of developing a hybrid system is powerful, in that it provides the maximal information content about the hemodynamics. The system requires careful integration of the NIR fibers into the breast MR imaging procedure. To avoid the co-registration error caused by patient motion in switching imaging modalities, it is best to collect MR images simultaneously with the NIR data in one patient scan. To realize this, both the source fibers and the detection fibers of the NIR system were extended into the MR scan room through tubes in the wall which were originally designed as brass waveguide feed-through for air vent. The fibers were fixed onto the breast interface through plastic set screws, which was in turn fixed inside a customized breast MR coil, as

shown in Figure 4.1. Co-registration of the two imaging modalities was realized by MR fiducials on the breast interface. The distance between adjacent sources on the breast interface was 0.4 inch, so the length of the source array was 2.4 inch for seven sources. The arrangement for detectors was the same, and on the other size of the breast interface. The human subject to be imaged would then lay prone on the breast coil on the MR bed, with the right breast gently compressed into a slab shape by the breast interface. A nurse would check the breast under pressure to make sure its width fully covered the array of sources and detectors on the breast interface, while the compression resulted in no pain to the human subject.



Figure 4.1. (a) A customized MR breast coil is shown. (b) The side view of the MR breast coil in which the breast interface was fixed with a phantom in between and fibers attached to both sides. The small yellow packets stuck onto the breast interface were MR fiducial markers.

In addition to the integration of the NIR tomography system and the MR scanner, a MR-compatible vital sign monitor (Veris Vital Signs Monitor, MEDRAD, Inc.) was also used in the MR scan room for the human studies. The probe of the monitor was attached to a finger of the human subject to provide continuous finger pulse oximetry reading of

the human subject during the imaging session. Besides the digital output of  $S_pO_2$  and heartbeat rate (HBR) reading at 1 Hz, the vital sign monitor could also output a continuous analog signal proportional to the intensity of the detected optical signal through the finger, which provided a convenient way to synchronize the measurement of the vital sign monitor with the NIR system.

The data acquisition of the NIR system was controlled by a customized LABVIEW program as shown in Figure 3.4 in Chapter 3, and another LABVIEW subroutine (Figure 4.2 as shown below) was added into that program to sample the analog signal of the pulse oximetry measurement at the same rate as the NIR imaging system, using a data acquisition board preinstalled in the console computer. The pulse oximetry reading was used as a frequency lock reference, which would be explained in detail later in this chapter. The whole experimental setup was shown in Figure 4.3, and the signal and data flow was shown in Figure 4.4. Two healthy volunteers have been examined by this multi-modal imaging system, and the results were discussed in the following sections.

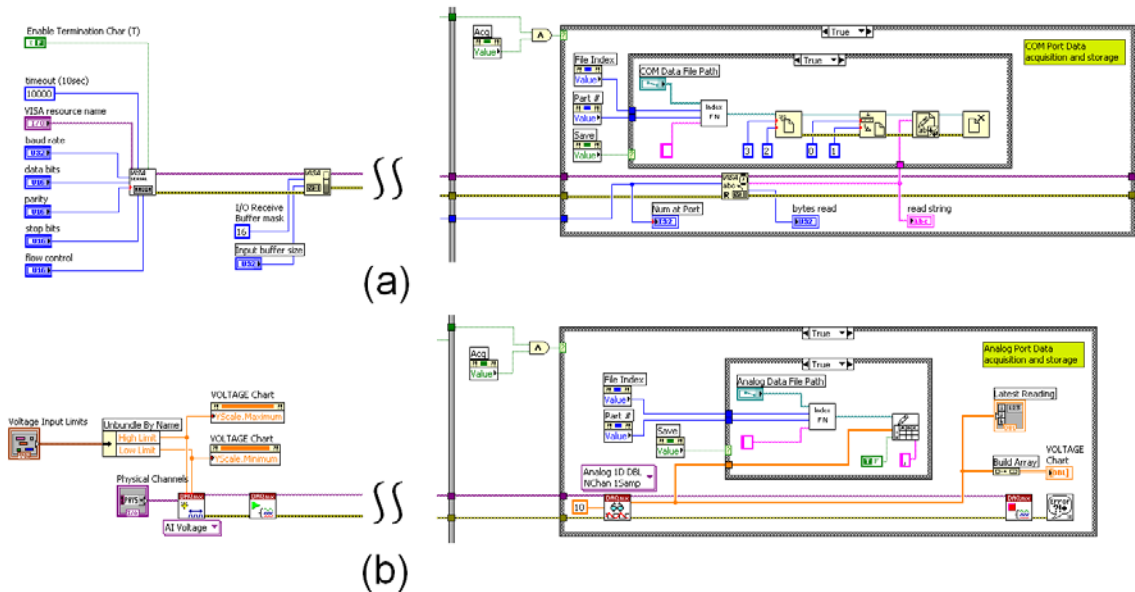


Figure 4.2. (a) The LABVIEW section to read the analog output of the vital sign monitor at the same speed as the NIR system is shown. (b) The LABVIEW section to read the 1 Hz digital output of the vital sign monitor is shown.

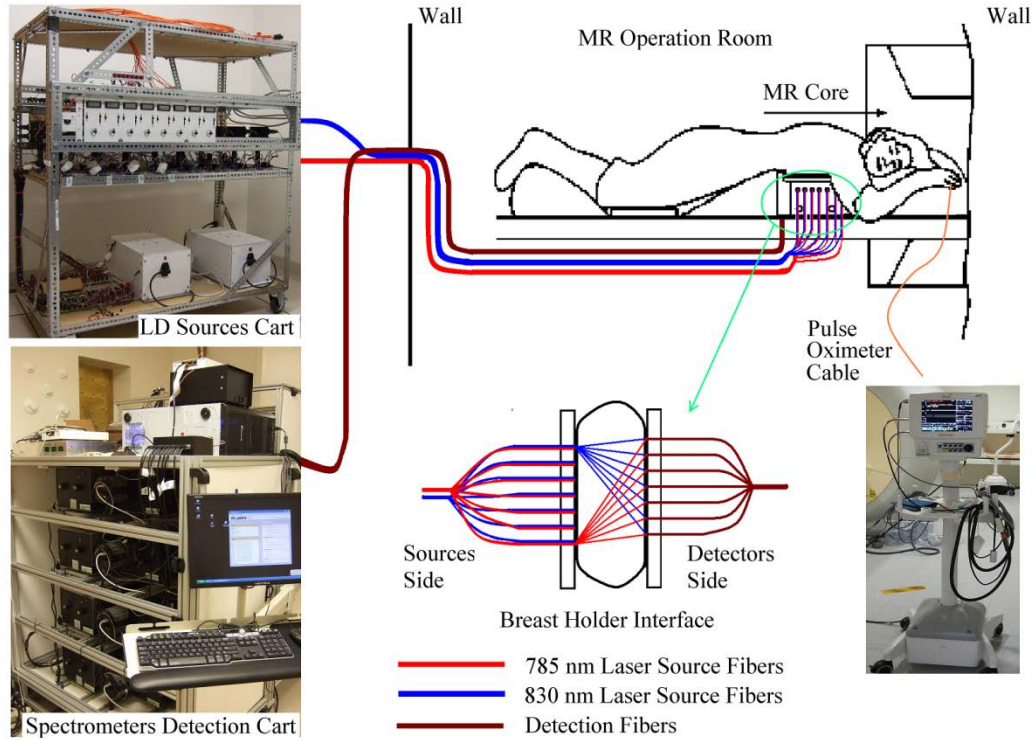


Figure 4.3. The experimental setup for breast imaging inside the MRI, showing the laser diodes and spectrometers (left) with fiber coupling into the MRI system (center). Data collection was synchronized with finger pulse oximetry (right) to monitor pulsatile flow data in a frequency locked manner.

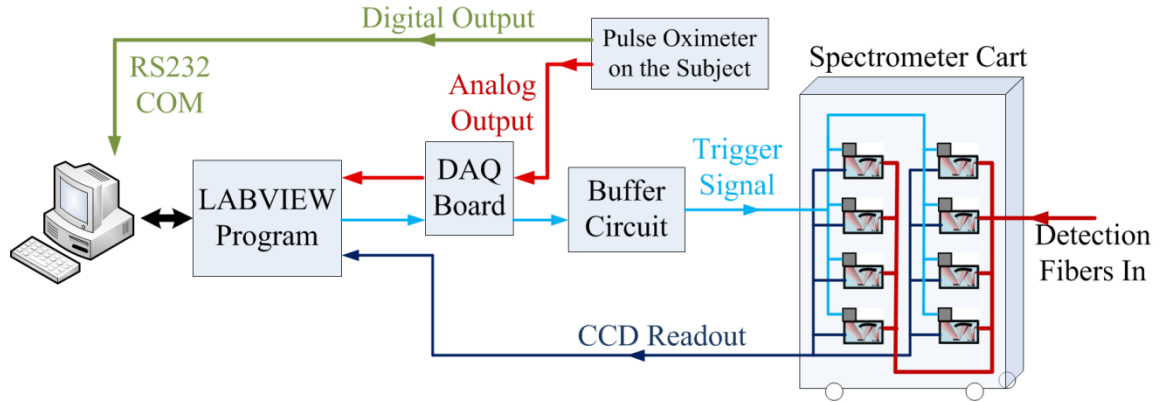


Figure 4.4. The flowchart of signal and data of the multi-modal experiment is shown. The spectrometers were connected with the computer through USB ports. The analog output of the pulse oximeter was connected to an I/O port of the DAQ board on the computer, and the digital output of the pulse oximeter was connected to the computer through 9-pin serial cable with RS-232 communication protocol.

## 4.2 Analysis of possible errors

Because the two-wavelength NIR tomography system was designed to reveal the small variations in  $\mu_a$  caused by breast hemodynamics, the response delay between different tissue types, e.g. the fibroglandular tissue and the adipose tissue, was of great interest in the clinical experiments. But the datasets obtained from clinical measurement are quite different from those from a well-controlled phantom experiment, where a lot of errors may come into play and distort the reconstruction result. This section would examine those possible errors related to the multi-modal imaging experiments, and estimated their influence on the reconstructed results through a series of pure simulations.

The errors examined in this simulation series included normally distributed coupling error, offset in the estimated size and position of the fibroglandular region, and

inhomogeneity of the heterogeneous medium. Additionally, since the NIR system needed prior knowledge about the scattering properties of the breast tissue, offsets in  $\mu_s'$  estimation of both tissue types were examined as well. In the simulations, the fibroglandular region was modeled as an anomaly region inside a phantom, and the adipose region was modeled as the background region of the phantom.

The dimension of the homogeneous phantom was  $143 \text{ mm} \times 70 \text{ mm}$  in this simulation. Its optical properties were set to be  $\mu_{a(homo)} = 0.006 \text{ mm}^{-1}$ , and  $\mu_{s'(homo)} = 1.0 \text{ mm}^{-1}$ . Seven sources with 0.4 inch distance in between were arranged on one side, and seven detectors with the same interval distance were on the other side. Since the homogeneous phantom was used solely for calibration, its true optical properties remained constant in the simulation.

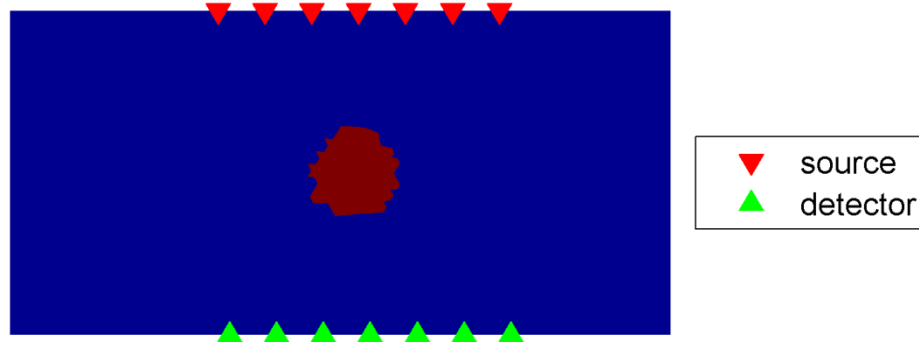


Figure 4.5. The geometry of the heterogeneous phantom used for simulation is shown. The 2D mesh contained 5249 nodes, and was discretized into triangular elements.

The heterogeneous phantom used for simulation was shown in Figure 4.5, with the same dimension and arrangement of sources and detectors as the homogeneous phantom. An anomaly with a radius of 10 mm was placed at the center of the phantom to mimic the

fibroglandular tissue region of the breast. The rest area of the phantom was used to represent the adipose tissue region. The time-averaged optical properties of the heterogeneous phantom were:

$$\mu_{a(heter)}(anom) = 0.008 \text{ mm}^{-1}, \mu'_{s(heter)}(anom) = 1.0 \text{ mm}^{-1};$$

$$\mu_{a(heter)}(BKG) = 0.004 \text{ mm}^{-1}, \mu'_{s(heter)}(BKG) = 0.6 \text{ mm}^{-1}$$

where “anom” was the anomaly, and “BKG” was the rest area of the phantom. A 1 Hz periodic component with the intensity of 1% of the averaged local  $\mu_a$  value was introduced into both regions of the heterogeneous phantom to mimic the pulsatile absorption properties in the breast tissue, where the phase of  $\mu_{a(heter)}(anom)$  was  $45^\circ$  ahead of that of  $\mu_{a(heter)}(BKG)$ .  $45^\circ$  was only a simulation setting of phase difference with no specific indication. The sampling rate of 20 Hz was adopted to mimic the high-speed NIR system, so that totally 200 frames of datasets could be generated through forward calculation, which represented a time length of 10 seconds.

The time span choice of 10 seconds came from the algorithm we developed to analyze the phase relation of two periodic signals, such as the variation of  $\mu_a$  in two regions of the human breast caused by pulsatile blood flow at the heartbeat rate. Originally we planned to study the time delay of  $\mu_a$  variation in different regions of the human breast. But later we found that the  $\mu_a$  curves had a wide frequency spectrum and it was difficult to find obvious landmarks to calculate the time delay. Thus the phase delay at the frequency of interest in two  $\mu_a$  curves became our next target, where usually the frequency with the largest intensity would be chosen. This phase delay in different tissue regions can provide information about the response delay of different locations or

different tissue types in the breast tissue, and may be potentially useful in the study of the dynamics of the breast tissue or the response of the breast to exogenous stimulation.

It was easy to calculate the phase difference of two curves of the same frequency, but first an effective signal processing algorithm was needed to pick out the frequency components of the same frequency from two  $\mu_a$  curves. One algorithm was proposed in our previous report [82], which dissembled the whole  $\mu_a$  curve into a series of frequency components with 0.02 Hz gaps in between each. Each frequency component had a very narrow frequency bandwidth and had the same length of the original  $\mu_a$  curve. Then the phase relation of two  $\mu_a$  curves in the same narrow frequency band could be easily analyzed. The limitation of this algorithm was that it was only robust to signals of very stable frequency. For the heartbeat rate of human which changes frequently, this algorithm cannot provide a viable method to track the correct temporal frequency of the heartbeat by itself.

To overcome this limitation, an improved phase analysis algorithm was proposed here. The new algorithm was still based on frequency analysis. But instead of treating the  $\mu_a$  curve as a whole, it treated only a small time segment of the  $\mu_a$  curve in which the heartbeat rate of the human subject was relatively stable. The frequency component with maximal intensity in this time segment was chosen as the main frequency component, and was used with the main frequency component of another  $\mu_a$  curve in the same time segment to perform phase analysis. Since the  $\mu_a$  curves of different regions are driven by the same heartbeat pulse, their main frequencies in the same time segment should be the same or very close. This algorithm was also more physiologically meaningful. The length of the time segment was chosen to be 10 seconds, because although shorter time segment

would provide better temporal resolution, it would also lower the frequency resolution of the Fourier transform itself.

The 10 seconds datasets forward calculated directly from the heterogeneous phantom with pulsatile absorption coefficients were accurate without any noise. The goal of the simulation was to examine whether the  $45^{\circ}$  phase difference introduced between two regions of the heterogeneous phantom could be successfully recovered with the existence of those errors mentioned above, and also to check how great the impact of these errors could be. Those errors were examined one by one to avoid ambiguity and complexity, as described below.

#### **4.2.1 Coupling error**

Although the procedure developed in section 2.2 can largely reduce the coupling error, it is practically impossible to ensure exact the same coupling on all source fibers in a phantom or breast measurement, and so do the detection fibers. The discrepancy in fiber coupling will distort the measurement data, and this distortion cannot be fixed by calibration. Besides, it was even harder to control the coupling error in clinical experiments than in well-controlled phantom experiments. Thus its impact has to be careful analyzed in order to justify any conclusion drawn from clinical results.

The coupling error has been usually modeled as normally distributed noise in the NIR measurement [83, 84], which was adopted in this simulation. Normally distributed (ND) noise was added into the forward calculated data of both homogeneous and heterogeneous measurement. Then the heterogeneous datasets were calibrated with the homogeneous data and were reconstructed frame by frame using the region-based reconstruction method. The intensity of the ND noise increased from 1% to 15% of the

datasets, with 1% step size. The true and reconstructed  $\mu_a$  curves of two regions with 5% ND noise were shown in Figure 4.6.

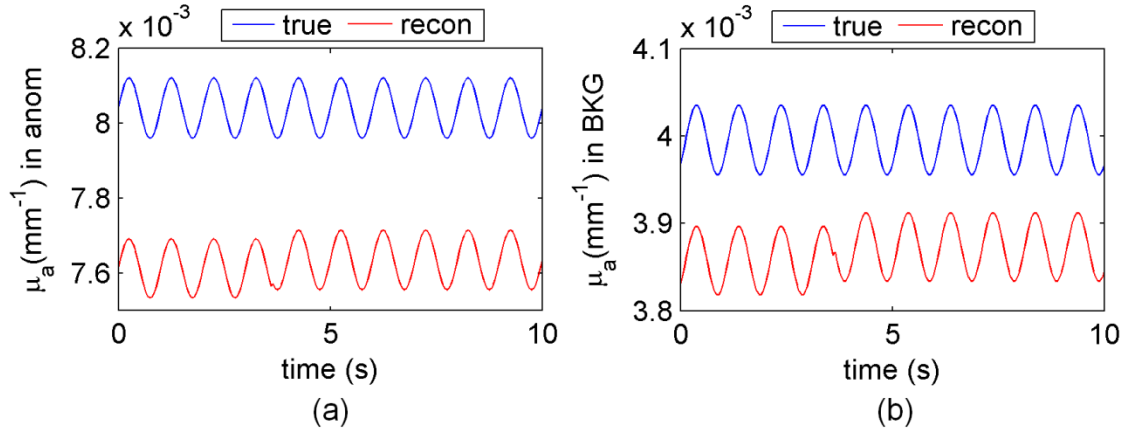


Figure 4.6. The reconstructed  $\mu_a$  curves with 5% normally distributed noise are shown along with the true values, where (a) is for the anomaly region, and (b) is for the background region.

It can be seen in Figure 4.6 that the reconstructed  $\mu_a$  curves well maintained the sinuous waveform despite small intensity variation. The reconstructed  $\mu_a$  values in both regions were smaller than the corresponding true values in Figure 4.6, but this was not always the case and totally depended on the noise added. The error in the reconstructed  $\mu_a$  was shown in Figure 4.7(a). The improved phase analysis algorithm was applied to the  $\mu_a$  curves, and the result was displayed in Figure 4.7(b).

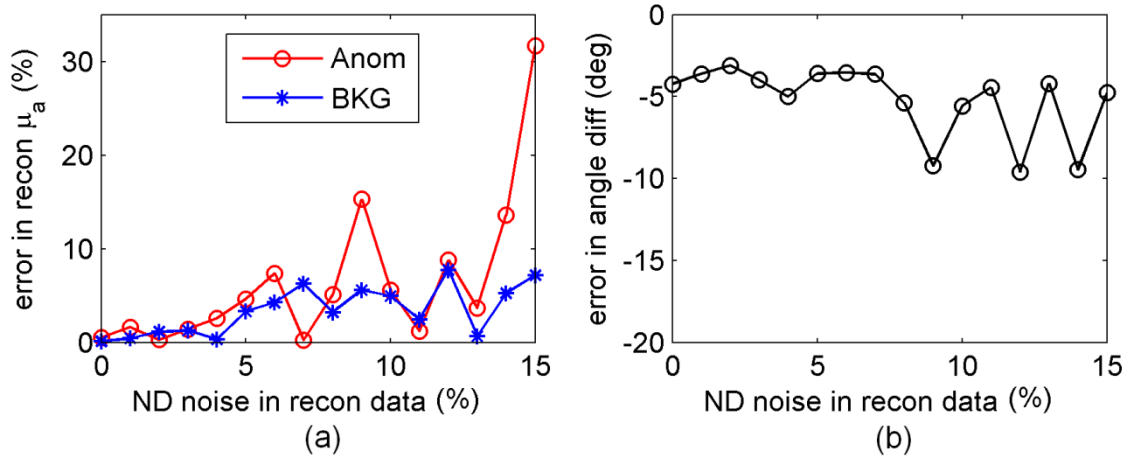


Figure 4.7. (a) The error in reconstructed  $\mu_a$  caused by normally distributed noise in the data is shown. (b) The error in reconstructed phase relation between the two regions caused by normally distributed noise in the data is shown.

Since the noise added onto the data was randomly generated, the curves in Figure 4.7 didn't follow a monotonous trend. But generally the error in reconstructed  $\mu_a$  increased with stronger ND noise. The ND noise had slightly larger influence on  $\mu_{a(heter)}(anom)$ , which was probably due to the smaller area of the anomaly region. For ND noise below 7%, it had little impact on the phase relation of the two regions. Because it is easy to control coupling error below 7% with the NIR system in clinical experiments, the phase relation should be trustworthy with this level of noise.

#### 4.2.2 Position of the anomaly region

The structural information of the breast tissue is essential to the NIR system, because the reconstruction method is region-based. Usually this information is obtained from a second imaging modality, where a mesh with the same dimension of the imaged tissue can be created and segmented into different regions based on the tissue structure.

Because of the possible error in the second imaging modality and during the co-registration of the two imaging modalities, the position of the anomaly could be slightly off from its true position, which could directly affect the reconstruction result.

To explore the impact of such error, the position of the anomaly in Figure 4.5 was shifted in the reconstruction mesh. The data for reconstruction was the forward calculated datasets with the correct anomaly position. The anomaly was firstly shifted several millimeters from left to right, and then up and down, and the reconstruction result of  $\mu_a$  and phase relation of the two regions were shown in Figure 4.8 and Figure 4.9 respectively.

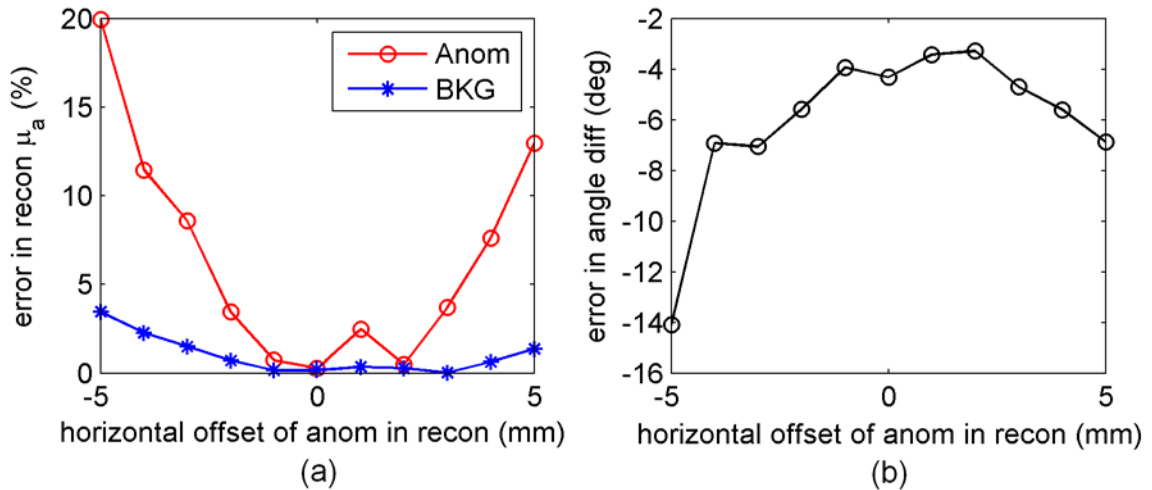


Figure 4.8. (a) The error in the reconstructed  $\mu_a$  caused by wrongly estimated horizontal position of the anomaly is shown. (b) The error in the reconstructed phase relation between the two regions caused by wrongly estimated horizontal position of the anomaly is shown.

The error of the reconstructed  $\mu_a$  value increased as the horizontal position offset of the anomaly increased, as shown in Figure 4.8(a). The larger error of  $\mu_a$  in the

anomaly region was reasonable because its position was wrongly estimated in reconstruction, but this error was not big for horizontal offset below 2 mm. The wrongly estimated horizontal position of the anomaly had very little impact on the phase relation of the two regions, where the error in phase was less than  $7^\circ$  for most of the cases.

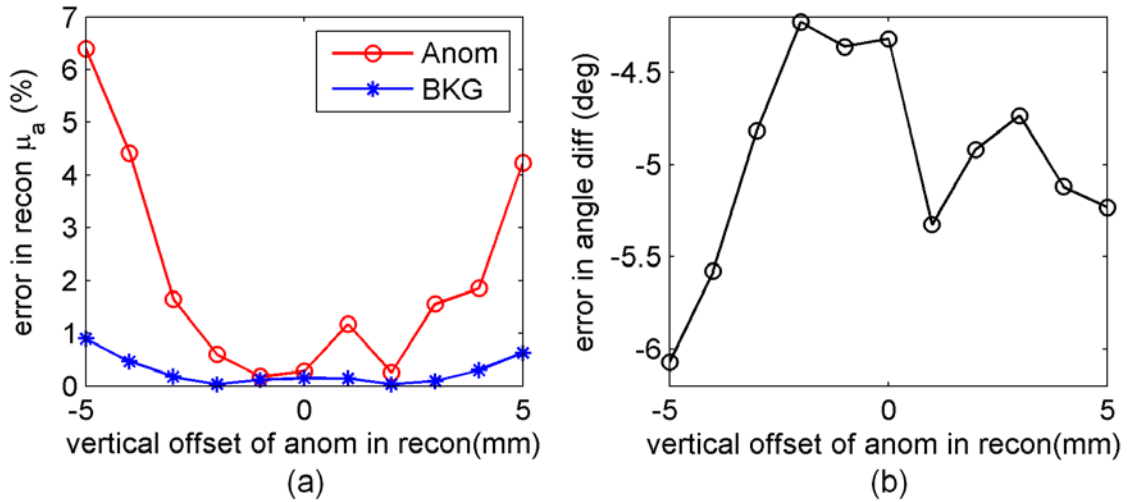


Figure 4.9. (a) The error in the reconstructed  $\mu_a$  caused by wrongly estimated vertical position of the anomaly is shown. (b) The error in the reconstructed phase relation between the two regions caused by wrongly estimated vertical position of the anomaly is shown.

The impact of the wrongly estimated vertical position of the anomaly was similar to that caused by the horizontal position offset, but smaller. The error in  $\mu_a$  values was below 2%, and the error in phase relation was below  $5^\circ$  for most cases.

With the sub-millimeter resolution of the second imaging modality such as MRI or X-ray, it is almost impossible to have a horizontal or vertical position offset of 5 mm as shown here. Therefore it might be expected that the error caused by the position shift should be very small in clinical experiments.

### 4.2.3 Size of the anomaly region

When the image domain is segmented according to the tissue types, it is more possible to have error in the estimated size of the anomaly than in the estimated position of the anomaly. This is because it is hard to accurately define the boundary of each tissue type on a gray-scaled image. So the anomaly region after segmentation may be either larger or smaller than the true size, and this error will affect the reconstruction result as well.

To explore the impact of this error, the radius of the anomaly in Figure 4.5 was changed between 5 mm and 15 mm, while its true radius was 10 mm. Region-based reconstruction was carried out on error-free forward calculated datasets and wrongly sized anomaly region. The error in the reconstructed  $\mu_a$  and the phase difference were shown in Figure 4.10.

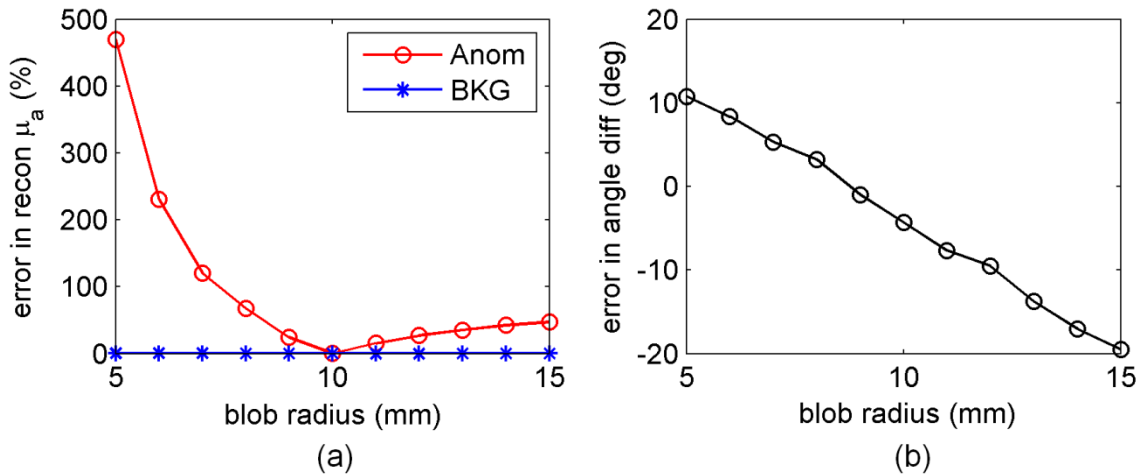


Figure 4.10. (a) The error in the reconstructed  $\mu_a$  caused by wrongly estimated anomaly size is shown. (b) The error in the reconstructed phase relation between the two regions caused by wrongly estimated anomaly size is shown. The true radius of the anomaly was 10 mm.

As shown in Figure 4.10(a), the anomaly size in reconstruction only affected the  $\mu_a$  value of the anomaly, while the  $\mu_a$  of the background remained almost constant. The impact on the  $\mu_a$  value of the anomaly was much smaller when the anomaly size was overestimated, indicating it is a safer option for imaging segmentation. The impact of wrongly estimated anomaly size on phase analysis was shown in Figure 4.10(b), where a clear linear relation was found. So even in the case where phase analysis is the target, the size of the anomaly shouldn't be overestimated too much.

#### 4.2.4 $\mu_s'$ of the homogeneous phantom

A homogeneous measurement is required to calibrate the heterogeneous data. And for the two-wavelength NIR tomography system,  $\mu_{s(homo)}'$  has to be pre-assigned because the NIR system works in continuous wave mode. Therefore it is worthwhile to explore the impact of wrongly pre-assigned  $\mu_{s(homo)}'$  to the  $\mu_a$  reconstruction and the phase analysis of the heterogeneous phantom. In this simulation,  $\mu_{s(homo)}'$  had a 50% error range of between  $0.5 \text{ mm}^{-1}$  and  $1.5 \text{ mm}^{-1}$ , where  $1.0 \text{ mm}^{-1}$  was the true value. In each case, the homogeneous data was forward calculated with the pre-assigned  $\mu_{s(homo)}'$ , and then the data was used to calibrate the heterogeneous datasets for region-based reconstruction. The error in the reconstructed  $\mu_a$  values and the phase difference were shown in Figure 4.11.

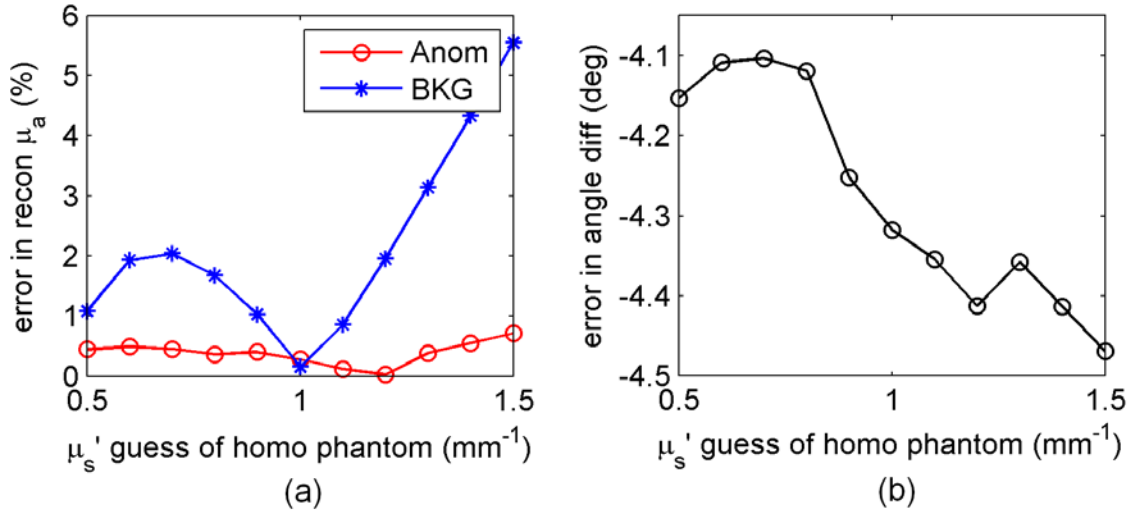


Figure 4.11. (a) The error in the reconstructed  $\mu_a$  caused by wrongly estimated homogeneous  $\mu_s'$  is shown. (b) The error in the reconstructed phase relation between the two regions caused by wrongly estimated homogeneous  $\mu_s'$  is shown.

The true value of the homogeneous  $\mu_s'$  was  $1.0 \text{ mm}^{-1}$ .

As shown in Figure 4.11(a) and (b), the error in pre-assigned  $\mu_{s(homo)}'$  alone had little effect on the reconstructed  $\mu_a$  value and the phase relation. The small variation of the numbers looked more likely due to the numerical calculation instead of error.

#### 4.2.5 $\mu_s'$ of the heterogeneous medium

Unlike the homogeneous phantom whose optical properties can be well characterized with a second imaging modality such as a multi-wavelength NIR tomography system [58] before a clinical experiment, the optical properties of the heterogeneous breast tissue of a human subject are usually unknown, and pre-assigned homogeneous  $\mu_s'$  values for all the tissue types have to be made for calibration and region-based reconstruction. In this process, three kinds of errors can be generated from

the different optical properties between the heterogeneous breast tissue and the reconstruction mesh consisting of homogeneous regions, and these errors were examined one by one in this section.

The first error is the heterogeneity of  $\mu_a$  and  $\mu'_s$  of the breast tissue. The region-based reconstruction method doesn't consider heterogeneity and assumes homogeneous  $\mu_a$  and  $\mu'_s$  values within each tissue region. The homogeneous values of each region can be treated as the average value of all nodes inside this region. But the distribution of  $\mu_a$  and  $\mu'_s$  in the breast tissue is heterogeneous in nature. Therefore the best bet is that the average value of  $\mu'_s$  in each region is accurately pre-assigned, and then the region-based reconstruction method can accurately recover the average value of  $\mu_a$  in each region. To examine this hypothesis, both  $\mu_a$  and  $\mu'_s$  of the heterogeneous phantom in Figure 4.5 were set to be normally distributed around the preset values, and then forward calculation was executed to generate datasets of heterogeneous measurement. After assigning accurate average  $\mu'_s$  values to the regions of the reconstruction mesh, the forward datasets were put into reconstruction to see whether the reconstructed  $\mu_a$  met with the preset average value of  $\mu_a$ . A wide range of normal distribution intensities, from 0% to 20% of the preset average value of  $\mu_a$  and  $\mu'_s$ , were examined and the results were shown in Figure 4.12.

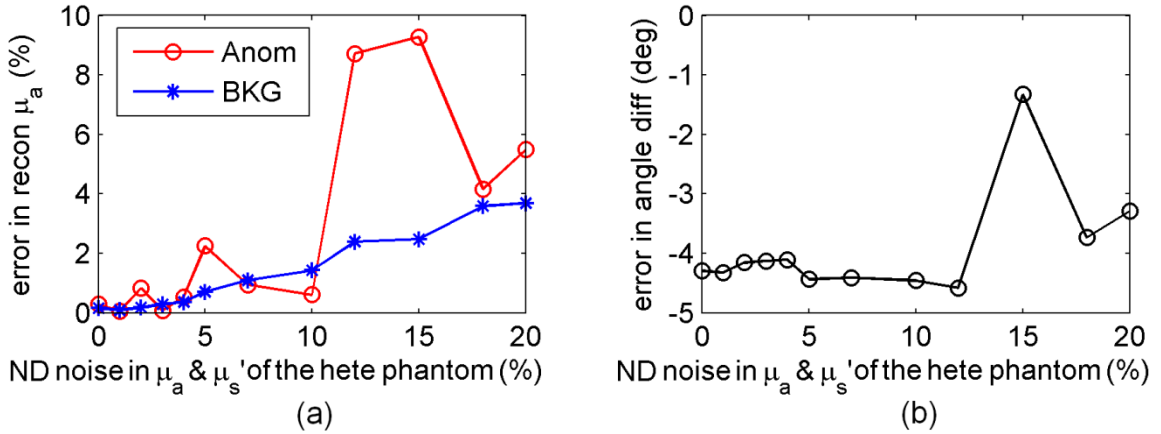


Figure 4.12. (a) The error in the reconstructed  $\mu_a$  caused by the heterogeneity of  $\mu_a$  and  $\mu'_s$  in the heterogeneous phantom is shown. (b) The error in the reconstructed phase relation between the two regions caused by the heterogeneity of  $\mu_a$  and  $\mu'_s$  in the heterogeneous phantom is shown.

As shown in Figure 4.12(a), the heterogeneity of  $\mu_a$  and  $\mu'_s$  of the heterogeneous phantom didn't bring in big error in  $\mu_a$  recovery with region-based reconstruction method. Even in the worst situation with 30% normally distributed noise in  $\mu_a$  and  $\mu'_s$ , the error in the reconstructed  $\mu_a$  was less than 10%. The impact of heterogeneity on the phase relation was even smaller. The error of the phase relation was below  $4^\circ$  in all cases, meaning the impact of heterogeneous optical properties was negligible.

The second error source is wrongly estimated average value of  $\mu'_s$  of the fibroglandular tissue in the breast. Although reference values about  $\mu'_s$  can be obtained through previous accumulated human subject scans [61], they can only provide a range of  $\mu'_s$ , and each human is different. So offset in  $\mu'_s$  assumption does exist, and its impact on  $\mu_a$  reconstruction should be examined.

To simulate this situation, the value of  $\mu'_{s(heter)}(anom)$  in the reconstruction mesh was varied between  $0.7 \text{ mm}^{-1}$  and  $1.3 \text{ mm}^{-1}$ , where  $1.0 \text{ mm}^{-1}$  was the true value. So the maximum error introduced was 30%. The data for reconstruction in every case was the forward calculated dataset with accurate value of  $\mu'_{s(heter)}(anom)$ , because  $\mu'_s$  assumption only affected the reconstruction. The error in the reconstructed  $\mu_a$  values and the phase difference were shown in Figure 4.13.

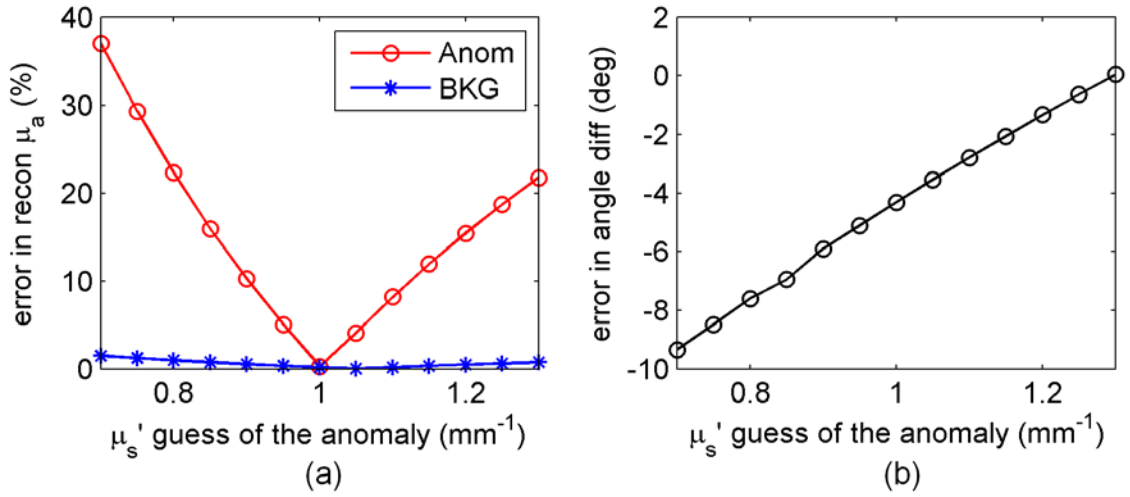


Figure 4.13. (a) The error in the reconstructed  $\mu_a$  caused by wrongly assumed  $\mu'_s$  in the anomaly region is shown. (b) The error in reconstructed phase relation between the two regions caused by wrongly assumed  $\mu'_s$  in the anomaly region is shown. The true  $\mu'_s$  in the anomaly region was  $1.0 \text{ mm}^{-1}$ .

As shown in Figure 4.13(a), the wrongly assumed  $\mu'_{s(heter)}(anom)$  had a large influence on  $\mu_{a(heter)}(anom)$ , while its impact on  $\mu_{a(heter)}(BKG)$  was much smaller. Similar to the conclusion about anomaly size in section 4.2.3, overestimating  $\mu'_{s(heter)}(anom)$  led to smaller error than underestimating it. The impact on the phase analysis was shown in Figure 4.13(b), where a good linear relation was found. Generally

the error in the phase difference was smaller than  $10^0$  even when 30% error was introduced into the pre-assigned  $\mu'_{s(heter)}(anom)$ .

The third error source is wrongly estimated average value of  $\mu'_s$  of the adipose tissue in the breast. The reason is similar to that of the fibroglandular tissue stated above. To examine its impact on  $\mu_a$  reconstruction, error within 30% was introduced into  $\mu'_{s(heter)}(BKG)$  in the reconstruction mesh. The value of  $\mu'_{s(heter)}(BKG)$  varied between  $0.42 \text{ mm}^{-1}$  and  $0.78 \text{ mm}^{-1}$ , where  $0.6 \text{ mm}^{-1}$  was the true value. The data for reconstruction in every setting was the forward calculated datasets with accurate  $\mu'_{s(heter)}(BKG)$ . The error in the reconstructed  $\mu_a$  values and the phase difference were shown in Figure 4.14.

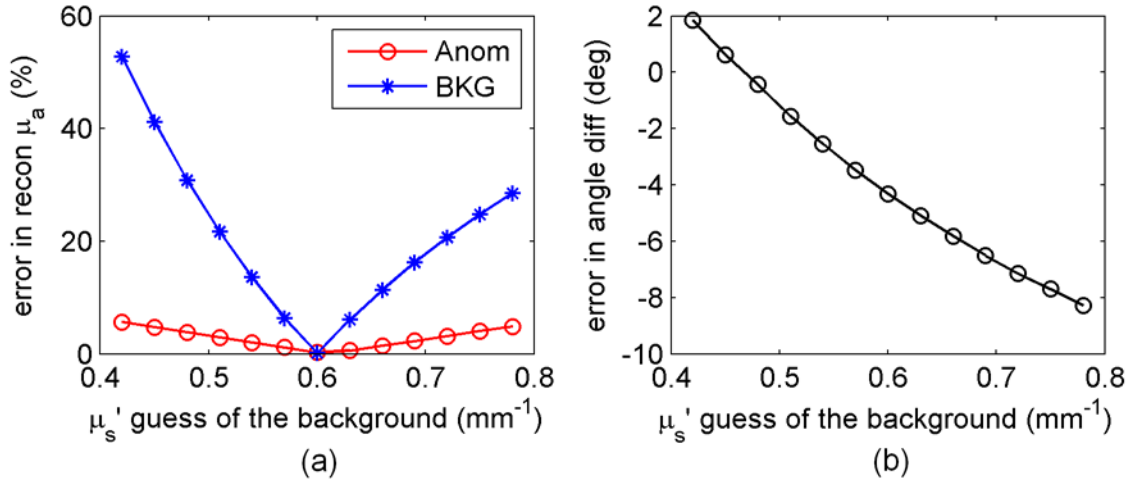


Figure 4.14. (a) The error in the reconstructed  $\mu_a$  caused by wrongly assumed  $\mu'_s$  in the background region is shown. (b) The error in the reconstructed phase relation between the two regions caused by wrongly assumed  $\mu'_s$  in the background region is shown. The true  $\mu'_s$  of the background region was  $0.6 \text{ mm}^{-1}$ .

As shown in Figure 4.14(a), the wrongly assumed  $\mu'_{s(heter)}(BKG)$  had a direct influence on  $\mu_{a(heter)}(BKG)$ , because they were closely related by the effective

attenuation coefficient. Its impact on  $\mu_{a(heter)}(anom)$  was much smaller. Overestimating  $\mu'_{s(heter)}(BKG)$  created smaller error than underestimating it, but the effect was not as strong as in the anomaly case. The impact of  $\mu'_{s(heter)}(BKG)$  on phase analysis was shown in Figure 4.14(b), where a monotonous decreasing curve was displayed. Generally the error of phase difference was within  $6^\circ$  even when 30% error was introduced into  $\mu'_{s(heter)}(BKG)$ .

#### 4.2.6 Conclusion for error analysis

Various possible errors which may exist in clinical experiments with the multi-modal imaging system have been examined through a series of phantom simulations in sections 4.2.1 to 4.2.5. Reducing coupling error and accurate positioning of the anomaly region are beneficial for both  $\mu_a$  recovery and phase analysis. Overestimating the size of the anomaly region a little is a safe option to improve its  $\mu_a$  recovery. Errors in pre-assigned  $\mu'_s$  values of the heterogeneous phantom directly affect the reconstruction value of  $\mu_a$ , but have minor impact on phase analysis. Error of  $\mu'_s$  assumption of the homogeneous phantom has little impact on  $\mu_a$  recovery and phase analysis. The combining effect of all kinds of errors was not examined here, because the possible interaction between errors was too complicated to model. The meshes used in the simulation were slab-shaped phantom with a circular anomaly, which also differ from the structure of human breast. But these will not change the general trend and the conclusion.

It was also found that the reconstructed  $\mu_a$  values of the heterogeneous phantom were much more sensitive to the errors than the phase relation of  $\mu_a$  between different regions. The error in phase difference was below  $10^\circ$  in most simulation settings, not to

mention those error settings were definitely exaggerated comparing with a careful designed clinical experiments. Therefore the phase analysis with the NIR system should be robust, and they can be used in clinical experiments to reveal the response delay between different tissue types.

### **4.3 Imaging experiment of the first human subject**

After the first human subject had laid prone on the breast coil on the MR bed, her right breast was compressed into a slab shape of 54 mm thick by the breast interface. The scout scans, T1-weighted and T2-weighted scans in the coronal view took the MR system 15 minutes in total to complete. The NIR system was synchronized with the vital sign monitor (would be called PO from now on because only its pulse oximetry function was used), and both devices took measurement at 10 Hz for 275 seconds in this exam.

A coronal T1 MR image of the breast was shown in Figure 4.15(a). The dark region inside the tissue was mostly fibro-glandular tissue with higher hemoglobin content, while the gray regions were mostly adipose or fatty tissues which generally have lower hemoglobin content [85]. Based on the MR image, a 2-dimensional mesh with 8000 nodes was created and segmented into two regions as shown in Figure 4.15(b) to perform region-based reconstruction.

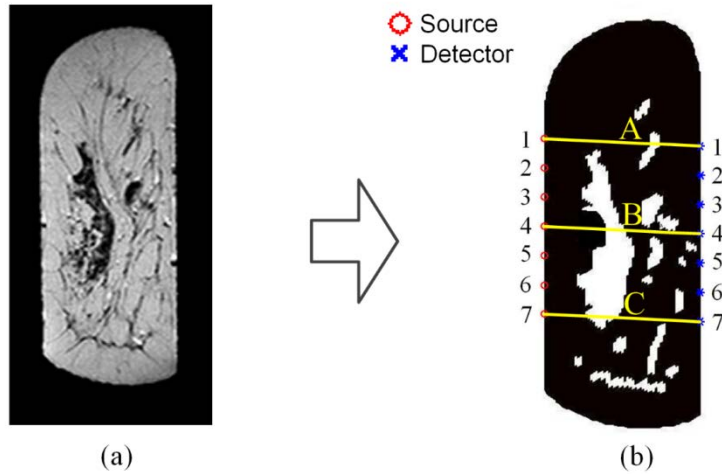


Figure 4.15. (a) A breast MR image (coronal view) of the first healthy human subject is shown. (b) A finite element mesh generated from (a) was segmented into the fibroglandular region (white) and the adipose region (black) for region-based reconstruction.

A 20-second data stream of the PO analog output was shown in Figure 4.16(a). The Fourier transform of the whole signal sequence was shown in Figure 4.16(b), which showed that the heartbeat rate of the human subject was between 1.1 and 1.4 Hz during the imaging experiment. In order to verify that the NIR system can detect the small fluctuation of the optical signal caused by the heartbeat related pulsatile blood flow of the human subject, three typical source-detector pairs as shown in Figure 4.15(b) were chosen, and their raw data at 785 wavelength band and Fourier transformed spectra were shown in Figure 4.16(c) to (h). In addition to the very low frequency components, there was a strong peak at around 0.25 Hz in every signal, which was attributed to the breathing of the subject. There was also smaller peak in the frequency spectrum of every signal which shared the same 1.1 to 1.4 Hz frequency band as the PO analog output. This was a solid proof that the fluctuation of the optical signals at 785 nm wavelength band

caused by blood flow in the breast tissue could be detected by this NIR system. Identical data analysis was performed on the 830 nm wavelength band, and from which the same conclusion was drawn, as shown in Figure 4.17.

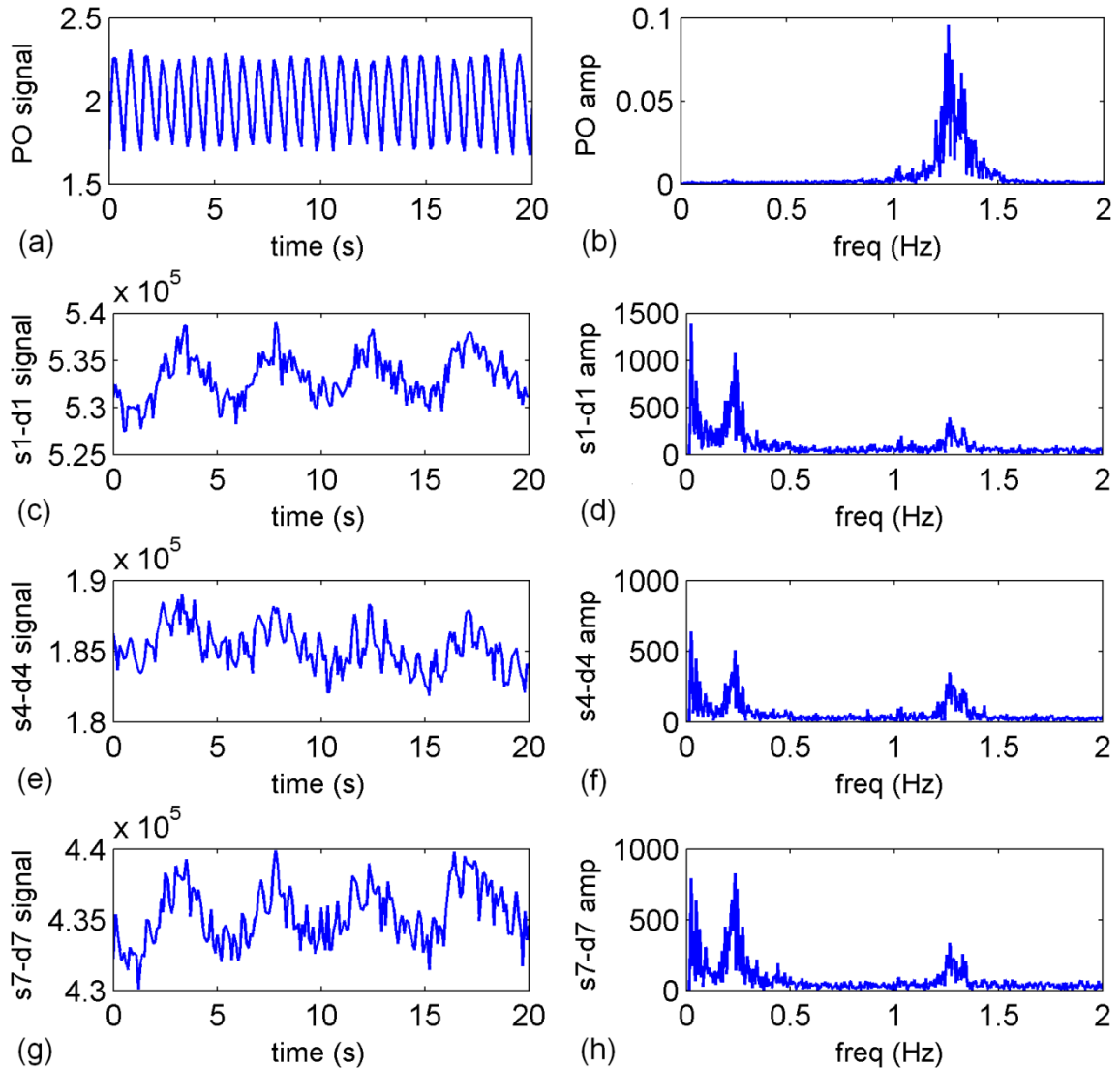


Figure 4.16. (a) A 20-second data stream of the PO analog output in volt. (b) The FFT of the PO output. 20-second data stream of the detected signals from the 785 nm wavelength band of the NIR system for source 1 to detector 1, source 4 to

detector 4, source 7 to detector 7 are plotted in (c), (e) and (g) respectively. Their FFT spectra are shown in (d), (f) and (h) respectively.

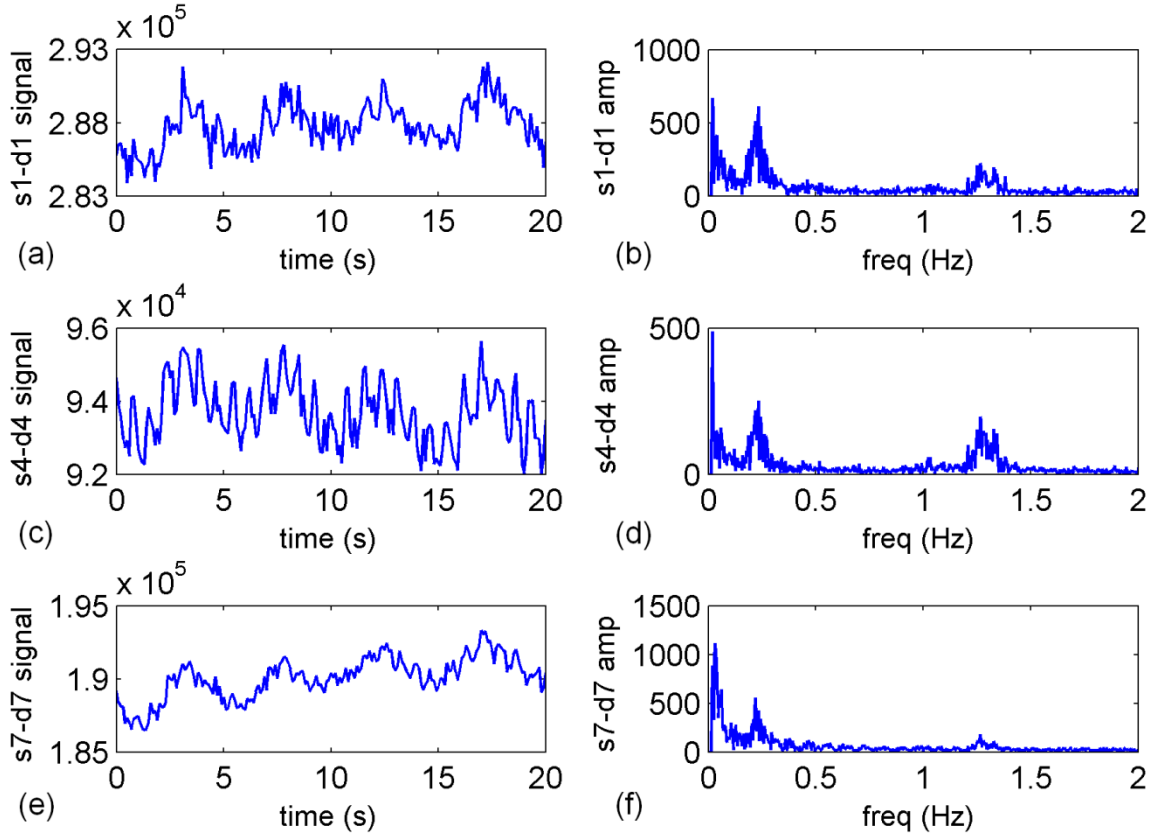


Figure 4.17. 20-second data stream of the detected signals from the 830 nm wavelength band of the NIR system for source 1 to detector 1, source 4 to detector 4, source 7 to detector 7 are plotted in (a), (c) and (e). Their FFT spectra are shown in (b), (d) and (f) respectively.

Because the hemodynamics in the breast is more closely related to the heartbeat, the frequency components related to breathing were filtered out from the raw data first. Then the data were compensated with the intensity profile of sources and the efficiencies of detectors, and calibrated per wavelength band with the measurement on a slab-shaped homogeneous agarose phantom to remove coupling offset. Now the data was ready for

reconstruction. But since the laser sources of the NIR system work in continuous wave mode, the system has no ability to separate absorption coefficient  $\mu_a$  from scattering coefficient  $\mu_s'$  in the images. However extensive earlier work with a frequency domain system has led to reasonable estimation for the  $\mu_s'$  values for adipose and fibroglandular tissues, which appear to be stable to within 15% between subjects [7]. These values are  $\mu_s'(adip) = 0.60 \text{ mm}^{-1}$  in the adipose region and  $\mu_s'(fibro) = 1.00 \text{ mm}^{-1}$  in the fibroglandular region at 785 nm, and  $\mu_s'(adip) = 0.55 \text{ mm}^{-1}$  and  $\mu_s'(fibro) = 0.95 \text{ mm}^{-1}$  at 830 nm.

Assuming the above values for scattering coefficients,  $\mu_a$  of each wavelength band was reconstructed separately and frame by frame using the region-based reconstruction method on a desktop computer. As discussed before, this reconstruction algorithm offered a robust way of exploring the variation of absorption properties. In addition, assuming a uniform distribution of absorption coefficients in each region offers a convenient way to compare the phase relation of the different regions in the breast tissue. The reconstruction generated a time-line of homogeneous absorption property in each region at each wavelength. But only the variation of  $\mu_a$  was shown here, since the accuracy of the absolute value of  $\mu_a$  depended on a lot of factors as stated in section 4.2, especially the pre-assigned values of  $\mu_s'$ . 15 seconds of  $\mu_a$  variation at two wavelengths were shown in Figure 4.18, where the  $\Delta\mu_a$  curves showed a clear period for both tissue types at both wavelengths. The variation of  $\mu_a$  was larger in the fibroglandular region than that in the adipose region, which agreed with common physiological knowledge and previous studies [61]. The variation of  $\mu_a$  at the 830 nm band was slightly larger than that of the 785 nm band in both tissue types, which agreed with the expectation that HbO makes up

the majority fraction of blood in the pulsatile signal, and has a higher absorption coefficient at 830 nm than at 785 nm.

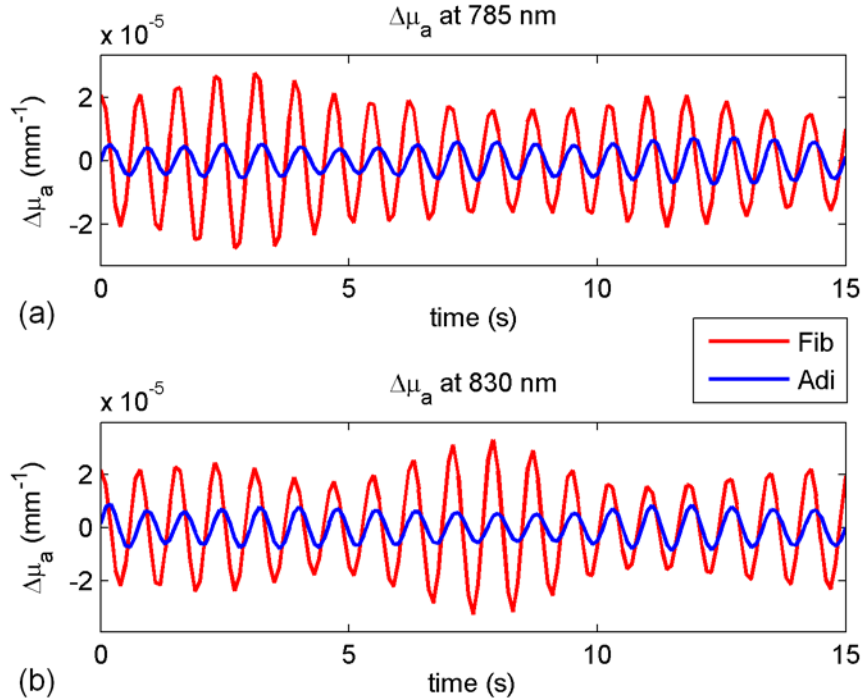


Figure 4.18. The recovered  $\mu_a$  variations in the breast tissue of the first human subject are shown at 785 nm (a) and 830 nm (b), where the red curves are of the fibroglandular region, and the blue curves are of the adipose region.

To verify the temporal resolution of  $\Delta\mu_a$  recovered by the NIR system, the temporal frequencies of recovered  $\Delta\mu_a$  of both tissue types at two wavelengths were computed and compared to the analog output of the PO. For each dataset, FFT was performed on every 10 seconds of the dataset, and the frequency component with the maximal amplitude was recorded as the main frequency of this segment. This process was repeated with the increment of 1 second step size. The curves of peak frequencies of the fibroglandular region at both wavelengths along the time were plotted in Figure 4.19, together with that of the analog output of the PO. The curves of the adipose region were

omitted just for clarity since they almost overlapped with the curves of the fibroglandular region, which also verified that those two tissue types were driven by the same pulse. The general shapes of the curves in Figure 4.19 were identical, which proved the NIR system could capture the temporal change of  $\mu_a$  as the PO did. Despite the identical shapes, the curve of PO had about 4 seconds lag compared to the other two. This was probably due to the smoothing and data processing algorithms inside the PO.

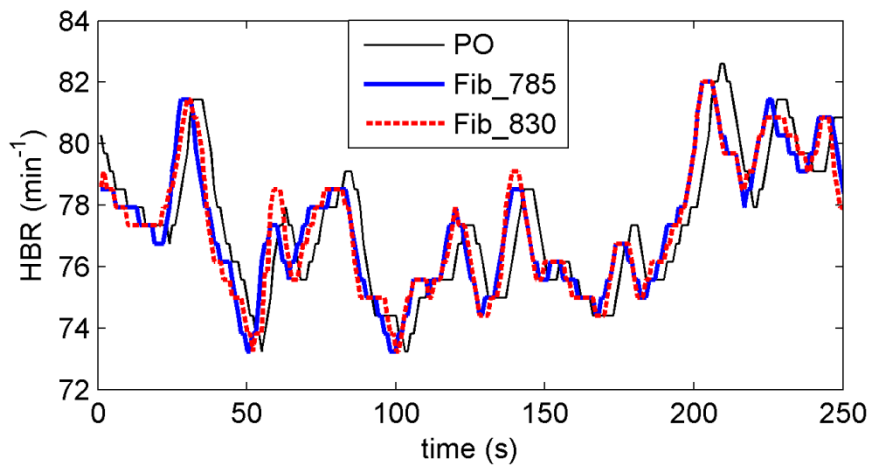


Figure 4.19. The peak frequency of the analog output of the PO along the time is shown, together with the peak frequencies of the reconstructed  $\Delta\mu_a$  of the fibroglandular region at both wavelength bands.

In addition to the temporal frequency, the phase relation between different tissue types could also be analyzed using the reconstructed  $\Delta\mu_a$  curves of high time resolution. The algorithm for phase relation analysis has been explained in detail in section 4.2. Basically, the strongest frequency components of two  $\Delta\mu_a$  curves at the same time span were found and their phase relation was calculated. The time span was chosen to be 10 seconds which was a tradeoff between time resolution and frequency resolution, and the process was repeated with 1 second step size. This algorithm was applied on the  $\Delta\mu_a$

curves of two tissue types and two wavelengths. They all used the analog output of the PO as the reference, because the latter had been pre-processed inside the PO and the noise was mostly removed. The phase analysis results were shown in Figure 4.20 below.

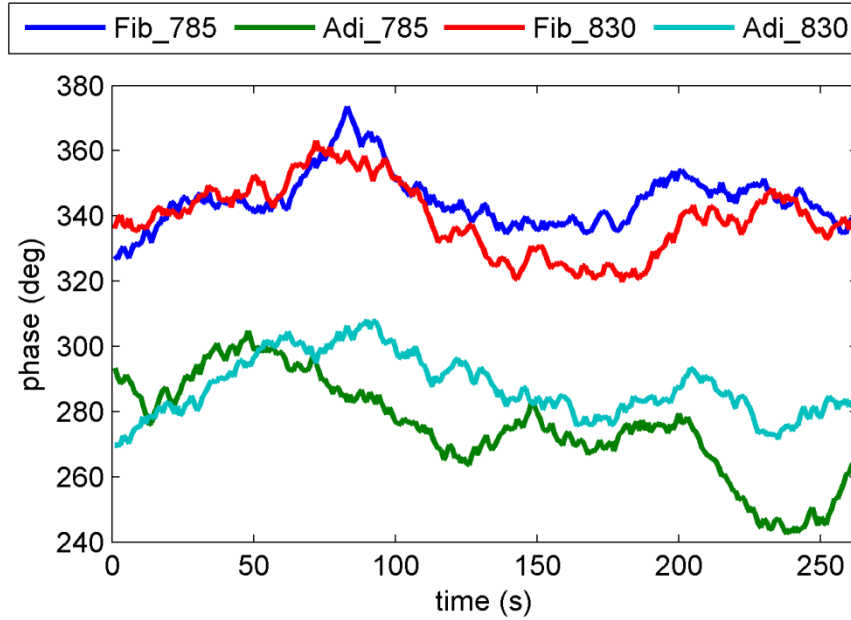


Figure 4.20. The phase relation of  $\Delta\mu_a$  of two breast tissue types of the first human subject at two wavelength bands is shown, with the PO analog output as the reference. All phases were unwrapped and shifted to be between  $0^\circ$  and  $360^\circ$ , showing the extent the corresponding signal ahead of the PO analog output.

The positive phase values in Figure 4.20 indicated that the variation of the corresponding  $\Delta\mu_a$  was ahead of the PO analog output. But it has to be noted that this phase relation is based on comparing signal components of the same frequency, so A ahead of B by  $\theta^\circ$  can also be translated as B ahead of A by  $(360 - \theta)^\circ$ . Therefore the actual sequence of those signals could not be obtained, and thus instead we focused more on the relative phase relations of  $\Delta\mu_a$  curves in this phase plot.  $\Delta\mu_a$  curves in the same

tissue region at both wavelength bands should be exactly in phase, because the pulsatile blood flow was the same to every wavelength in the same region. As shown in Figure 4.20, the  $\Delta\mu_a$  curves in the fibroglandular region at both wavelength bands were almost in phase, and so did the  $\Delta\mu_a$  curves in the adipose region. The small discrepancy of  $\Delta\mu_a$  curves of the same region at two wavelengths was caused by the noise in the experiment. There was a reasonably stable phase difference of about  $60^\circ$  between the  $\Delta\mu_a$  curves of the two regions, so the conclusion was that the  $\Delta\mu_a$  curves in the fibroglandular region were ahead of those in the adipose region by one sixth period of heartbeat, or in another word, the  $\Delta\mu_a$  curves in the fibroglandular region were behind of those in the adipose region by five sixth period of heartbeat. Since the main frequency of the curves was around 1.3 Hz, this phase difference could also be translated as: the response of the fibroglandular region was 0.13 second ahead of that of the adipose region, or equally the absorption response of the fibroglandular region was 0.65 second behind that of the adipose region, depending on which direction to choose. The physiological indication of this result is that the vascular responses to the heartbeat of the fibroglandular tissue and the adipose tissue are not exactly simultaneous, and there is a blood diffusion delay between the two tissue types.

#### **4.4 Imaging experiment of the second human subject**

The setup of the second human subject imaging experiment was similar to that of the first one described before. After the subject had laid prone on the breast coil on the MR bed, her right breast was compressed into a slab shape of 52 mm thick by the breast interface. The scout scans, T1-weighted and T2-weighted scans in the coronal view took

the MR system 15 minutes in total to complete. The NIR system was synchronized with the PO, and both devices took measurement at 20 Hz for 134 seconds in this exam.

A coronal view T1 MR image of the breast was shown in Figure 4.21(a). The dark region inside the tissue was mostly fibroglandular tissue, and the gray regions were mostly adipose tissues. Based on the MR image, a 2-dimensional mesh with 3963 nodes was created and segmented into two regions as shown in Figure 4.21(b) to perform region-based reconstruction.

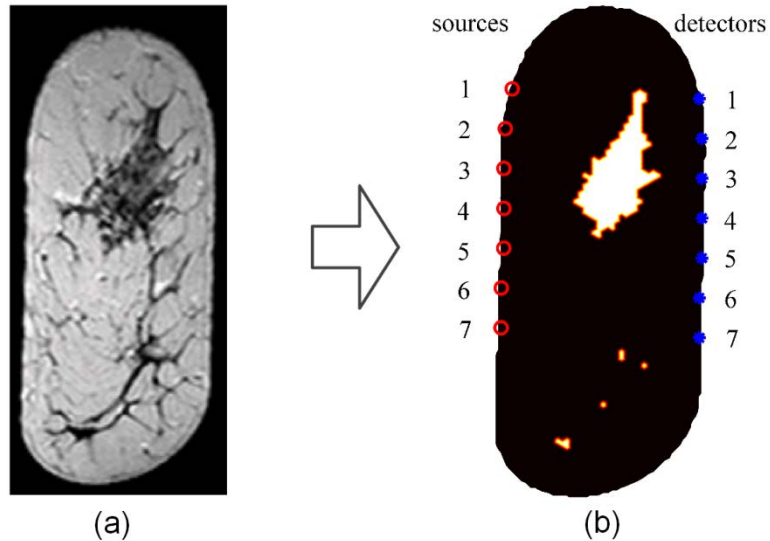


Figure 4.21. (a) A breast MR image (coronal view) of the second healthy human subject is shown. (b) A finite element mesh generated from (a) was segmented into the fibroglandular region (white) and the adipose region (black) for region-based reconstruction.

A 15-second data stream of the PO analog output was shown in Figure 4.22(a). The Fourier transform of the whole signal sequence was shown in Figure 4.22(b), which showed that the heartbeat rate of the human subject was around 1.2 Hz in the imaging experiment. The optical signals from source 4 to detector 4 at two wavelengths, and their

spectra after Fourier transform, were also displayed in Figure 4.22(c) to (f). The strong peaks around 0.2 Hz at both wavelengths were attributed to the breathing of the human subject. Similar to the PO analog output, there were smaller peaks around 1.2 Hz in the frequency spectrum of every signal as well, which proved that the fluctuation of the optical signals at both wavelength bands caused by blood flow in the breast tissue can be detected by this NIR system.

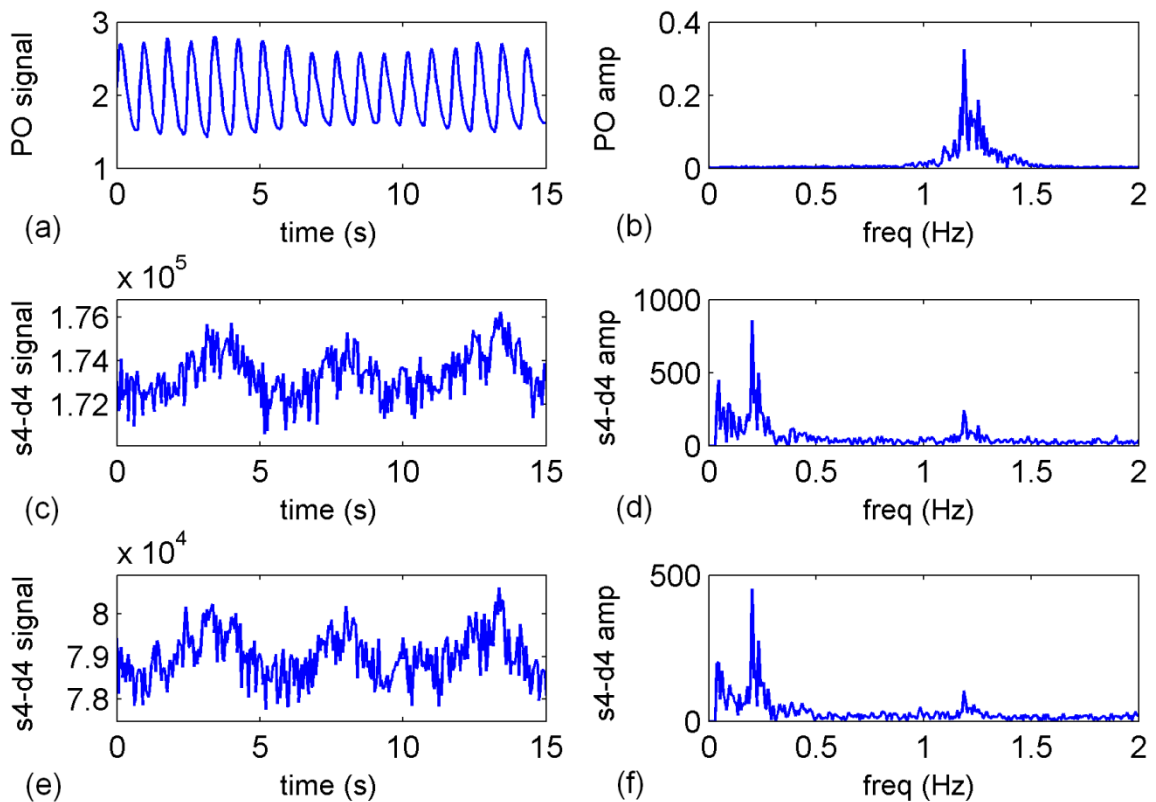


Figure 4.22. (a) A 15-second data stream of the PO analog output in volt. (b) The FFT of the PO output in (a). (c) 15-second data stream of the detected signal from source 4 to detector 4 at the 785 nm wavelength band. (d) The FFT of the signal in (c). (e) 15-second data stream of the detected signal from source 4 to detector 4 at the 830 nm wavelength band. (f) The FFT of the signal in (e).

The data preprocess, calibration, and pre-assigned scattering properties of two tissue types at two wavelengths were the same as those of the first human subject experiment in section 4.3.  $\mu_a$  of each wavelength band was reconstructed separately and frame by frame using the region-based reconstruction method on a desktop computer.

15-second data streams of the reconstructed  $\mu_a$  variation in both regions at two wavelength bands were shown in Figure 4.23, where all four  $\Delta\mu_a$  curves showed a clear periodical trend. Similar to the results in the first human subject experiment, the variation of  $\mu_a$  was larger in the fibroglandular region than that in the adipose region, and the variation of  $\mu_a$  at the 830 nm band was slightly larger than that of the 785 nm band in both tissue types. Additionally, the variation of  $\mu_a$  in Figure 4.23 was smaller than that of Figure 4.18, which was coincident with the observation that the fluctuation of the optical signals in the first human subject experiment (Figure 4.16 and Figure 4.17) was larger than those in this experiment (Figure 4.22).

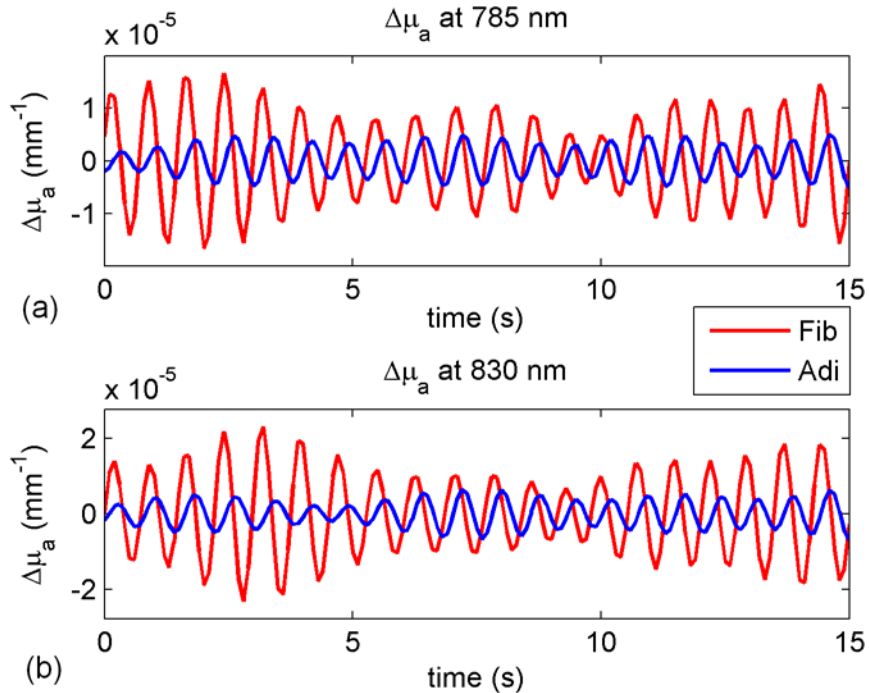


Figure 4.23. The recovered  $\mu_a$  variation in the breast tissue of the second human subject are shown at 785 nm (a) and 830 nm (b), where the red curves are of the fibroglandular region, and the blue curves are of the adipose region.

The temporal frequencies of recovered  $\Delta\mu_a$  of both tissue types at two wavelengths were calculated and compared to the analog output of the PO, using the same method as in section 4.3. FFT was performed on every 10 seconds of the dataset with the increment of 1 second step size. The peak frequency curves of the adipose region at both wavelengths along the time were plotted in Figure 4.24, together with that of the analog output of the PO. The curves of the fibroglandular region were omitted for clarity. The general shapes of the three curves in Figure 4.24 were identical, which again proved the NIR system could capture the temporal change of  $\mu_a$  as the PO did. Despite the identical shapes, the curve of PO has about 5 seconds lag compared to the other two as noticed before in Figure 4.19 of section 4.3.

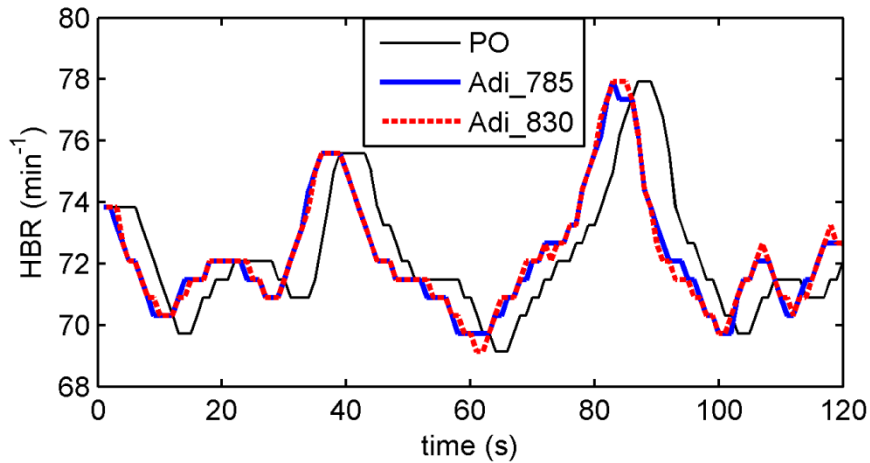


Figure 4.24. The peak frequency of the analog output of the PO along the time is shown, together with the peak frequencies of the reconstructed  $\Delta\mu_a$  of the adipose region at both wavelength bands.

In addition to the temporal frequency, the phase relation between  $\Delta\mu_a$  curves of different tissue types and wavelengths was also analyzed using the identical procedure in section 4.3, where the analog output of the PO was used as the reference. 10 seconds was chosen as the length of the time segment, and the step size was 1 second. The results were shown in Figure 4.25.

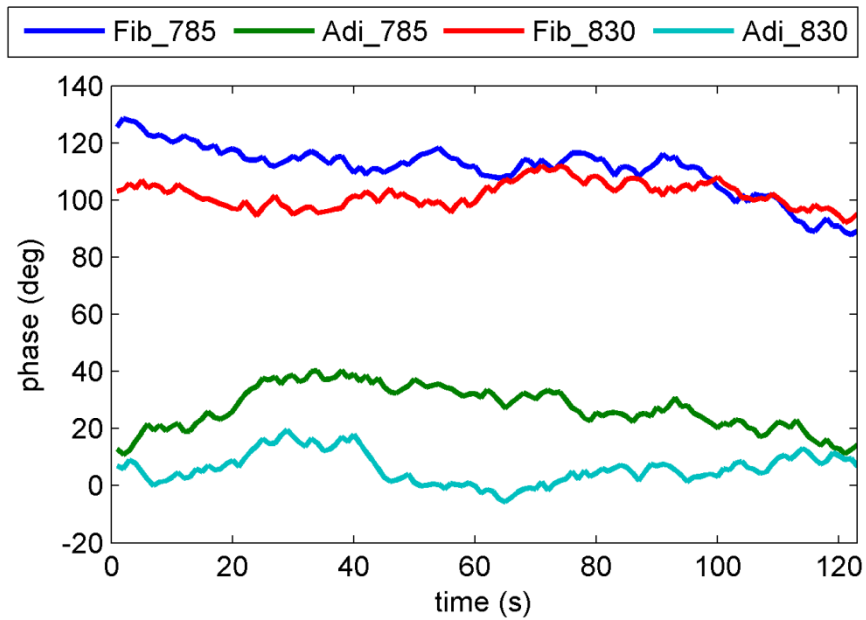


Figure 4.25. The phase relation of  $\Delta\mu_a$  of two breast tissue types of the second human subject at two wavelength bands is shown, with the PO analog output as the reference. All phases were unwrapped and shifted to be between  $0^{\circ}$  and  $360^{\circ}$ , showing the extent the corresponding signal ahead of the PO analog output.

Similar to Figure 4.20, the phase curves in Figure 4.25 could be easily divided into two groups, one containing two curves of the fibroglandular region, and one containing two curves of the adipose region. Noise induced phase discrepancy could be seen in either group, but there was an apparent phase difference of about  $100^{\circ}$  between the  $\Delta\mu_a$

curves of the two regions, indicating physiologically that the vascular responses to the heartbeat of the fibroglandular tissue and the adipose tissue were not exactly simultaneous, as seen before in section 4.3. Since the main frequency of the  $\Delta\mu_a$  curves was around 1.2 Hz, this phase difference could also be translated as: the absorption response of the fibroglandular region was 0.23 second ahead of that of the adipose region, or equally the absorption response of the fibroglandular region was 0.60 second behind that of the adipose region, depending on the chosen direction. It was noted that the value of the phase difference in this experiment was not the same as the one in the previous experiment, but this difference was physiologically possible, and different noise levels in these two experiments may contribute as well.

## **4.5 Conclusion**

In this chapter, the two-wavelength NIR tomography system was successfully integrated into a clinical MR system to realize simultaneous multimodal imaging on human subjects. Most major noise sources emerging with this multimodal design were carefully examined through a series of simulations. It turned out that the recovered value of absorption properties were much more sensitive to the noise than the temporal phase relationship of absorption changes between different tissue regions. The heterogeneous nature of the breast optical properties, and the error in the pre-assigned scattering properties would directly affect the accuracy of the recovered absorption properties, while the errors were static and so would not influence the phase relationship significantly. If accurate estimation is difficult, slight overestimation of the anomaly size and scattering properties were a safer option to yield good reconstruction result. Good coupling between fibers and the medium was essential for accurate recovery as well.

Two healthy human subjects have been imaged within this multimodal system, with their finger pulse oximetry measured at the same pace as the NIR system. By comparing the Fourier spectrum of the raw data as well as the temporal frequency curves with the pulse oximetry measurement, the multimodal system has demonstrated its capacity to pick up and recover the small pulsatile absorption property change in the breast tissue caused by the heartbeat driven blood flow. With an improved phase analysis algorithm, it was discovered that the vascular responses to the heartbeat of the fibroglandular tissue and the adipose tissue were not exactly simultaneous. To our knowledge, this is the first temporal phase comparison of absorption or hemoglobin content between different types of breast tissue. Previous results from NIR brain imaging have repeatedly shown phase shifts between oxyhemoglobin and deoxyhemoglobin [86, 87], but were based on homogeneous estimation of the whole imaging domain.

The value of NIR spectroscopy to breast tumor imaging has been demonstrated in several individual trials[49, 88-90], and is just about to enter multicenter trials to study the prognostic value for neoadjuvant chemotherapy[91]. With the goal of clinical hemodynamic imaging of the breast by tracking absorption changes at high speed, this design potentially adds a different dimension of data of this type of imaging, providing temporal pulsatile feature information of specific regions.

## Chapter 5. Conclusions

### 5.1 Thesis summary

This study demonstrates the technology and methodology to build a NIR tomography system with spectrally-encoded sources in two wavelength bands which is capable of quantifying the temporal oxyhemoglobin and deoxyhemoglobin contrast in breast tissue at a 20 Hz bandwidth. This work involved three distinct developing phases.

First, a single-wavelength high-speed NIR tomography system was built, where eight LD sources with about 10 mW power output were spectrally encoded, and eight spectrometers were hardware synchronized and controlled by a customized LABVIEW program. This design didn't require source switching or shutter operations, so high-speed and continuous data acquisition could be realized. Both static and dynamic imaging experiments were carried out on slab-shaped tissue-like phantoms, where the system demonstrated its capacity to image through phantoms of up to seven centimeters thick at a speed as high as 20 Hz. Results of three reconstruction methods were compared, where the region-based reconstruction method excelled for its superior linearity and accuracy. This discovery was consistent with the hypothesis that the introduction of spatial priors could reduce the tomographic imaging problem to a spectroscopic imaging problem, thus made the ill-posed inverse problem much less susceptible to noise.

Then the NIR system was updated to include a second wavelength band at 830 nm without compromising on imaging speed. In a series of phantom experiments this new two-wavelength NIR system recovered total hemoglobin and temporal oxygen saturation with reasonable accuracy, which were more clinically preferable than solely the

absorbance distribution. Pulse oximetry was also experimented on a phantom with this two-wavelength system, but the proposed algorithms could not generate a stable reading of  $S_pO_2$  as expected. It was concluded that the small separation between wavelength bands and high scatter in the medium contributed to this result, and thus the pulse oximetry algorithm was not applicable on this NIR system.

Finally the two-wavelength NIR system was successfully integrated into a clinical MR system through a customized breast coil, and synchronized to the finger pulse oximeter plethysmogram to realize simultaneous multimodal imaging on human subjects. Prior to clinical experiments, most major noise sources emerging with this multimodal design were carefully examined through simulation. It turned out that the recovered value of absorption properties were much more sensitive to the noise than the temporal phase relationship of absorption changes between different tissue regions. Two healthy subjects have been examined with this multimodal system. By comparing the Fourier spectrum of the raw optical data as well as the temporal frequency of recovered  $\mu_a$  with the pulse oximetry measurement, this multimodal system was proven to be able to pick up and recover the small pulsatile absorption property change in the breast tissue caused by the heartbeat driven blood flow. It was also discovered that the vascular responses to the heartbeat of the fibroglandular tissue and the adipose tissue were not exactly simultaneous in the breast.

In summary, the performance of this two-wavelength system was verified numerically and experimentally. Admittedly, this NIR system requires prior information about  $\mu_s'$ , which is not available with the CW working mode of LDs. But with the tissue structural information from MR, and pre-assigned homogeneous  $\mu_s'$  of each tissue region,

this system can recover the temporal absorbance, and the response delay of different tissue regions inside the breast can be analyzed as well. The high-speed feature of this system makes it well fit for applications such as monitoring the clearance of optical contrast agents, or where the response sequence of different tissue regions is of interest.

## 5.2 Future directions

The incapacity to distinguish absorbance from scatter is the biggest obstacle that stops this system from accurately recovering hemoglobin content and oxygen saturation. We are working on incorporating a frequency-domain NIR tomography system with six discrete measurement wavelengths [52, 58] previously developed in our group which can provide reference  $\mu'_s$  and chromophore information of the breast tissue. The fiber coupler of the high-speed NIR system will be modified to fit into the new breast interface (shown in Figure 5.1) which is designed to accommodate fibers from both the high-speed NIR system and the multi-wavelength NIR system, facilitating the measurement of all major tissue chromophores, scattering, and dynamic changes in HbO and Hb in a single imaging session.

With this hybrid design, the high-speed NIR system can incorporate the prior information of reference  $\mu'_s$  and chromophore from the multi-wavelength NIR system into the reconstruction, and accurately recover temporal hemoglobin content and oxygen saturation in addition to the phase relationship analysis. The high speed and accuracy of this hybrid design make it a perfect option to monitor dynamic contrast mechanisms in breast tissue.

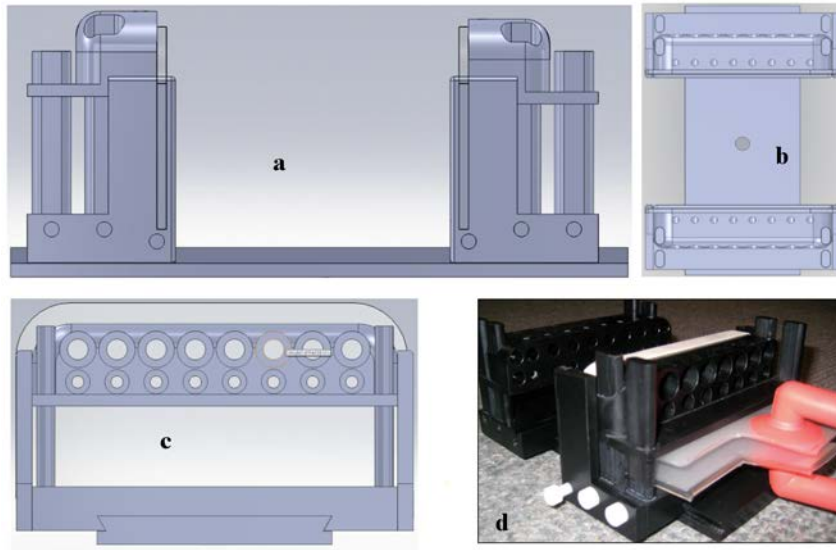


Figure 5.1. (a) The designs of the new breast interface [58] are shown from the profile side view (a), top view (b) and front view (c). (d) shows the fabricated product with lift bag and elastic in place. The upper holes are for the fibers of the multi-wavelength NIR system, and the lower holes are for the high-speed NIR system.

One example is to monitor the rapid vascular changes in breast tissue induced from exogenous incentives, such as gas inhalation changes [92, 93]. Jiang et al used a three-wavelength FD NIR system to measure the dynamic vascular change in breast tissue at 30 seconds time resolution by varying the concentration of O<sub>2</sub> and CO<sub>2</sub> in the inhaled gas, where a large change of 21% in Hb and 9% in SO<sub>2</sub> has been recorded as shown in Figure 5.2. And the hybrid design in this thesis may provide an alternative apparatus with better accuracy and time resolution. The extent of vascular changes could be used to evaluate the tumor hypoxia, and to provide prognostic information about the response of patients to neoadjuvant chemotherapy [1, 94, 95].

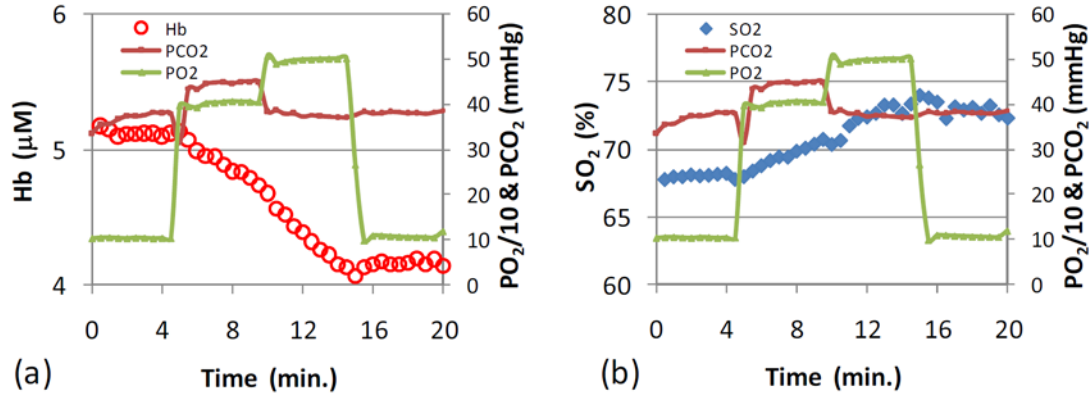


Figure 5.2. Dynamic changes of (a) Hb, (b) of a subject under stimulation of 5 min. of hypercarbia & hyperoxia followed by 5 min hyperoxia imaging [93].

Another example is to monitor the absorption variation caused by pharmacodynamics of optical contrast agent in breast tissue. The tumor site in breast tissue has leaky capillaries of tumor vessels, and thus the pharmacokinetic rates should be higher around the tumor region [96]. This feature can be used to help the detection of breast tumor. Till now, indocyanine green (ICG) is the only NIR organic dye approved by the Food and Drug Administration for use in the human body. And there have been several studies about its diffusion inside human breast [62, 96, 97], but none of them have reached sub-second speed. Figure 5.3(a) showed the schematic breast interface of a single-wavelength CW system developed at University of Pennsylvania which consisted of 16 sources and 16 detectors and could run at 8.8 seconds a frame. Figure 5.3(b) showed the absorption increase in breast tissue after ICG was injected intravenously by bolus with a concentration of  $0.25 \text{ mg kg}^{-1}$  of body weight.

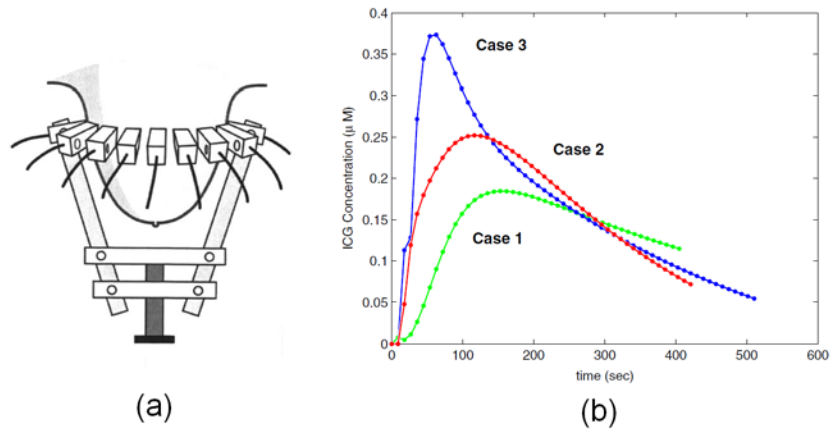


Figure 5.3. (a) Schematic diagram of the breast interface of a CW NIR system developed at UPenn [62]. (b) Time course of ICG concentration curves for a specific voxel in three patients [96].

The linearity response to the concentration of ICG has also been verified on the high-speed two-wavelength NIR system. A batch of solutions mixed with different ICG concentrations and 0.75% intralipid were added into the anomaly inside an agarose phantom in sequence similar to the experiment in section 3.2, and NIR measurements were taken. The  $\mu_a$  values of the anomaly at two wavelengths were reconstructed and displayed in Figure 5.4, where a superior linearity relationship between  $\mu_a$  and ICG concentration can be seen. So the temporal concentration of ICG in the breast could be recovered if the high-speed two-wavelength NIR system is applied in human experiments with ICG administration.

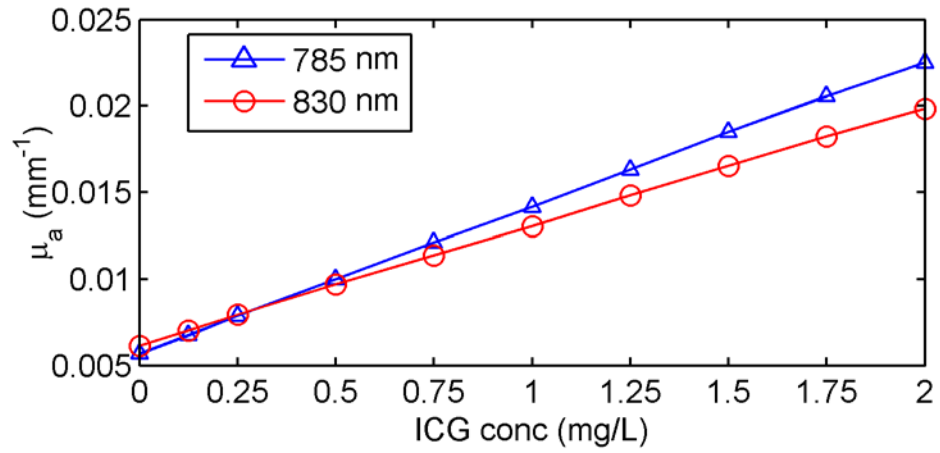


Figure 5.4. The relationship of  $\mu_a$  of ICG and 0.75% intralipid mixture at two wavelengths with regard to the concentration of ICG is shown.

## BIBLIOGRAPHY

- [1] B. J. Tromberg, B. W. Pogue, K. D. Paulsen, A. G. Yodh, D. A. Boas, and A. E. Cerussi, "Assessing the future of diffuse optical imaging technologies for breast cancer management," *Med Phys*, vol. 35, pp. 2443-51, Jun 2008.
- [2] (Apr. 16th). *Breast Cancer*. Available: <://www.cancer.gov/cancertopics/types/>
- [3] *Breast Cancer Facts & Figures 2007-2008*. Available: [.cancer.org/downloads/stt/bcff-final](://cancer.org/downloads/stt/bcff-final).
- [4] USPSTF, "Screening for Breast Cancer: U.S. Preventive Services Task Force Recommendation Statement," *Annals of Internal Medicine*, vol. 151, pp. 716-726, 2009.
- [5] (2002). *Screening for Breast Cancer: Recommendations and Rationale*. Available: <://www.ahrq.gov/clinic/3rduspstf/breastcancer/breanrr>.
- [6] T. Morimoto, T. Nagao, K. Okazaki, M. Kira, Y. Nakagawa, and A. Tangoku, "Current status of breast cancer screening in the world," *Breast Cancer*, vol. 16, pp. 2-9, 2009.
- [7] L. Tabar, M. F. Yen, B. Vitak, H. H. Chen, R. A. Smith, and S. W. Duffy, "Mammography service screening and mortality in breast cancer patients: 20-year follow-up before and after introduction of screening," *Lancet*, vol. 361, pp. 1405-10, Apr 26 2003.
- [8] (2007). *Cancer Trends Progress Report - 2007 Update*. Available: [://progressreport.cancer.gov/doc\\_detail.asp?pid=1&did=2007&chid=72&coid=716&mid=#](://progressreport.cancer.gov/doc_detail.asp?pid=1&did=2007&chid=72&coid=716&mid=#)
- [9] (2009). *Mammography Factsheet*. Available: <://www.cancer.gov/cancertopics/factsheet/Detection/screening->
- [10] A. M. Chiarelli, V. Majpruz, P. Brown, M. Theriault, R. Shumak, and V. Mai, "The contribution of clinical breast examination to the accuracy of breast screening," *J Natl Cancer Inst*, vol. 101, pp. 1236-43, Sep 16 2009.
- [11] (2007). *ACS Advises MRIs for Some at High Risk of Breast Cancer, Get Scans Along With Mammograms, Not Instead of Them*. Available: [://www.cancer.org/docroot/NWS/content/NWS\\_1\\_1X\\_Society\\_Advises\\_MRIs\\_for\\_Some\\_Women\\_at\\_High\\_Risk\\_of\\_Breast\\_Cancer](://www.cancer.org/docroot/NWS/content/NWS_1_1X_Society_Advises_MRIs_for_Some_Women_at_High_Risk_of_Breast_Cancer).
- [12] *For Healthcare Providers - Breast MRI Indications*. Available: <://www.hastingsimagingcenter.com/for-healthcare-providers-indications-breast-mri-nebraska>.

- [13] D. Saslow, C. Boetes, W. Burke, S. Harms, M. O. Leach, C. D. Lehman, E. Morris, E. Pisano, M. Schnall, S. Sener, R. A. Smith, E. Warner, M. Yaffe, K. S. Andrews, and C. A. Russell, "American Cancer Society guidelines for breast screening with MRI as an adjunct to mammography," *CA Cancer J Clin*, vol. 57, pp. 75-89, Mar-Apr 2007.
- [14] Improving Methods for Breast Cancer Detection and Diagnosis. Available: [://www.cancer.gov/cancertopics/factsheet/Detection/breast-](http://www.cancer.gov/cancertopics/factsheet/Detection/breast-)
- [15] A. Sarvazyan, V. Egorov, J. S. Son, and C. S. Kaufman, "Cost-Effective Screening for Breast Cancer Worldwide: Current State and Future Directions," *Breast Cancer*, vol. 1, pp. 91-99, Jul 2 2008.
- [16] M. Cutler, "Transillumination as an aid in the diagnosis of breast lesions," *Surg. Gynecol. Obstet*, vol. 48, 1929.
- [17] O. Jarlman, G. Balldin, I. Andersson, M. Lofgren, A. S. Larsson, and F. Linell, "Relation between lightscanning and the histologic and mammographic appearance of malignant breast tumors," *Acta Radiol*, vol. 33, pp. 63-8, Jan 1992.
- [18] J. F. Nunn, *Applied Respiratory Physiology*. Boston, MA: Butterworth-Heinemann, 1987.
- [19] J. G. Webster, *Design of Pulse Oximeters*: Taylor & Francis, 1997.
- [20] (2002). *History of Pulse Oximetry*. Available: [://www.oximeter.org/pulseox/history](http://www.oximeter.org/pulseox/history).
- [21] J. W. Severinghaus and Y. Honda, "History of blood gas analysis. VII. Pulse oximetry," *J Clin Monit*, vol. 3, pp. 135-8, Apr 1987.
- [22] Masimo. *Signal Extraction Technology*. Available: [.masimo.com/pdf/technology/lab1959](http://masimo.com/pdf/technology/lab1959).
- [23] P. Vaupel, S. Briest, and M. Hockel, "Hypoxia in breast cancer: pathogenesis, characterization and biological/therapeutic implications," *Wien Med Wochenschr*, vol. 152, pp. 334-42, 2002.
- [24] S. B. Fox, D. G. Generali, and A. L. Harris, "Breast tumour angiogenesis," *Breast Cancer Res*, vol. 9, p. 216, 2007.
- [25] B. W. Pogue, S. Jiang, H. Dehghani, C. Kogel, S. Soho, S. Srinivasan, X. Song, T. D. Tosteson, S. P. Poplack, and K. D. Paulsen, "Characterization of hemoglobin, water, and NIR scattering in breast tissue: analysis of intersubject variability and menstrual cycle changes," *J Biomed Opt*, vol. 9, pp. 541-52, May-Jun 2004.

- [26] A. Cerussi, S. Siavoshi, A. Durkin, C. Chen, W. Tanamai, D. Hsiang, and B. J. Tromberg, "Effect of contact force on breast tissue optical property measurements using a broadband diffuse optical spectroscopy handheld probe," *Appl Opt*, vol. 48, pp. 4270-7, Jul 20 2009.
- [27] A. Cerussi, N. Shah, D. Hsiang, A. Durkin, J. Butler, and B. J. Tromberg, "In vivo absorption, scattering, and physiologic properties of 58 malignant breast tumors determined by broadband diffuse optical spectroscopy," *J Biomed Opt*, vol. 11, p. 044005, Jul-Aug 2006.
- [28] F. Bevilacqua, A. J. Berger, A. E. Cerussi, D. Jakubowski, and B. J. Tromberg, "Broadband absorption spectroscopy in turbid media by combined frequency-domain and steady-state methods," *Appl Opt*, vol. 39, pp. 6498-507, Dec 1 2000.
- [29] B. J. Tromberg, N. Shah, R. Lanning, A. Cerussi, J. Espinoza, T. Pham, L. Svaasand, and J. Butler, "Non-invasive in vivo characterization of breast tumors using photon migration spectroscopy," *Neoplasia*, vol. 2, pp. 26-40, Jan-Apr 2000.
- [30] S. J. Madsen, E. R. Anderson, R. C. Haskell, and B. J. Tromberg, "Portable, high-bandwidth frequency-domain photon migration instrument for tissue spectroscopy," *Opt Lett*, vol. 19, pp. 1934-6, Dec 1 1994.
- [31] J. B. Fishkin, O. Coquoz, E. R. Anderson, M. Brenner, and B. J. Tromberg, "Frequency-domain photon migration measurements of normal and malignant tissue optical properties in a human subject," *Appl Opt*, vol. 36, pp. 10-20, Jan 1 1997.
- [32] N. Shah, A. E. Cerussi, D. Jakubowski, D. Hsiang, J. Butler, and B. J. Tromberg, "The role of diffuse optical spectroscopy in the clinical management of breast cancer," *Dis Markers*, vol. 19, pp. 95-105, 2003.
- [33] N. Shah, A. Cerussi, C. Eker, J. Espinoza, J. Butler, J. Fishkin, R. Hornung, and B. Tromberg, "Noninvasive functional optical spectroscopy of human breast tissue," *Proc Natl Acad Sci U S A*, vol. 98, pp. 4420-5, Apr 10 2001.
- [34] B. W. Pogue, M. S. Patterson, H. Jiang, and K. D. Paulsen, "Initial assessment of a simple system for frequency domain diffuse optical tomography," *Phys Med Biol*, vol. 40, pp. 1709-29, Oct 1995.
- [35] H. Jiang, K. D. Paulsen, U. L. Osterberg, B. W. Pogue, and M. S. Patterson, "Simultaneous reconstruction of optical absorption and scattering maps in turbid media from near-infrared frequency-domain data," *Opt Lett*, vol. 20, pp. 2128-30, Oct 15 1995.

- [36] H. Jiang, K. Paulsen, U. Osterberg, and M. Patterson, "Improved continuous light diffusion imaging in single-and multi-target tissue-like phantoms," *Physics in Medicine and Biology*, vol. 43, pp. 675-694, 1998.
- [37] T. O. McBride, B. W. Pogue, E. D. Gerety, S. B. Poplack, U. L. Osterberg, and K. D. Paulsen, "Spectroscopic diffuse optical tomography for the quantitative assessment of hemoglobin concentration and oxygen saturation in breast tissue," *Appl Opt*, vol. 38, pp. 5480-90, Sep 1 1999.
- [38] T. McBride, B. Pogue, S. Jiang, U. Österberg, and K. Paulsen, "A parallel-detection frequency-domain near-infrared tomography system for hemoglobin imaging of the breast in vivo," *Review of Scientific Instruments*, vol. 72, p. 1817, 2001.
- [39] T. O. McBride, B. W. Pogue, S. Jiang, U. L. Osterberg, K. D. Paulsen, and S. P. Poplack, "Initial studies of in vivo absorbing and scattering heterogeneity in near-infrared tomographic breast imaging," *Opt Lett*, vol. 26, pp. 822-4, Jun 1 2001.
- [40] B. W. Pogue, S. P. Poplack, T. O. McBride, W. A. Wells, K. S. Osterman, U. L. Osterberg, and K. D. Paulsen, "Quantitative hemoglobin tomography with diffuse near-infrared spectroscopy: pilot results in the breast," *Radiology*, vol. 218, pp. 261-6, Jan 2001.
- [41] T. O. McBride, B. W. Pogue, S. Poplack, S. Soho, W. A. Wells, S. Jiang, U. L. Osterberg, and K. D. Paulsen, "Multispectral near-infrared tomography: a case study in compensating for water and lipid content in hemoglobin imaging of the breast," *J Biomed Opt*, vol. 7, pp. 72-9, Jan 2002.
- [42] S. Srinivasan, B. W. Pogue, B. Brooksby, S. Jiang, H. Dehghani, C. Kogel, W. A. Wells, S. P. Poplack, and K. D. Paulsen, "Near-infrared characterization of breast tumors in vivo using spectrally-constrained reconstruction," *Technol Cancer Res Treat*, vol. 4, pp. 513-26, Oct 2005.
- [43] S. Srinivasan, B. W. Pogue, S. Jiang, H. Dehghani, C. Kogel, S. Soho, J. J. Gibson, T. D. Tosteson, S. P. Poplack, and K. D. Paulsen, "In vivo hemoglobin and water concentrations, oxygen saturation, and scattering estimates from near-infrared breast tomography using spectral reconstruction," *Acad Radiol*, vol. 13, pp. 195-202, Feb 2006.
- [44] S. Jiang, B. Pogue, and K. Paulsen, "Dynamic frequency domain tomography system and phantom test," 2007, p. 64310G.
- [45] J. Wang, B. W. Pogue, S. Jiang, and K. D. Paulsen, "Near-Infrared Tomography of breast cancer hemoglobin, water, lipid and scattering properties using combined frequency domain and continuous wave measurement," *Optical Letter*, Manuscript Preparing.

- [46] A. Corlu, T. Durduran, R. Choe, M. Schweiger, E. M. Hillman, S. R. Arridge, and A. G. Yodh, "Uniqueness and wavelength optimization in continuous-wave multispectral diffuse optical tomography," *Opt Lett*, vol. 28, pp. 2339-41, Dec 1 2003.
- [47] A. Corlu, R. Choe, T. Durduran, K. Lee, M. Schweiger, S. R. Arridge, E. M. Hillman, and A. G. Yodh, "Diffuse optical tomography with spectral constraints and wavelength optimization," *Appl Opt*, vol. 44, pp. 2082-93, Apr 10 2005.
- [48] R. Choe, S. D. Konecky, A. Corlu, K. Lee, T. Durduran, D. R. Busch, S. Pathak, B. J. Czerniecki, J. Tchou, D. L. Fraker, A. Demichele, B. Chance, S. R. Arridge, M. Schweiger, J. P. Culver, M. D. Schnall, M. E. Putt, M. A. Rosen, and A. G. Yodh, "Differentiation of benign and malignant breast tumors by in-vivo three-dimensional parallel-plate diffuse optical tomography," *J Biomed Opt*, vol. 14, p. 024020, Mar-Apr 2009.
- [49] R. Choe, A. Corlu, K. Lee, T. Durduran, S. D. Konecky, M. Grosicka-Koptyra, S. R. Arridge, B. J. Czerniecki, D. L. Fraker, A. DeMichele, B. Chance, M. A. Rosen, and A. G. Yodh, "Diffuse optical tomography of breast cancer during neoadjuvant chemotherapy: a case study with comparison to MRI," *Med Phys*, vol. 32, pp. 1128-39, Apr 2005.
- [50] S. Srinivasan, B. W. Pogue, C. Carpenter, S. Jiang, W. A. Wells, S. P. Poplack, P. A. Kaufman, and K. D. Paulsen, "Developments in quantitative oxygen-saturation imaging of breast tissue in vivo using multispectral near-infrared tomography," *Antioxid Redox Signal*, vol. 9, pp. 1143-56, Aug 2007.
- [51] V. Ntziachristos, A. G. Yodh, M. D. Schnall, and B. Chance, "MRI-guided diffuse optical spectroscopy of malignant and benign breast lesions," *Neoplasia*, vol. 4, pp. 347-54, Jul-Aug 2002.
- [52] C. M. Carpenter, B. W. Pogue, S. Jiang, H. Dehghani, X. Wang, K. D. Paulsen, W. A. Wells, J. Forero, C. Kogel, J. B. Weaver, S. P. Poplack, and P. A. Kaufman, "Image-guided optical spectroscopy provides molecular-specific information in vivo: MRI-guided spectroscopy of breast cancer hemoglobin, water, and scatterer size," *Opt Lett*, vol. 32, pp. 933-5, Apr 15 2007.
- [53] N. Shah, J. Gibbs, D. Wolverson, A. Cerussi, N. Hylton, and B. J. Tromberg, "Combined diffuse optical spectroscopy and contrast-enhanced magnetic resonance imaging for monitoring breast cancer neoadjuvant chemotherapy: a case study," *J Biomed Opt*, vol. 10, p. 051503, Sep-Oct 2005.
- [54] Q. Fang, S. A. Carp, J. Selb, G. Boverman, Q. Zhang, D. B. Kopans, R. H. Moore, E. L. Miller, D. H. Brooks, and D. A. Boas, "Combined optical imaging and mammography of the healthy breast: optical contrast derived from breast structure and compression," *IEEE Trans Med Imaging*, vol. 28, pp. 30-42, Jan 2009.

- [55] Q. Zhu, T. Durduran, V. Ntziachristos, M. Holboke, and A. Yodh, "Imager that combines near-infrared diffusive light and ultrasound," *Optics letters*, vol. 24, pp. 1050-1052, 1999.
- [56] M. J. Holboke, B. J. Tromberg, X. Li, N. Shah, J. Fishkin, D. Kidney, J. Butler, B. Chance, and A. G. Yodh, "Three-dimensional diffuse optical mammography with ultrasound localization in a human subject," *J Biomed Opt*, vol. 5, pp. 237-47, Apr 2000.
- [57] Z. Jiang, D. Piao, G. Xu, J. W. Ritchey, G. R. Holyoak, K. E. Bartels, C. F. Bunting, G. Slobodov, and J. S. Krasinski, "Trans-rectal ultrasound-coupled near-infrared optical tomography of the prostate, part II: experimental demonstration," *Opt Express*, vol. 16, pp. 17505-20, Oct 27 2008.
- [58] M. A. Mastanduno, C. M. Carpenter, S. Srinivasan, S. Jiang, B. W. Pogue, and K. D. Paulsen, "Three-Dimensional MR-Guided Optical Spectroscopy of the Breast: Optimizing Probe Placement for Improved Image Quality," in *Optical Society of America*, 2010, p. JMA78.
- [59] Q. Fang, S. A. Carp, J. Selb, G. Boverman, Q. Zhang, D. B. Kopans, R. H. Moore, E. L. Miller, D. H. Brooks, and D. A. Boas, "Combined Optical Imaging and Mammography of the Healthy Breast: Optical Contrast Derived From Breast Structure and Compression," *Medical Imaging, IEEE Transactions on*, vol. 28, pp. 30-42, 2009.
- [60] Q. Zhu, M. Huang, N. Chen, K. Zarfos, B. Jagjivan, M. Kane, P. Hedge, and H. Kurtzman, "Ultrasound-guided optical tomographic imaging of malignant and benign breast lesions: initial clinical results of 19 cases," *Neoplasia (New York, NY)*, vol. 5, p. 379, 2003.
- [61] B. Brooksby, B. Pogue, S. Jiang, H. Dehghani, S. Srinivasan, C. Kogel, T. Tosteson, J. Weaver, S. Poplack, and K. Paulsen, "Imaging breast adipose and fibroglandular tissue molecular signatures by using hybrid MRI-guided near-infrared spectral tomography," *Proceedings of the National Academy of Sciences*, vol. 103, p. 8828, 2006.
- [62] V. Ntziachristos, A. G. Yodh, M. Schnall, and B. Chance, "Concurrent MRI and diffuse optical tomography of breast after indocyanine green enhancement," *Proceedings of the National Academy of Sciences of the United States of America*, vol. 97, pp. 2767-2772, March 14, 2000 2000.
- [63] C. M. Carpenter, R. Rakow-Penner, S. Jiang, B. W. Pogue, G. H. Glover, and K. D. Paulsen, "Monitoring of hemodynamic changes induced in the healthy breast through inspired gas stimuli with MR-guided diffuse optical imaging," *Medical Physics*, vol. 37, pp. 1638-1646, 2010.

- [64] S. Jiang, B. Pogue, W., C. Carpenter, M., P. Kaufman, A., and K. Paulsen, D., "Near-Infrared Spectral Tomography System for Measuring Dynamic Vascular Changes in Breast," 2010, p. BSuB6.
- [65] C. Schmitz, M. Löcker, J. Lasker, A. Hielscher, and R. Barbour, "Instrumentation for fast functional optical tomography," *Review of Scientific Instruments*, vol. 73, p. 429, 2002.
- [66] D. K. Joseph, T. J. Huppert, M. A. Franceschini, and D. A. Boas, "Diffuse optical tomography system to image brain activation with improved spatial resolution and validation with functional magnetic resonance imaging," *Appl. Opt.*, vol. 45, pp. 8142-8151, 2006.
- [67] D. Piao, S. Jiang, S. Srinivasan, H. Dehghani, and B. W. Pogue, "Video-rate near-infrared optical tomography using spectrally encoded parallel light delivery," *Opt Lett*, vol. 30, pp. 2593-5, Oct 1 2005.
- [68] D. Piao, H. Dehghani, S. Jiang, S. Srinivasan, and B. Pogue, "Instrumentation for video-rate near-infrared diffuse optical tomography," *Review of Scientific Instruments*, vol. 76, p. 124301, 2005.
- [69] D. Piao, S. Jiang, S. Srinivasan, P. Yalavarthy, X. Song, and B. Pogue, "Spectral-encoding for parallel source implementation in NIR tomography," 2005, p. 129.
- [70] G. Xu, D. Piao, C. H. Musgrove, C. F. Bunting, and H. Dehghani, "Trans-rectal ultrasound-coupled near-infrared optical tomography of the prostate, part I: simulation," *Opt Express*, vol. 16, pp. 17484-504, Oct 27 2008.
- [71] D. Piao, H. Xie, W. Zhang, J. S. Krasinski, G. Zhang, H. Dehghani, and B. W. Pogue, "Endoscopic, rapid near-infrared optical tomography," *Opt Lett*, vol. 31, pp. 2876-8, Oct 1 2006.
- [72] T. A. Heumier and J. L. Carlsten. Application Note #5: An Overview of Laser Diode Characteristics.  
Available: [://www.ilxlightwave.com/appnotes/AN%205%20REV02%20LD%20Characteristics%20Overview](http://www.ilxlightwave.com/appnotes/AN%205%20REV02%20LD%20Characteristics%20Overview).
- [73] Opnext. (2006, Datasheet of Hitachi HL7851G GaAlAs Laser Diode. Available: [://www.thorlabs.com/Thorcat/2300/2306-M01](http://www.thorlabs.com/Thorcat/2300/2306-M01).
- [74] T. A. Heumier and J. L. Carlsten. Application Note #8: Mode Hopping in Semiconductor Lasers.  
Available: [://www.ilxlightwave.com/appnotes/AN%208%20REV01%20Mode%20Hopping%20in%20Semiconductor%20Lasers](http://www.ilxlightwave.com/appnotes/AN%208%20REV01%20Mode%20Hopping%20in%20Semiconductor%20Lasers).
- [75] S. Davis, B. Pogue, R. Springett, C. Leussler, P. Mazurkewitz, S. Tuttle, S. Gibbs-Strauss, S. Jiang, H. Dehghani, and K. Paulsen, "Magnetic resonance–

- coupled fluorescence tomography scanner for molecular imaging of tissue," *Review of Scientific Instruments*, vol. 79, p. 064302, 2008.
- [76] B. A. Brooksby, "Combining near infrared tomography and magnetic resonance imaging to improve breast tissue chromophore and scattering assessment," ed, 2005.
- [77] S. Jiang, B. Pogue, S. Srinivasan, S. Soho, S. Poplack, T. Tosteson, and K. Paulsen, "Assessment of the menstrual cycle upon total hemoglobin, water concentration, and oxygen saturation in the female breast," 2003, p. 342.
- [78] T. O. McBride, "Spectroscopic Reconstructed Near Infrared Tomographic Imaging for Breast Cancer Diagnosis," 2001.
- [79] H. Van Staveren, C. Moes, J. van Marie, S. Prahl, and M. van Gemert, "Light scattering in Intralipid-10% in the wavelength range of 400–1100 nm," *Applied Optics*, vol. 30, pp. 4507-4514, 1991.
- [80] B. Brooksby, H. Dehghani, B. Pogue, and K. Paulsen, "Near-infrared (NIR) tomography breast image reconstruction with a priori structural information from MRI: algorithm development for reconstructing heterogeneities," *IEEE Journal of selected topics in quantum electronics*, vol. 9, pp. 199-209, 2003.
- [81] J. D. GRUBER. (2010). *A High-Frequency Ultrasound-Guided Fluorescence Tomography System for Protoporphyrin-IX Quantification within Subcutaneous Tumors*. Available: [://www.dartmouth.edu/~nir/downloads/Gruber](http://www.dartmouth.edu/~nir/downloads/Gruber).
- [82] Z. Li, V. Krishnaswamy, S. Jiang, S. C. Davis, S. Srinivasan, K. D. Paulsen, and B. W. Pogue, "Rapid magnetic resonance-guided near-infrared mapping to image pulsatile hemoglobin in the breast," *Opt. Lett.*, vol. 35, pp. 3964-3966, 2010.
- [83] S. Srinivasan. (2005). *Spectroscopy-based Quantification of Chromophores and Scattering in Near Infrared Tomography*.
- [84] J. Wang, "BROADBAND NEAR-INFRARED TOMOGRAPHY FOR BREAST CANCER IMAGING," 2009.
- [85] B. Brooksby, B. W. Pogue, S. Jiang, H. Dehghani, S. Srinivasan, C. Kogel, T. D. Tosteson, J. Weaver, S. P. Poplack, and K. D. Paulsen, "Imaging breast adipose and fibroglandular tissue molecular signatures by using hybrid MRI-guided near-infrared spectral tomography," *Proc Natl Acad Sci U S A*, vol. 103, pp. 8828-33, Jun 6 2006.
- [86] M. Reinhard, E. Wehrle-Wieland, D. Grabiak, M. Roth, B. Guschlbauer, J. Timmer, C. Weiller, and A. Hetzel, "Oscillatory cerebral hemodynamics--the

- macro- vs. microvascular level," *J Neurol Sci*, vol. 250, pp. 103-9, Dec 1 2006.
- [87] H. Obrig, M. Neufang, R. Wenzel, M. Kohl, J. Steinbrink, K. Einhaupl, and A. Villringer, "Spontaneous low frequency oscillations of cerebral hemodynamics and metabolism in human adults," *Neuroimage*, vol. 12, pp. 623-39, Dec 2000.
- [88] S. Jiang, B. W. Pogue, C. M. Carpenter, S. P. Poplack, W. A. Wells, C. A. Kogel, J. A. Forero, L. S. Muffly, G. N. Schwartz, K. D. Paulsen, and P. A. Kaufman, "Evaluation of breast tumor response to neoadjuvant chemotherapy with tomographic diffuse optical spectroscopy: case studies of tumor region-of-interest changes," *Radiology*, vol. 252, pp. 551-60, Aug 2009.
- [89] A. E. Cerussi, V. W. Tanamai, R. S. Mehta, D. Hsiang, J. Butler, and B. J. Tromberg, "Frequent optical imaging during breast cancer neoadjuvant chemotherapy reveals dynamic tumor physiology in an individual patient," *Acad Radiol*, vol. 17, pp. 1031-9, Aug 2010.
- [90] H. Soliman, A. Gunasekara, M. Rycroft, J. Zubovits, R. Dent, J. Spayne, M. J. Yaffe, and G. J. Czarnota, "Functional Imaging Using Diffuse Optical Spectroscopy of Neoadjuvant Chemotherapy Response in Women with Locally Advanced Breast Cancer," *Clin. Cancer Res.*, vol. 16, pp. 2605-2614, 2010.
- [91] B. J. Tromberg and A. E. Cerussi, "Imaging breast cancer chemotherapy response with light. Commentary on Soliman et al., p. 2605," *Clin Cancer Res*, vol. 16, pp. 2486-8, May 1 2010.
- [92] C. M. Carpenter, R. Rakow-Penner, S. Jiang, B. L. Daniel, B. W. Pogue, G. H. Glover, and K. D. Paulsen, "Inspired gas-induced vascular change in tumors with magnetic-resonance-guided near-infrared imaging: human breast pilot study," *Journal of Biomedical Optics*, vol. 15, p. 036026, 2010.
- [93] S. Jiang, B. W. Pogue, M. A. Mastanduno, K. E. Michaelsen, T. E. Frazee, K. D. Paulsen, S. P. Poplack, W. A. Wells, R. M. diFlorio-Alexander, and P. A. Kaufman, "Assessing dynamic vascular changes in breast tissue in response to subject-specific hyperoxic and hypercarbic gas inhalation based upon end-tidal expiration," presented at the SPIE Bios, San Francisco, CA, 2011.
- [94] A. M. Shannon, D. J. Bouchier-Hayes, C. M. Condron, and D. Toomey, "Tumour hypoxia, chemotherapeutic resistance and hypoxia-related therapies," *Cancer Treatment Reviews*, vol. 29, pp. 297-307, 2003.
- [95] B. Tromberg, A. Cerussi, N. Shah, M. Compton, A. Durkin, D. Hsiang, J. Butler, and R. Mehta, "Imaging in breast cancer: Diffuse optics in breast cancer: detecting tumors in pre-menopausal women and monitoring

neoadjuvant chemotherapy," *Breast Cancer Research*, vol. 7, pp. 279 - 285, 2005.

- [96] B. Alacam, B. Yazici, X. Intes, S. Nioka, and B. Chance, "Pharmacokinetic-rate images of indocyanine green for breast tumors using near-infrared optical methods," *Physics in Medicine and Biology*, vol. 53, p. 837, 2008.
- [97] A. Corlu, R. Choe, T. Durduran, M. A. Rosen, M. Schweiger, S. R. Arridge, M. D. Schnall, and A. G. Yodh, "Three-dimensional in vivo fluorescence diffuse optical tomography of breast cancer in humans," *Opt. Express*, vol. 15, pp. 6696-6716, 2007.